

Gold and silver nanoparticles: synthesis, characterization and functional properties

Author:

Kemal, Lydia

Publication Date:

2008

DOI:

<https://doi.org/10.26190/unsworks/17954>

License:

<https://creativecommons.org/licenses/by-nc-nd/3.0/au/>

Link to license to see what you are allowed to do with this resource.

Downloaded from <http://hdl.handle.net/1959.4/43108> in <https://unsworks.unsw.edu.au> on 2024-05-02

**GOLD AND SILVER NANOPARTICLES:
SYNTHESIS, CHARACTERIZATION AND
FUNCTIONAL PROPERTIES**

BY
LYDIA KEMAL

A thesis submitted in fulfilment
of the requirements for the degree of
Masters of Engineering

School of Materials Science and Engineering
University of New South Wales
Sydney, Australia
September, 2008

CANDIDATE'S DECLARATION

'I hereby declare that this submission is my own work and to the best of my knowledge it contains no materials previously published or written by another person, or substantial proportions of material which have been accepted for the award of any other degree or diploma at UNSW or any other educational institution, except where due acknowledgement is made in the thesis. Any contribution made to the research by others, with whom I have worked at UNSW or elsewhere, is explicitly acknowledged in the thesis. I also declare that the intellectual content of this thesis is the product of my own work, except to the extent that assistance from others in the project's design and conception or in style, presentation and linguistic expression is acknowledged.'

Lydia Kemal

Date:

ACKNOWLEDGEMENTS

The candidate for ME degree gratefully acknowledges the financial support from the Australia Research Council (ARC) through the ARC Centre of Excellence for Functional Nanomaterials.

I extremely appreciate my supervisor, Professor Aibing Yu, for his guidance and help during the course of this research. I would like to thank my co-supervisor, Dr. Xuchuan Jiang, for his time, assistance, and guidance during my study.

At the same time, I would like to thank those group members including Dr. Qinghua Zeng, Mr. Jeffery Yue and Mr. Kenneth Wong for their valuable discussion, and Dr. Ruiping Zou for her time and efforts; as well as the staff in the School of Materials Science Engineering at UNSW, including Cathy Lau, Lana Strizhevsky, Flora Lau, and Guangqing Zhang for their help in the past two years.

Also to my best friend Mr. Auppatham Nakaruk, my family, my brother Mr. Indra Kemal and my boyfriend Mr. Felix Yakub from whom I have gained much help, and continuous support throughout my study.

ABSTRACT

This thesis focuses on the shape-controlled metal nanoparticles for functional applications, covering the synthesis, characterization and optical properties. Three parts are mainly involved in this work, including, gold worm-like nanoparticles, silver nanoplates, and silver induced selenium nanowires. The first part focuses on a facile synthesis method for shape control of gold nanoparticles by treating an aqueous solution of chloroauric acid with sodium citrate and poly(vinyl pyrrolidone) (PVP), in which those worm-like nanoparticles were investigated by various advanced experimental characterizations combining density function theory (DFT) calculation. These nanoparticles can be used for optical sensing detection of ions in aqueous system. The second part involves the synthesis, growth, and optical properties of silver nanoplates (triangles and circular discs). Such nanoplates could be synthesized by a self-seeding co-reduction method at ambient conditions. In particular, molecular dynamics simulation is used to quantify the interaction energies between surfactant molecules and different facets of silver crystal. Such molecular information, together with measurements using x-ray diffraction (XRD), transmission electron microscopy (TEM), atomic force microscopy (AFM) and ultraviolet-visible (UV-vis) spectroscopy, has proven to be useful for understanding the growth mechanisms of silver nanoplates. The third part focuses on the template of silver nanoparticles for generating trigonal selenium (t-Se) nanowires. This technique exhibits some advantages in fabricating t-Se nanostructures, including no need to use stabilizers and sonichemical process and all operations being proceeded in aqueous media and at room temperature. Particularly it can successfully achieve the transformation from amorphous α -Se to crystalline t-Se in aqueous solution and this method would be useful for generating one-dimensional nanostructures with similar lattice parameter(s). It is considered that the technique for the shape-controlled metal nanoparticles can at least partially, be extended to other nanomaterials for functional applications.

Table of Contents

CHAPTER 1

Introduction.....	1
-------------------	---

CHAPTER 2

Literature Review.....	3
2.1 Properties of Metal Particles.....	3
2.1.1 Optical Absorption of Metal Spheres.....	3
2.1.2 Optical Absorption of Metal Ellipsoids.....	7
2.1.3 The Effect of Aspect Ratio.....	9
2.1.4 The Effect of the Refractive Index of the Solvent.....	10
2.1.5 The Effect of A Shell Layer.....	12
2.1.6 The Effect of Particular Orientation.....	14
2.1.7 Nonradiative Relaxation in Metal Nanostructured Systems.....	17
2.1.7.1 Nonradiative Relaxation of Gold.....	17
2.1.7.2 Theoretical Modeling of Optical Response.....	18
2.1.7.3 Electron-Electron Thermalization in Gold Nanoparticles.....	19
2.1.7.4 Electron-Phonon Relaxation in Gold Nanoparticles.....	21
2.1.7.5 Electron-Phonon Relaxation Rate.....	24
2.1.7.6 Other Properties of Gold Nanoparticles.....	27
2.2 Synthesis Methods.....	32
2.2.1 Irradiation Methods.....	32
2.2.1.1 Sonochemistry Method.....	32
2.2.1.2 Thermolysis Method.....	33
2.2.1.3 Laser Photolysis Method.....	33
2.2.2 Chemical Synthesis.....	34
2.2.2.1 Solvothermal Method.....	34
2.2.2.2 Hydrochemical method.....	37
2.2.2.3 Photochemical method.....	37
2.2.2.4 Electrochemical method.....	40
2.2.2.5 Microwave-Polyol method.....	44

2.2.2.6	Gamma irradiation.....	48
2.2.2.7	Ultrasonication.....	50
2.2.2.8	Biochemical method: Aspartate Reduction.....	53
2.2.2.9	Non-hydrochemical method.....	54
2.2.2.9.1	Polyol Reduction method.....	54
2.2.2.9.2	Template method.....	56
2.3	Growth Mechanism.....	60
2.3.1	Electrical-field Induced Mechanism.....	60
2.3.2	Light-induced Reconstruction Mechanism of Metal Nanoparticles.....	61
2.3.3	Stack-fault Mechanism.....	62
2.4	Applications.....	65
2.4.1	Biomedical application.....	65
2.4.1.1	Gene Delivery.....	65
2.4.1.2	Detection of Cancer with Gold Nanocages.....	66
2.4.2	Sensing Application.....	68
2.4.3	Wave-Guiding Materials.....	68
2.4.4	Catalysis Reaction.....	69
2.4.4.1	Homogenous Catalysts.....	69
2.4.4.2	Heterogenous Catalysts.....	70
2.5	Conclusions.....	71
CHAPTER 3		
Experimental Work.....		
3.1	Gold Nanostructure Synthesis.....	72
3.1.1	Chemicals.....	72
3.1.2	Synthesis of worm-like gold nanoparticles.....	72
3.1.3	Sensing detection of anions.....	72
3.1.4	Density Function Theory (DFT) simulations.....	73
3.2	Silver Nanoplates Synthesis.....	73
3.2.1	Chemicals.....	73
3.2.2	Synthesis of silver nanoplates.....	74
3.2.3	Numerical method.....	74

3.3 Selenium Nanowires Synthesis.....	74
3.3.1 Chemicals.....	74
3.3.2 Synthesis of silver nanoparticles.....	75
3.3.3 Synthesis of selenium nanowires.....	75
3.4 Characterization.....	75
CHAPTER 4	
Results and Discussion.....	76
4.1 Au Nanostructures.....	76
4.1.1 Shape/Size Worm-like gold nanoparticles.....	76
4.1.2 Optical Properties.....	79
4.1.3 Effects of Experimental Parameters.....	80
4.1.3.1 Reaction temperatures.....	80
4.1.3.2 Surfactants of AOT and CTAB.....	83
4.1.3.3 PVP-AuCl ₄ ⁻ and citrate-AuCl ₄ ⁻ systems.....	86
4.1.4 Particle Growth Mechanism.....	87
4.1.5 Sensing Detection of Anions.....	91
4.1.6 Conclusions.....	93
4.2 Silver Nanoplates.....	95
4.2.1 Shape and Size.....	96
4.2.2 Size Distributions.....	100
4.2.3 Effect of Surfactants.....	102
4.2.4 Effect of Reducing Agents.....	104
4.2.5 Theoretical Simulation.....	105
4.2.5.1 Adsorption of surfactant.....	105
4.2.5.2 Formation of silver nanoplates.....	107
4.2.5.3 Stabilization of triangular silver nanoplates.....	108
4.2.5.4 Formation of silver nanospheres.....	109
4.2.5.5 Atom distributions at silver surface.....	110
4.2.6 Gold Nanorings.....	112
4.2.7 Conclusions.....	114
4.3 Au Induced Selenium Nanowires.....	116

4.3.1	Shape and Size of Silver Nanoprticles.....	116
4.3.2	Composition.....	119
4.3.3	Optical Properties.....	120
4.3.4	Effect of Various Parameters.....	121
4.3.4.1	Metal nanoparticles.....	121
4.3.4.2	Shape of silver nanoparticles.....	122
4.3.4.3	Induced reaction time.....	124
4.3.4.4	Molar ratio of Ag ⁰ to SeO ₃ ²⁻ ions.....	125
4.3.5	Growth Mechanism.....	127
4.3.6	Conclusions	129

CHAPTER 5

Conclusions and Future Work.....	130
----------------------------------	-----

CHAPTER 6

References.....	132
Reply to the comments from Examiners	140

Caption of Figures

Figure	Page
2.1 Depolarization of a prolate spheroid vs. eccentricity, e , along the major axis, x and the two equivalent minor axes, y and z (left). The real and imaginary parts of the dielectric function of bulk gold (right).	8
2.2 The ratio of the dielectric function of the material to the medium for different polarization factors.	9
2.3 Experimental plot of the surface plasmon longitudinal band position vs. aspect ratio for pure gold rods in water. This linear correlation is fortuitous. Over large aspect ratio values, the Gans formula predicts a slow curvature. Furthermore, retardation effects and radiation damping become more prominent for larger aspect ratios. These effects are not included in the basic ellipsoid model.	10
2.4 The color of gold rods and the respective micrographs. The color changes take place for very small changes in mean aspect ratio.	10
2.5 Experimental spectra of gold nanorods in different solvents (left) and change in the longitudinal plasmon band position with refractive index (right).	11
2.6 Calculated spectra for gold ellipsoids with an aspect ratio of 3.5 in different media as a function of the medium refractive index. There is a drastic red-shift with increasing solvent polarizability. The peak in extinction coefficient occurs because at longer wavelengths, there is increasing damping, i.e., a rise in the value of ϵ'' , see Figure 2.1.	13
2.7 Calculated spectra for a gold rod in water. The rod has dimensions 12 nm \times 30 nm. The calculation shows the shift in SPL for 2, 4, 6, and 8 nm silica shells with an assumed refractive index of $n = 1.5$.	14
2.8 Calculated spectra of vertically oriented gold nanorods with aspect ratio of 4.0 in water. The spectra are calculated for various angles, and show that there is an isosbestic point at about 530 nm.	15
2.9 (a) TEM image of gold triangular nanoplates; (b) Self-assembly model of rhombic nanostructures.	16

2.10	(a) TEM image of pairs of gold triangular nanoplates and (b) corresponding dipole assembly model.	16
2.11	(a) TEM image of rhombic nanostructure and (b) corresponding dipole assembly model.	17
2.12	Electron-electron thermalization in spherical gold nanoparticles. The plasmon bleach recovery of 22-nm gold nanoparticles probed at 530 nm is plotted against a logarithmic scale.	20
2.13	Steady-state absorption and transient absorption spectra of 15-nm gold nanoparticles after excitation with 400-nm laser light. The series of spectra corresponds to different delay times between the pump and probe pulses.	21
2.14	Temporal evolution of the plasmon bleach spectra at certain wavelengths: (□) 480 nm; (0) 520 nm; (O) 550 nm.	22
2.15	Transient absorption data obtained for 60 nm diameter Au particles (solid line) and signal calculated with a distribution of cosine functions with frequencies and weights determined by the measured size distribution of the sample (dashed line).	23
2.16	Transient absorption spectra of 15-nm gold nanoparticles after excitation at 400 nm with 100-fs laser pulses recorded at different delay times. The left inset shows the decrease in the bleach line width with increasing delay time. The line width was obtained by fitting a Lorentzian function (s) to the experimental spectra (O). The right inset illustrates the decay of the transient bleach signal monitored at 2.38 eV.	24
2.17	Optical response of gold nanorods after excitation with a femtosecond laser pulse. Transient absorption (s) and steady-state absorption spectrum (- - -) of gold nanorods with a mean aspect ratio of 3.8 are shown. Both spectra are scaled to arbitrary units. The transient absorption spectrum was recorded at a delay time of 6 ps after excitation with 100-fs laser pulses having a center wavelength of 400 nm.	25
2.18	Size and shape dependence of the electronphonon relaxation time. Plasmon bleach recovery was measured for 48- and 15-nm gold nanoparticles and for	25

the transverse and longitudinal modes of gold nanorods with an average aspect ratio of 3.8 (from top to bottom).	
2.19 Pump power dependence of the electronphonon relaxation time in gold nanoparticles. The Plasmon bleach recovery of 15-nm gold nanoparticles is probed at 520 nm after excitation at 400 nm with laser pulses of various energies.	27
2.20 Relationship between the melting points and the sizes of gold (top) and CdS nanoparticles (bottom).	28
2.21 <i>I-U</i> characteristic of ideal single electron transport, where Coulomb blockade is shown as the step function.	30
2.22 (a) Field emission scanning electron micrograph of a lead structure before the nanocrystals are introduced. The light gray region is formed by the angle evaporation and is 10 nm thick. The darker region is from a normal angle evaporation and is 70 nm thick. (b) Schematic cross section of nanocrystals bound via a bifunctional linker molecule to the leads. Transport between the leads occurs through the mottled nanocrystal bridging the gap.	31
2.23 <i>I -V</i> characteristic of a 5.8-nm diameter Au nanocrystal measured at 77 K. Several Coulomb steps of period $\Delta V_{sd} \approx 200$ mV can be seen.	31
2.24 Taping-mode AFM images of the species formed in a solution irradiated with γ rays (1.5 kGy) and then deposited on highly ordered pyrolytic graphite (HOPG) 30 days after the irradiation and dried under a mild N_2 stream for visualization. The solution contains 10^{-3} mol.L ⁻¹ AuIII and poly(vinyl alcohol) but no alcohol. (A) Height-mode (z range 80.0 nm) image and (B) phase (z range 42.2°) image, run simultaneously on the same area of the sample. (C, D) Close-up images showing the same area as in (A) and (B), respectively.	32
2.25 UV-vis spectra (A) and TEM images and size distributions (B).	33
2.26 Thin films of FeCo, CdSe, CdS, Co and Ag formed on glass microslides prepared under solvothermal conditions.	34
2.27 (A) Bright-field image of FeCo nanoparticles drop-cast on a carbon-coated Cu grid showing particle size around 5–6 nm. (B) Bright-field image of	35

FeCo film directly grown on a Cu grid under the same condition as in (A), having average particle size around 9–10 nm. (C) Bright-field image showing a FePt nanoparticle film formed on the 100 plane of a NaCl crystal. The particle size was found to be around 1–1.5 nm. (D) Gold nanoparticle film formed directly on a carbon-coated TEM grid with particle size around 2–3 nm.

- 2.28** (a) Image of photochemically prepared gold nanorods solution, and (b) corresponding UV-vis spectrum. The leftmost solution was prepared with no silver ion addition. The other solutions were prepared with addition of 15.8, 31.5, 23.7, 31.5 μL of silver nitrate solution, respectively. The middle solution was prepared with longer irradiation time (54 h) compared to that for all other solutions (30 h), and the transformation into shorter rods can be seen. 37
- 2.29** Transmission electron microscopy (TEM) images of gold nanorods prepared with (a) 15.8 μL , (b) 23.7 μL , (c) 31.5 μL of silver nitrate solution. The bar indicates 50 nm. (d) High-resolution image of a gold nanorod. 38
- 2.30** (a) Schematic diagram of the set-up for preparation of gold nanorods via the electrochemical method containing; VA, power supply; G, glassware electrochemical cell; T, teflon spacer; S, electrode holder; U, ultrasonic cleaner; A, anode; C, cathode. (b) TEM micrographs of Au nanorods with different aspect ratios 2.7 (top) and 6.1 (bottom). Scale bars represent 50 nm. 41
- 2.31** (a) High-resolution TEM image of a gold nanorod showing the faceted crystal structure of the rod. The inset is the electron diffraction pattern, which confirms its single crystalline structure. (b) Dark-field TEM image of a gold nanorods. Cross-section and the corresponding profile of crystal thickness (c) as well as the structural model (d) proposed by Wang et al. 42
- 2.32** (a) TEM image of a long nanorods; (b) the corresponding electron diffraction pattern; (c) the proposed structure model for long gold nanorods. 43
- 2.33** TEM photographs of gold nanostructures obtained by MW heating after 2 min. $\text{HAuCl}_4\cdot 4\text{H}_2\text{O}/\text{PVP}$ molar ratios were (a) 1.2×10^{-3} , (b) 4.7×10^{-3} , (c) 44

- 9.3x10⁻³, and (d) 1.9x10⁻² at a PVP concentration of 1.03 mmol/dm³, and (e) 9.3x10⁻³ at a PVP concentration of 2.06 mmol/dm³, (f) Electron diffraction pattern of the longest nanowire shown in panel (e).
- 2.34** UV-vis absorption spectra of reagent solutions of H₂AuCl₄·4H₂O/EG/C₁₆TAB and H₂AuCl₄·4H₂O/EG/C₁₆PC and product solutions of H₂AuCl₄·4H₂O/EG/C_nTAB (n =14, 16) and H₂AuCl₄·4H₂O/EG/C₁₆PC after MW irradiation for 2 min. 45
- 2.35** Possible formation processes of Au nanoparticles prepared by the MW-polyol method with the assistance of cationic surfactants C_nTAB and C₁₆PC. 48
- 2.36** The TEM morphology micrograph of the Ag-adopted SiO₂ film under irradiation by γ-ray for 4 h, the inserted image is the corresponding selected area electron diffraction pattern. 48
- 2.37** TEM images of Ag nanoparticles containing (a) 1.0 x 10⁻³ M; (b) 4.0 x 10⁻⁴ M; (c) 2.0 x 10⁻⁴ M and (d) 1.2 x 10⁻⁴ M silver and histograms of particle size distributions (inset). 49
- 2.38** Optical absorption spectra for the mesoporous SiO₂ film without doping (a) (sample 0); the mesoporous SiO₂ film soaked in 0.01, 0.05 and 0.1 M AgNO₃, respectively, and γ-irradiated for 4 h (b–d) (samples 1–3) and the annealed sample (e) (sample 4). 50
- 2.39** Schematic illustration of an ultrasonically irradiated process 51
- 2.40** (A) Time evolution of optical absorption spectra for the aged irradiated sample (5 mL, ultrasonic-irradiated for 120 min, and then aged at room temperature for 7 days) after an addition of 0.1 mL of 25 mM H₂AuCl₄ solution. (B) The optical spectra for the samples with an addition of different amounts of H₂AuCl₄ after 7 days. (C-F) The TEM images of Au nanoprisms after 7 days for the samples, respectively, are corresponding to the addition of 0.1, 0.3, 0.5, and 1 mL of 25 mM H₂AuCl₄ solution to a 5 mL aliquot aged sample. 52
- 2.41** Typical TEM images of a sample prepared from a reaction solution containing aspartate, showing the high- (a) and slightly lower- (b) degree assembled nanoplates during the evaporation of solvent. The representative 53

images of individual hexagonal and truncated triangular nanoplates are shown in (c) and (d). The insets show the selected-area electron diffraction patterns. The scale bars are 200 nm.

- 2.42** TEM images and size distributions of samples (2 g of PVP): (a) A1; (b) A2; (c) A3; (d) A4; (e) A5 (scale bar: 50 nm (A1–A4), 1 μm (A5)). 55
- 2.43** Reverse micelle and normal micelle structures. 56
- 2.44** Schematic phase diagram of surfactant-oil-water systems showing a variety of self-assembled structures. 57
- 2.45** TEM images obtained after synthesis at $[\text{Cu}(\text{AOT})_2] = 5 \times 10^{-2} \text{ M}$, $w = 4, 20, 34, 40$, respectively. 58
- 2.46** TEM images of the reacting colloids with 3 h acid treatment MWCNTs exposed in X-ray for 1, 10, and 30 min as shown in (a), (b), and (c), respectively. 59
- 2.47** TEM images of the reacting colloid for 6 h acid treatment MWCNTs exposed to X-ray for 1, 10, and 30 min, as shown in (a), (b), and (c), respectively. The element characterization by EDS is shown in (d). 59
- 2.48** Illustration of the structural transformation process from nanorod to gold nanodot. 62
- 2.49** Typical SAED patterns that show the $1/3\{422\}$ forbidden reflections. 63
- 2.50** (A) TEM image of the silver nanodisk taken in side view, showing the contrast from (111) stacking faults and a preferential growth along the stacking faults. (B) A typical SAED pattern of silver nanodisk at 100 kV in the [011] orientation (side view). 64
- 2.51** Spatially selective binding of DNA plasmids and transfer into multicomponent nanorods. (a) Illustration of nanorod functionalization. At this step, nanorods are incubated with the 3-[(2-aminoethyl) dithio] propionic acid (AEDP) linker (1). The carboxylate end-group binds to the Ni segment. The disulphide linkage acts as a cleavable point within the spacer to promote DNA release within the reducing environment of the cell. Plasmids are bound by electrostatic interactions to the protonated amines presented on the surface of the nickel segment (2). CaCl_2 compacts the 65

surface-immobilized plasmids (3). Rhodamine-conjugated transferrin is selectively bound to the gold segment of the nanorods (4). (b) Confirmation of selective functionalization of nanorods is observed by light and fluorescent microscopy, in which (1) Light microscope image of dual functionalized Au/Ni nanorod 20 μm long; (2) Fluorescence image of the rhodamine-tagged (633 nm) transferrin on the Au segment; (3) Fluorescence image of the Hoechst-stained (350/450 nm) plasmids on the Ni segment; and (4) Fluorescent overlay image combining b2 and b3.

- 2.52** Transformation of 30 nm Ag nanocubes into Au/Ag alloyed nanoboxes and nanocages results in a continuous shift of their surface plasmon resonance (SPR) peak from 400 to 900 nm, which is in the transparent window of biological tissue. The SPR peak position is determined by the molar ratio between HAuCl_4 and Ag involved in the replacement reaction. Insets show TEM images of the cubes and cages; scale bar in each Figure 2.52 represents 20 nm. 67
- 4.1** Typical solution color of the wormlike Au nanoparticles. 76
- 4.2** TEM images of gold worm-like nanoparticles prepared at 50 $^\circ\text{C}$ with different reflux heating times at 95 $^\circ\text{C}$: (A) 10 min; (B) 30 min; (C) 45 min; and (D) 60 min. The inset of Figure 4.2D is showing the corresponding electron diffraction pattern of nanoparticles. 77
- 4.3** (A) HRTEM image of gold worm-like nanoparticles; (B) HRTEM image of a short nanorod; and (C) an L-shaped gold particle, along with the interplanar distance around 0.285 nm. 78
- 4.4** UV-vis spectra of the samples corresponding to different reflux heating times: (a) 10 min; (b) 30 min; (c) 45 min; and (d) 60 min. 79
- 4.5** TEM images of gold nanoparticles prepared under the same preheating time (30 min) but different preheating temperatures: (A) 40 $^\circ\text{C}$; (B) 60 $^\circ\text{C}$; and (C) 70 $^\circ\text{C}$. 80
- 4.6** Solution color after 60 minutes refluxing time at 95 $^\circ\text{C}$ but at different preheating time, a. 10, b. 30, c. 45 and d. 60 min 81

4.7	TEM images of gold nanoparticles prepared by preheating at 50 °C for different times: (A) 10 min; (B) 30 min; (C) 45 min; and (D) 60 min, following by immersing into cold water (~5 °C) for comparing the effect of temperature on the seed and hence the final morphology of products.	82
4.8	Size distribution of different samples preheated at different time (AA) 10 min; (BB) 30 min; (CC) 45 min; and (DD) 60 min	83
4.9	UV-vis spectra of the 4 samples shown in Figure 4.7 indicating they have the similar optical absorption profile.	84
4.10	TEM images of Au nanoparticles prepared by using different types of surfactants: (A) AOT; (B) CTAB and (C) SDSN. The electron-diffraction pattern (inset of Figure 4.10A, B and C) confirming that the particles are crystalline.	85
4.11	(A) TEM image of gold seeds obtained from the preheated PVP-AuCl ₄ ⁻ solution at 50 °C for 60 min, and the inset showing the corresponding electron diffraction pattern; (B) TEM image of gold nanoparticles obtained from the preheated citrate-AuCl ₄ ⁻ solution at 50 °C for 60 min, and the inset showing the corresponding electron diffraction pattern; and the corresponding UV-vis spectra shown in (C) and (D), respectively.	87
4.12	A scheme illustrating the formation of gold worm-like nanoparticles through the fusion along Au{111} planes with different lengths (e.g., I, II, and III).	89
4.13	(A) The simulation model showing that PVP interacts with each gold crystalline plane (i.e., 111, or 110, or 100); and (B) the planar electron density profile of the PVP/Au system indicating the electrostatic interactions between PVP and Au. The atoms marked with different color as followings; Au (yellow), H (white), O (red), N (blue), and C (grey).	90
4.14	The sensing detection of anions by using gold nanoparticles monitored by UV-vis spectrum: (A) the sensitivity of Au worm-like particles towards sulfide ions with different contents; (B) the sensitivity of Au spheres towards sulfide ions with different contents.	92
4.15	Schematic showing the procedures in the self-seeding coreduction approach.	95

- 4.16** TEM images ((A)–(F)) showing the evolution of the silver nanoparticles from unshaped particles to triangular plates, and finally circular discs, over 1, 3, 5, 10 min, 10 h, and 100 h, respectively. The inset of Figure 4.16F shows a TEM image of the Moiré fringe pattern formed by stacking two nanodiscs. 96
- 4.17** The UV–vis spectra corresponding to the silver nanocrystals obtained at different times: (A) 1 min, (B) 3 min, (C) 5 min, (D) 10 min, (E) 10 h, and (F) 100 h, respectively. 98
- 4.18** (A) A representative TEM image of one individual silver nanodisc with its selected area electron diffraction (SAED) pattern (inset). In the SAED pattern, the circled spot, boxed spot, and spot circumscribed by triangle correspond to $(1/3)\{422\}$, $\{220\}$ and $\{311\}$ Bragg reflections with lattice spacings of 2.5, 1.44 and 1.23 °Å, respectively. (B) The HRTEM image shows the lattice spacing 2.36 °Å corresponding to Ag $\{111\}$ facets. (C) AFM image (side view) of the silver nanodiscs obtained over 100 h. (D) The thickness of the nanodisc is estimated to be ~2.3 nm. 99
- 4.19** TEM images and the size distributions of circumference and surface area showing the transformation from triangular silver plates (A–C) to circular discs (D–F). 101
- 4.20** Shape transformation of silver nanoparticles under various conditions: (a) triangular silver nanoplates formed after ageing for 10 min under AOT molecules; (b) disc-like silver nanoplates formed after further ageing for 48 h; (c) silver nanospheres formed after further ageing for 48 h under the addition of CTAB molecules; (d) triangular silver nanoplates remaining after ageing for 48 h under the addition of C₁₂SH molecules. 102
- 4.21** The corresponding UV–vis spectra to the silver nanoparticles: (A) triangular silver nanoplates formed after ageing for 10 min under AOT molecules; (B) disc-like silver nanoplates formed after further ageing for 48 h; (C) silver nanospheres formed after further ageing for 48 h under the addition of CTAB molecules; (D) triangular silver nanoplates remaining after ageing for 48 h under the addition of C₁₂SH molecules. 103

- 4.22** The effect of the reducing agents on the shape of silver nanoparticles: (A) NaBH_4 , (B) citric acid + NaBH_4 , (C) L-ascorbic acid + NaBH_4 , and (D) citric acid + L-ascorbic acid. 104
- 4.23** Molecular models of: (a) silver crystal plane and surfactants; (b) silver crystal plane only; (c) surfactants only. Here the crystal plane (in balls) is Ag (100) and the surfactant is AOT which contains atoms of sulfur (yellow), oxygen (red), grey (carbon), white (hydrogen) and sodium (purple). 106
- 4.24** Evolution of AOT molecular adsorption on silver crystal surface (100) at time: (a) 0 ps; (b) 5 ps; (c) 20 ps, (d) 50 ps. Here the silver crystal plane (100) is expressed as dots and AOT is expressed as sticks containing atoms of sulfur (yellow), oxygen (red), grey (carbon), white (hydrogen) and sodium (purple). 106
- 4.25** Evolution of C_{12}SH molecular adsorption on AOT coated silver nanoparticle surface (100) at time: (a) 0 ps; (b) 5 ps; (c) 20 ps, (d) 50 ps. Here a silver crystal plane (100) is expressed in dots while AOT and C_{12}SH are expressed in sticks containing atoms of sulfur (yellow), oxygen (red), grey (carbon), white (hydrogen) and sodium (purple). 109
- 4.26** Atom density profiles of AOT surfactant on silver surfaces: Ag (100) (top), Ag (110) (middle) and Ag (111) (bottom). 110
- 4.27** Atom density profiles of C_{12}SH surfactant on silver surfaces: Ag (100) (top), Ag (110) (middle) and Ag (111) (bottom). 111
- 4.28** Atom density profiles of CTAB surfactant on silver surfaces: Ag (100) (top), Ag (110) (middle) and Ag (111) (bottom). 112
- 4.29** (A) TEM image and the inset SAED pattern of gold nanorings, (B) the XRD patterns of gold nanorings (a) and silver nanodiscs (b), and (C) the corresponding UV-vis spectra of gold nanorings (dotted line) and Ag nanodiscs (solid line). 113
- 4.30** TEM image and the corresponding EDS pattern of silver nanoparticles. 116
- 4.31** TEM image of Se nanowires (A), one individual Se nanowire and the SAED patterns from different parts (B), HRTEM image of the Se nanowire shown 118

in Figure 4.31B (C), and the enlarged HRTEM images from two squared parts of the Se nanowire (D and E).

- 4.32** (A) TEM image of an individual bending Se nanowire; and (B) its HRTEM with a bending angle of $\sim 15^\circ$. 119
- 4.33** The XRD (A) and EDS (B) patterns of the as-prepared Se nanowires. 120
- 4.34** UV-vis spectra of Ag nanoparticles (a), the as-synthesized Se nanostructures (b), Ag_2Se nanowires (c), and pure Se nanowires (d). 120
- 4.35** TEM images of metal nanoparticles: (A) Au; (B) Cu; (C) Pt; and (D) Pd; and the corresponding selenium nanostructures induced by metal nanoparticles: (E-H). 121
- 4.36** (A) TEM images of multiple-shape silver nanoparticles; (B) and (C) the etched silver particles by hydrazine; and (D) the corresponding Se nanowires induced by the freshly formed silver nanoparticles. 123
- 4.37** (A) TEM image of silver nanoplates; (B) the corresponding slim Se nanobelts and a high magnification inset of image (B); (C) small silver nanoparticles; and (D) the corresponding Se nanowires. 124
- 4.38** TEM images of time-dependent growth of selenium nanostructures at different stages: (A) 3 h; (B) 24 h; and (C) 48 h. 124
- 4.39** TEM images showing the influence of the molar ratios of silver to selenium ions on the formation of Se nanostructures: (A) 1/4,000; (B) 1/800; (C) 1/230; and (D) 1/115. 125
- 4.40** UV-vis spectra of Ag-Se nanoparticles with different molar ratio Ag to Se (a) 1/4000, (b) 1/800, (c) 1/230 and (d) 1/115. 126
- 4.41** Schematic diagram illustrating the growth mechanism of Se nanowires induced by silver nanoparticles. 127
- 4.42** TEM images of the as-synthesized Se nanostructures rooted on the surface of $\text{Ag}_2\text{Se}/\text{Ag}$ nanoparticles along one, two or more directions. 128

Caption of Tables and Schemes

Table/Scheme	Page
Table 2.1 Characteristic of transition and noble metals nanoparticles using solvothermal technique.	36
Table 2.2 Synthesis conditions and characteristics for PVP-stabilized Au colloids	54
Scheme 2.1 Mechanism of gold rod formation.	60
Scheme 4.1 Schematic growth mechanism of Au worm-like nanostructure.	88
Table 4.1 The calculated interaction energies (kcal mol^{-1}) for various surfactant–silver plane systems.	107

CHAPTER 1

Introduction

Nanostructures have been extremely attractive because of their unique properties (e.g., optical, electronic, magnetic and chemical properties) and potential applications in nanoscience and nanotechnology. ^[1-3] Important scientific and technological advances based on understanding and control of properties and processes at the scale of atoms and molecules—the nanometer scale—are taking place in laboratories around the world. The ability to control materials at the nanoscale is already leading to novel materials and improved performance and other characteristics in existing products. Over the longer term, nanotechnology promises even more revolutionary advances with potential impacts on nearly every industrial sector, including energy, health care, defense, transportation, and electronics.

The novelty of nanoscale materials arises from the fact that with decreasing size, the properties of materials change. Many attempts have been made by the researchers in the world to discover and develop new synthesis methods and characterization techniques. To control shape and size of nanoparticles become more attractive due to the heavily shape/size-dependent functional properties, particularly for noble metallic nanoparticles.

This thesis will focus on the shape-controlled synthesis of gold and silver nanoparticles through developing simple but effective methods, facilitated by advanced experimental techniques including transmission electron microscopy (TEM), high-resolution TEM (HRTEM), X-ray diffraction (XRD), and ultraviolet-visible (UV-vis) spectrometer.

More interestingly, various theory methods are used in this study to understand the fundamentals of underlying particle growth and shape control, such as density function theory (DFT) for calculating the binding energy of atoms, and molecule dynamics (MD) method for calculating the interaction energies between surfactant molecules and metallic crystallographic surfaces. They will provide quantitative information to understand

particle growth and shape control at an atom/molecule scale. Such a comprehensively experimental and theoretical study and the consequent findings will be useful for shape controlled synthesis of nanoparticle with desirable functional properties and applications in different area, such as chemical usage, biomedical, electronic, materials science industries, ionic sensing and catalysis.

This thesis consists of six chapters. Chapter 1 will give a brief introduction to this project, followed by the literature review on chapter 2, in which the research background, the problems or limitations experienced in previous studies and the motivation of this work will be outlined. Chapter 3 briefly introduces the developed synthesis methods of gold worm-like particles, silver nanoplates, and silver induced selenium nanowires, as well as the characterization techniques and the theoretical simulation methods (e.g., density function theory, DFT, and molecular dynamics, MD, simulations). Chapter 4 provides the details of research results and discussion, covering the growth of gold worm-like nanoparticles, silver nanoplates and silver induced selenium nanowires, understood by DFT and MD simulations; the optical properties of gold, silver, and selenium; and the functional application in ionic sensing detection using gold nanoparticles. Chapter 5 summarizes the research findings in this work, including newly developed synthesis strategies, and theoretical simulations for fundamentally understanding the growth mechanism at a molecular level and potential applications; followed by references on chapter 6.

CHAPTER 2

Literature review

In this section, some of the key attributes of spherical and non-spherical particles are reviewed. To understand the basic optical properties is important for a few distinct reasons. First, small particles may have electronic, crystallographic, mechanical or catalytic properties that are largely different from their bulk material, which can be monitored through optical measurements. Secondly, spectroscopic measurements are often the easiest methods for monitoring surface processes such as dissolution and precipitation, adsorption and electron transfer. For example, one of the current efforts has been made in pushing analytical chemistry towards single molecule detection and identification. This could be feasible by using surface enhanced Raman spectroscopy (SERS) of molecules on anisotropic metal surfaces, and various geometries for achieving this have been proposed in the past years. Furthermore, there is growing recognition of the opportunity to build nanoscale blocks, photonic crystals and other functional structures using “bottom-up” assembly due to their new or complicated properties. This part aims only at providing the foundation for interpreting experimental data included in previous studies. ^[4-8] Several comprehensive reviews of the optical properties of metal particles have been given to discuss electromagnetic theory, size effects, ^[4, 9, 10] the light scattering features or the surface chemical perturbations. ^[5] Textbooks are also given by van der Hulst, ^[6] Kerker ^[7] and Bohren and Huffman. ^[8] More recent work has involved the development of robust numerical solutions to the light scattering and extinction by non-spherical structures including 2D arrays. ^[11] The review by Kelly et al. ^[12] provides an excellent overview, while computational aspects are reviewed by other researchers. ^[13-15]

2.1 Properties of Metal Particles

2.1.1 Optical Absorption of Metal Spheres

Solutions containing small nanocrystals are particularly concerned in this section. These particles do not sediment and the solution is optically and spatially homogeneous. In a

dilute colloidal solution containing N particles per unit volume, the measured attenuation of light of intensity I_0 , over a path length x cm in a spectrophotometer is given in differential form as: ^[16]

$$\frac{dI(x)}{dx} = -NC_{\text{ext}}I(x) \quad (2.1)$$

which shows that the rate of loss of photons is proportional to the light intensity at distance x into the medium, and also to the number density of light extinguishing particles. Integration gives the solution absorbance:

$$A = \log_{10} \frac{I_0}{I(x)} = \frac{NC_{\text{ext}}x}{2.303} \quad (2.2)$$

where C_{ext} is the extinction cross-section of a single particle. For spherical particles with a wavelength-dependent dielectric function $\varepsilon(\lambda) = \varepsilon'(\lambda) + i\varepsilon''(\lambda)$, embedded in a medium of dielectric function ε_m , C_{ext} is given by: ^[6-8]

$$C_{\text{ext}} = \frac{2\pi}{k^2} \sum_{n=1}^{n=\infty} (2n+1) \text{Re}\{a_n + b_n\} \quad (2.3)$$

$$k = 2\pi \frac{\sqrt{\varepsilon_m}}{\lambda}, \quad (2.4)$$

and a_n and b_n are the scattering coefficients, which are functions of the particle radius and λ in terms of Ricatti–Bessel functions. The extinction cross-section of a particle is often normalized to give the extinction cross-section per unit area:

$$Q_{\text{ext}} = \frac{C_{\text{ext}}}{\pi R^2} \quad (2.5)$$

Conventionally, chemists measure the extinction coefficient of a solution in units of $\text{M}^{-1} \text{cm}^{-1}$, where the concentration is the molar concentration of metal atoms. For particles of radius R (cm), this quantity is related to Q_{ext} by:

$$\varepsilon(\text{M}^{-1} \text{cm}^{-1}) = \frac{3 \times 10^{-3} V_m Q_{\text{ext}}}{(4 \times 2.303 R)} \quad (2.6)$$

where V_m ($\text{cm}^3 \text{mol}^{-1}$) is the molar volume of the metal. Bohren and Huffman provided various approximations that may be used instead of the full series expansion.^[8] In particular, for very small particles where $kR \leq 1$, only the first few terms are important in these equations

$$a_1 = -\frac{i2x^3}{3} \frac{m^2 - 1}{m^2 + 2} - \frac{i2x^5}{5} \frac{(m^2 - 2)(m^2 - 1)}{(m^2 + 2)^2} + \frac{i4x^6}{9} \left[\frac{m^2 - 1}{m^2 + 2} \right]^2 + O(x^7) \quad (2.7)$$

$$a_2 = -\frac{i2x^5}{15} \frac{m^2 - 1}{2m^2 + 2} + O(x^7) \quad (2.8)$$

$$b_1 = -\frac{ix^5}{45} (m^2 - 1) + O(x^7) \quad (2.9)$$

$$b_2 = O(x^7) \quad (2.10)$$

Here m is the refractive index of the material relative to the medium, i.e., $m = n/n_{\text{med}}$ and $x = kR = 2\pi n_{\text{med}} R / \lambda$. If we retain just the first term in a_1 , then Eq. (2.3) becomes:

$$C_{\text{ext}} = \frac{24\pi^2 R^3 \varepsilon_m^{3/2}}{\lambda} \frac{\varepsilon''}{(\varepsilon' + 2\varepsilon_m)^2 + \varepsilon''^2} \quad (2.11)$$

This equation can also be obtained by purely electrostatic arguments, and a succinct derivation is given elsewhere.^[17] Note that C_{ext} scales as R^3 , while the number density decreases as R^3 for a given amount of colloidal material. Hence, the molar absorption coefficient is independent of particle size. This is borne out for particles in the range up to about 30 nm, where scattering begins to be significant. For very small particles, less than 5–10 nm in diameter, the material properties themselves change, and this results in changes to the dielectric function, $\varepsilon(\lambda)$, and hence to the colloid optical properties. A curious feature of Eq. (2.11) is that there is no absorption if $\varepsilon' = 0$ but there is also no absorption if $\varepsilon'' = \infty$. In the first case, the particle is simply non-absorbing; while in the second case, it reflects all incident radiation. Mie could explain some of the anomalous and striking colors exhibited by small metal particles, particularly those of gold or silver.^[18] In these measurements, it is assumed that the refractive index and absorption

coefficient of the dispersed particles are known. These are usually gleaned from reflection measurements on pure thin films in vacuum.^[19] The reason that metals exhibit such strong optical effects is due to the dynamic response of the electrons. The dielectric function is related to the complex refractive index, n , through $\varepsilon(\lambda)=(n + ik)^2$. For metals, the dielectric function typically takes the form:

$$\varepsilon'(\lambda) = \varepsilon(0) - \frac{\lambda^2}{\lambda_p^2} \quad (2.12a)$$

$$\varepsilon''(\lambda) = \frac{\lambda(\lambda^2 + \lambda_d^2)}{\lambda_p^2 \lambda_d} \quad (2.12b)$$

The first term in Eq. (2.12a) is the short wavelength dielectric constant, which subsumes all UV absorption bands.

$$\lambda_p = \frac{2\pi c}{\omega_p} = \sqrt{\frac{4\pi^2 c^2 m \varepsilon_0}{Ne^2}} \quad (2.13)$$

The plasma wavelength, λ_p , is characteristic for each metal, and is a function of only the electron density, N , and the effective mass of electrons, m , in the material. λ_d is the damping constant of the conduction electrons. Surface plasmon absorption due to the confined excitation of conduction electrons in small particles occurs because the dielectric function $\varepsilon(\lambda)$ can take negative values, leading to poles in the value of a_1 . The position of the surface plasmon absorption band of small gold spheres is given to a good approximation by the condition:

$$\varepsilon_1 = -2\varepsilon_m \quad (2.14)$$

Here, $\varepsilon_m = n_{\text{med}}^2$ is the dielectric function of the (non-absorbing) solvent, and ε_1 is the real part of the dielectric function of the metal at that energy or wavelength. Previous work suggested that the dielectric data obtained from reflectivity measurements on bulk metal may be in error by about 1–3%. Such small errors are inevitable from the Kramers–Kronig analysis, but the predicted surface plasmon band position may consequently be in error by up to 10 nm.^[16]

2.1.2 Optical Absorption of Metal Ellipsoids

The optical properties are heavily dependent on the morphology and size of metal particles. In 1912, Gans^[20] predicted that for very small ellipsoids, where the dipole approximation holds, the surface plasmon mode would split into two distinct modes. This is a consequence of the surface curvature, which determines classically the restoring force or depolarization field that acts on the confined conduction electron population. The researcher quantified the response as a function of the ellipsoid aspect ratio.^[20] For most nanorods, electron microscopy reveals that they are more like cylinders or spherocapped cylinders than ellipsoids. However, an analytical solution for such morphologies is not possible. Solutions have been found for the case of an infinite cylinder and for oblate and prolate ellipsoids. Ruppin has extensively studied the light scattering by finite dielectric cylinders,^[21, 22] while Fuchs has provided numerical solutions for the modes of a cube-shaped nanocrystal,^[23] and also a method for numerical solution to the general problem of modes in non-spherical particles via a surface integral technique, which appears to be an alternative to the discrete dipole approximation (DDA) approach. Numerical methods, especially the T-matrix^[24, 25] and DDA technique^[14, 26, 27] have been widely applied to small metal particles. Schatz and co-workers have recently reviewed this approach.^[12] With the development of advanced experimental techniques, Stookey and Araujo^[28] stretched glasses containing small silver spheres in the 1960s. The small particles were aligned in the molten glass to form necklaces, which exhibited red-shifted absorption spectra. Other work involved thermally evaporating silver or gold through angled masks to create small, anisotropic, 2D layers of metal on glass substrates. More recently, it has become feasible to chemically synthesize small gold rods. In explaining the optical properties of these small rods, it has been common to treat them as ellipsoids,^[29-32] which allows the Gans formula to be applied. The polarizability of an ellipsoid is given by:

$$\alpha_{x,y,z} = \frac{4\pi abc(\epsilon_{\text{Au}} - \epsilon_{\text{m}})}{3\epsilon_{\text{m}} + 3L_{x,y,z}(\epsilon_{\text{Au}} - \epsilon_{\text{m}})} \quad (2.15)$$

Here a , b and c refer to the length of the ellipse along the x , y and z axes ($a > b = c$), ϵ_{Au} the dielectric function of Au, ϵ_{m} the dielectric constant of the medium at optical

frequencies and $L_{x,y,z}$ is the depolarization factor for the respective axis, which is given by:

$$L_x = \frac{1 - e^2}{e^2} \left(-1 + \frac{1}{2e} \ln \frac{1+e}{1-e} \right) \quad (2.16)$$

$$L_{y,z} = \frac{(1 - L_x)}{2} \quad (2.17)$$

Here, e is the rod ellipticity given by $e^2 = 1 - (b/a)^2$. For a sphere $e = 0$ and $L = 1/3$. The polarizability is related directly to the extinction of light by $C_{\text{ext}} = kI(\alpha)$ (Figure 2.1).

These equations provide the stimulation for much of the subsequent experimental work on the growth and synthesis of gold and metal rods. The implication is clear. If the material growth parameters can be controlled, materials with tunable absorption spectra can be synthesized. Subsequently, there should be many applications for such materials in optics, thin films and coatings if the metals are generally photo-stable, unlike semiconductors. Oriented ellipsoids and cylinders should exhibit strong, polarization-dependent optical spectra. Moreover, the successful chemical growth of small rods and cylinders may signal the advent of systematic fabrication of nanowires and even electronic circuitry through wet-chemical processing.

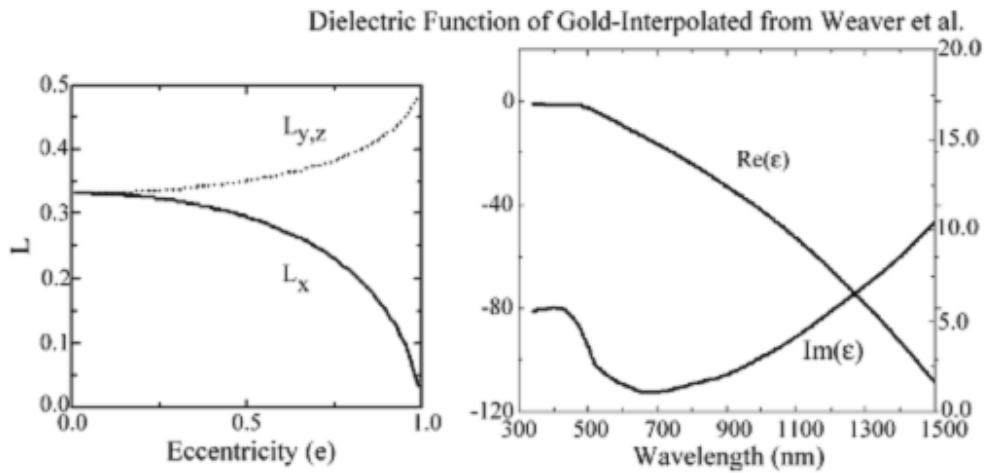


Figure 2.1 Depolarization of a prolate spheroid vs. eccentricity, e , along the major axis, x and the two equivalent minor axes, y and z (left). The real and imaginary parts of the dielectric function of bulk gold (right).^[16]

2.1.3 The Effect of Aspect Ratio

Gans' equation predicts how the plasmon mode peak position varies with aspect ratio for small ellipsoids embedded in the same medium. The easiest way to visualize this is to plot the depolarization factor L in Eq. (2.16) versus the value of the dielectric function at the peak (Figure 2.2). An observation from combining transmission electron microscopy (TEM) image of Au nanocrystals with spectral measurements is an almost linear correlation between peak position and the aspect ratios. Results from Pérez-Juste et al. [33] are shown in Figure 2.3.

Small changes in aspect ratio can result in drastic changes in transmitted colors as seen in the samples in Figure 2.4. The fact that the plasmon band appears to be drastically red-shifted from the positions predicted by the Gans model, yet still displays the linearity expected from Eqs. (2.15) and (2.16). El-Sayed and co-workers proposed [31] that the water layers around the rods were polarized and had a substantially higher refractive index than water. Yan et al. [34] pointed out that their analysis contains a mathematical flaw; yet even so it is clear that the discrepancy needs to be explained. From the micrographs shown below, one explanation is that cylindrical particles exhibit surface plasmon longitudinal (SP_{long}) bands red-shifted from those of similar sized ellipsoids.

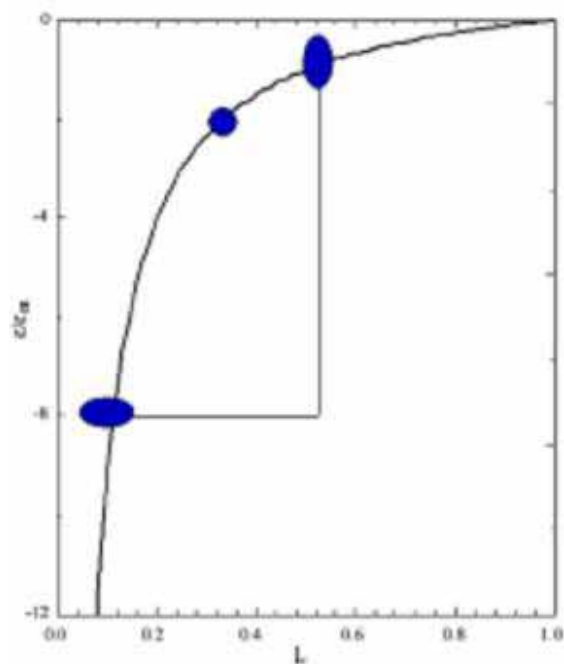


Figure 2.2 The ratio of the dielectric function of the material to the medium for different polarization factors. [33]

2.1.4. The Effect of the Refractive Index of the Solvent

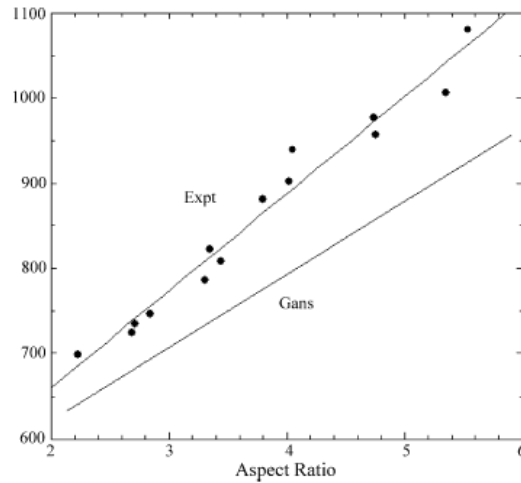


Figure 2.3 Experimental plot of the surface plasmon longitudinal band position vs. aspect ratio for pure gold rods in water. This linear correlation is fortuitous. Over large aspect ratio values, the Gans formula predicts a slow curvature. Furthermore, retardation effects and radiation damping become more prominent for larger aspect ratios. These effects are not included in the basic ellipsoid model. [16]

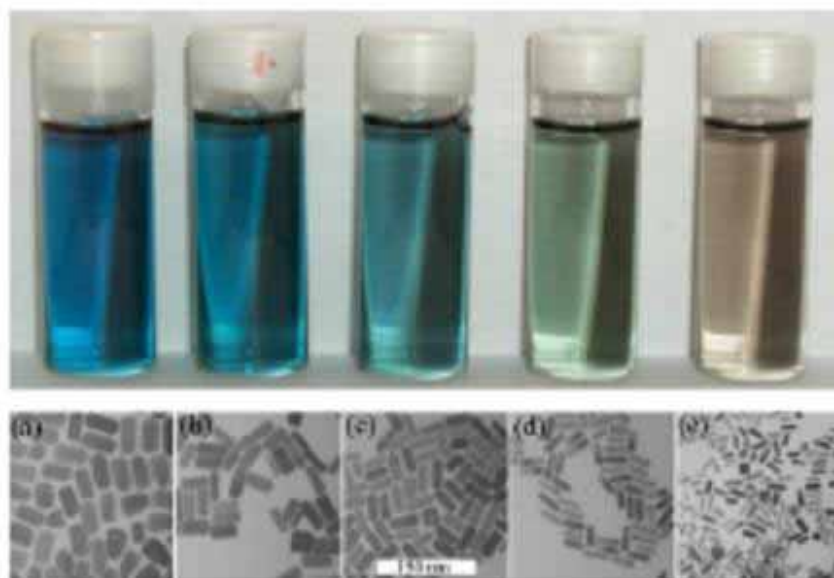


Figure 2.4 The color of gold rods and the respective micrographs. The color changes take place for very small changes in mean aspect ratio. [16]

Gold nanorods change color when embedded in different solvents of varying refractive index. Typical experimental data are shown in the left hand graph of Figure 2.5, while the right hand graph shows a plot of the peak position versus solvent refractive index. Note that the peak absorption and the peak width both increase as n increases. Calculated spectra for ellipsoids in different media are shown in Figure 2.6. As can be seen the shifts are quite dramatic. The gold nanorods are extremely sensitive to the dielectric properties of their environment. The calculations predict stronger shifts than are observed experimentally.

For a sphere, the single plasmon mode occurs at $\epsilon/\epsilon_m = -2$, corresponding to $L = 1/3$. When the degeneracy is lifted, two modes split out from this point. The transverse mode asymptotes towards $L = 1.0$, giving a peak at the wavelength where the dielectric function of the metal is zero. This is the condition for surface plasmon excitation of an infinite surface slab. For Au, this is about 510 nm in water (as compared to 520 nm for spheres) so the transverse band shifts only slightly toward short wavelengths as the rods grow. Conversely, the longitudinal mode continues to slide to more negative values of ϵ/ϵ_m , corresponding to longer wavelengths, according to Eq. (2.16).

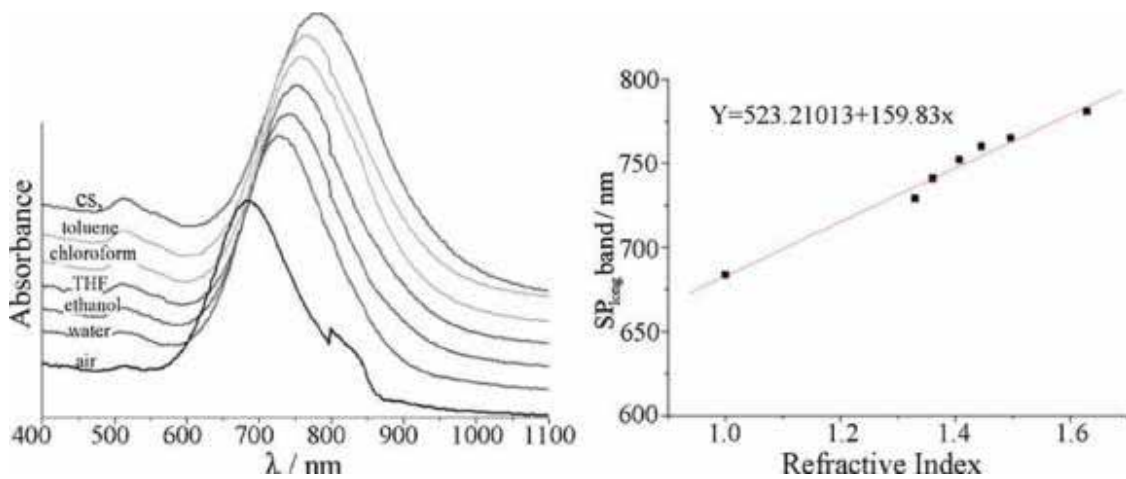


Figure 2.5 Experimental spectra of gold nanorods in different solvents (left) and change in the longitudinal plasmon band position with refractive index (right). ^[16]

To obtain $n = 1$, the particles were coated on glass. However, the effective refractive index for small particles in air supported on glass is approximately $n_{\text{eff}} = (n_{\text{air}} + n_{\text{glass}})/2 \sim$

1.25. From Eq. (2.15), the enhanced sensitivity of gold rods over gold spheres towards dielectric perturbations is readily understood.

$$\alpha_{x,y,z} = \frac{4\pi abc(\varepsilon_{Au} - \varepsilon_m)}{3\varepsilon_m + 3L_{x,y,z}(\varepsilon_{Au} - \varepsilon_m)} \quad (2.17)$$

$$3\varepsilon_m + 3L(\varepsilon_{Au} - \varepsilon_m) = 0 \quad (2.18)$$

$$\varepsilon_m + L \left(\varepsilon^0 - \frac{\lambda^2}{\lambda_p^2} - \varepsilon_m \right) = 0 \quad (2.19)$$

It follows that the peak position shifts according to:

$$\lambda^2 = \lambda_p^2 \left(\varepsilon^0 + \varepsilon_m \left(\frac{1}{L} - 1 \right) \right) \quad (2.20)$$

As the eccentricity of the rods increases, the slope of the dispersion curve increases. The longer the rod, the greater the sensitivity to refractive index effects on SP_{long} . This holds provided that the ellipsoid model remains valid. However, such long rods will necessarily absorb in the IR, so that the color effect will be less apparent to the observer.

2.1.5 The Effect of a Shell Layer

To tackle some of the key optical effects observed during synthesis and measurements of chemically synthesized metal nanorods, some simple modifications to Eqs. (2.10)–(2.16) could be considered, particularly the effect of a dielectric shell. Eq. (2.15) can be modified in the case of a small coated ellipsoid in the electrostatic limit. The polarizability is then given by the following equation:

$$\alpha^x = V \frac{((\varepsilon_2 - \varepsilon_m)[\varepsilon_2 + (\varepsilon_1 - \varepsilon_2)(L_{core}^x - fL_{shell}^x)] + f\varepsilon_2(\varepsilon_1 - \varepsilon_2))}{((\varepsilon_2 + (\varepsilon_1 - \varepsilon_2)(L_{core}^x - fL_{shell}^x))[\varepsilon_m + (\varepsilon_2 - \varepsilon_m)L_{shell}^x] + \varepsilon_2(\varepsilon_1 - \varepsilon_2))} \quad (2.21)$$

where, ε_{core} and ε_{shell} which representing ε_1 and ε_2 in Eq. 2.21 are the dielectric function of

the core and shell components of the ellipsoid, ϵ_m is the real dielectric constant of the non-absorbing medium.

L_{core} and L_{shell} are the depolarization factors for the core and shell, respectively, $V=4\pi a_{\text{shell}}b_{\text{shell}}c_{\text{shell}}/3$ is the volume of the coated particle, f is the volume fraction $a_{\text{core}}b_{\text{core}}c_{\text{core}}/a_{\text{shell}}b_{\text{shell}}c_{\text{shell}}$ occupied by the inner ellipsoid. When $\epsilon_{\text{core}} = \epsilon_{\text{shell}}$, we recover Eq. (2.15) as expected.

For a thin non-absorbing shell, it is similar to the effect of immersion in a medium with the same refractive index, and the origin of the spectral shift is similar. Because of the sensitivity of the surface plasmon resonance to both geometric and dielectric effects, particles that can be selectively deposited a coating layer have promising applications as optical sensors. The peak position changes perceptibly even for thin shells. Any shell layer with a different refractive index to the embedding medium will cause a shift in the surface plasmon transverse and longitudinal mode positions.

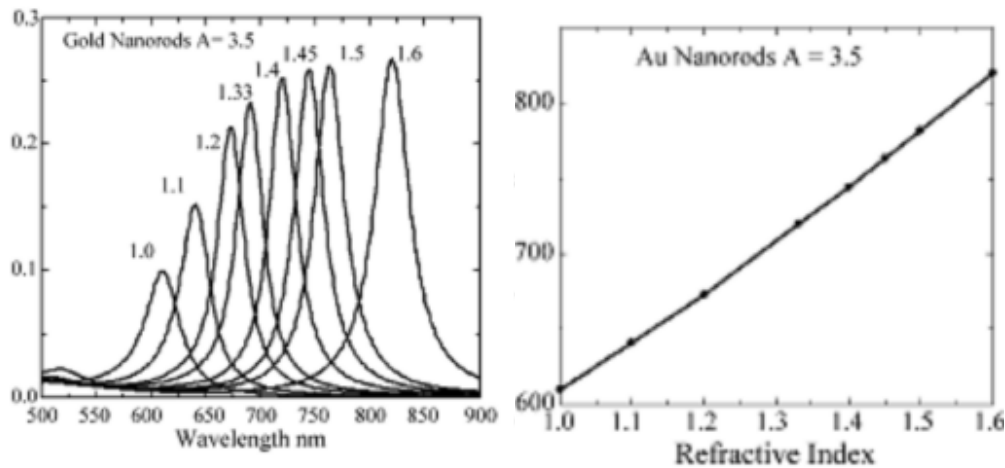


Figure 2.6 Calculated spectra for gold ellipsoids with an aspect ratio of 3.5 in different media as a function of the medium refractive index. There is a drastic red-shift with increasing solvent polarizability. The peak in extinction coefficient occurs because at longer wavelengths, there is increasing damping, i.e., a rise in the value of ϵ'' , see Figure 2.1. ^[16]

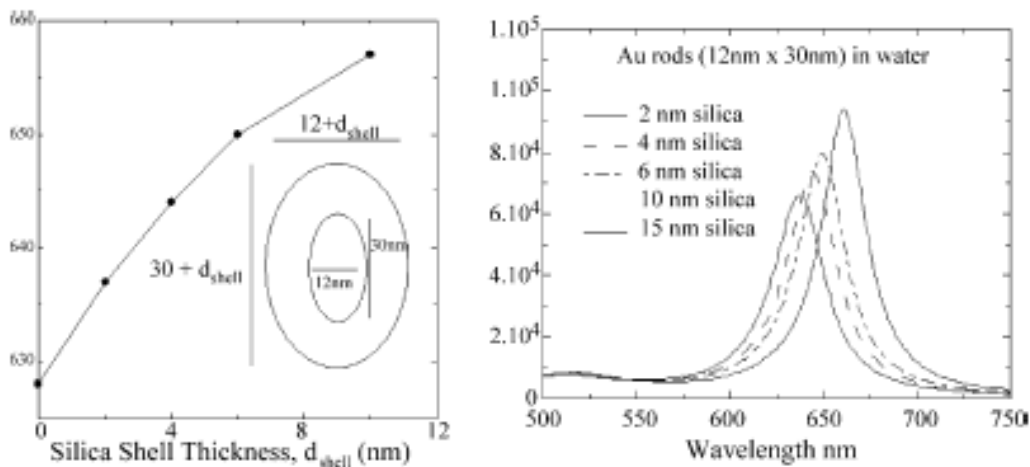


Figure 2.7 Calculated spectra for a gold rod in water. The rod has dimensions 12 nm×30 nm. The calculation shows the shift in SPL for 2, 4, 6, and 8 nm silica shells with an assumed refractive index of $n = 1.5$. [35]

For example, an antibody functionalized gold rod will respond to the presence of the corresponding antigen through a red-shift in the plasmon mode, since the antigen will have a higher refractive index than water. However, there are other reasons for synthesizing core-shell nanorods for desirable functional properties. To prevent gold rods from precipitate or coalescence, and to facilitate dispersion and orientation in polymers, glasses or non-polar solvents, silica coating is particularly useful. In Figure 2.7, we show calculated spectra for a silica-coated gold rod in water. The rod has dimensions 12 nm×30 nm. The calculation shows the shift in SPL for 2, 4, 6 and 8 nm silica shells with an assumed refractive index of $n = 1.5$.

2.1.6 The Effect of Particular Orientation

The longitudinal and transverse localized plasmon resonances of gold nanorods can be selectively excited by using light polarized with the oscillating electric field parallel and perpendicular to the long axis of the rod, respectively, because they are basically independent of each other. [36] Experimentally, this effect can only be studied if all rods are oriented in the same direction, so that they respond equally to light with the same

polarization, which can be achieved through extension in polymer films.^[37] Assuming the particles are small, the extinction coefficient of the film should be given by:

$$C_{\text{ext}} = k \text{Im}\{\alpha_{\text{L}}(1 - \cos^2(\theta)) + \alpha_{\text{T}}(\cos^2(\theta))\} \quad (2.22)$$

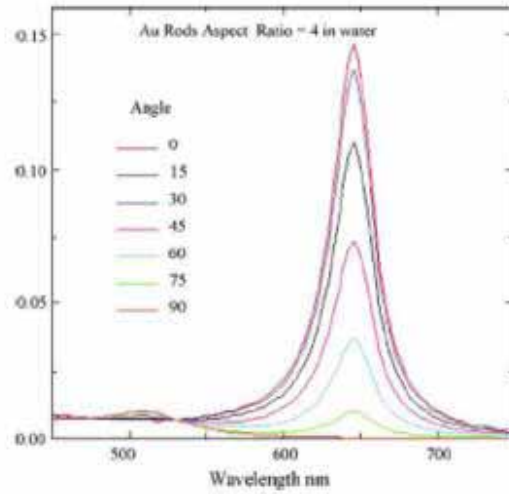


Figure 2.8 Calculated spectra of vertically oriented gold nanorods with aspect ratio of 4.0 in water. The spectra are calculated for various angles, and show that there is an isosbestic point at about 530 nm.^[16]

Typical calculated spectra for such a film as a function of the polarization of the incident light are shown in Figure 2.8. When the incident beam is polarized parallel to the long axis of the rods (0°), only the longitudinal surface plasmon is excited, and thus only the band at 645 nm is observed. Conversely, for light polarized perpendicular to the long axis (90°), the SP_{long} band is completely removed and only the transverse mode is excited. For intermediate angles, contributions of both modes exist, as defined by Eq. (2.22), which is confirmed by the presence of an isosbestic point at about 530 nm.

To realize the orientation of particles, many methods have been developed to self-assemble nanoparticles. For example, suspended gold nanoplates that was prepared via electrochemical method (Figure 2.9) by using some amount of silver ions as catalyst.^[36]

A gold metal plate was used as the anode and platinum plate as the cathode in the electrochemical cell. By introducing current and heat at certain time then the nanoplates was formed.

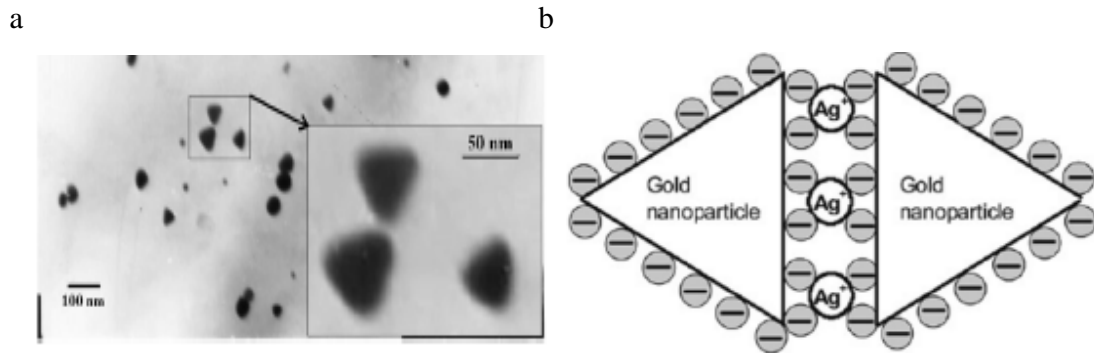


Figure 2.9 (a) TEM image of gold triangular nanoplates; (b) Self-assembly model of rhombic nanostructures. ^[36]

Furthermore, it was found that when this sample was aged at room temperature for 3 days, the gold nanoplates self-organized into rhombic nanostructures as can be seen from Figure 2.10. ^[36] Gold colloidal particles that consist of elemental gold core were surrounded by double charge negative ions, which prevent aggregation in solution to exist.

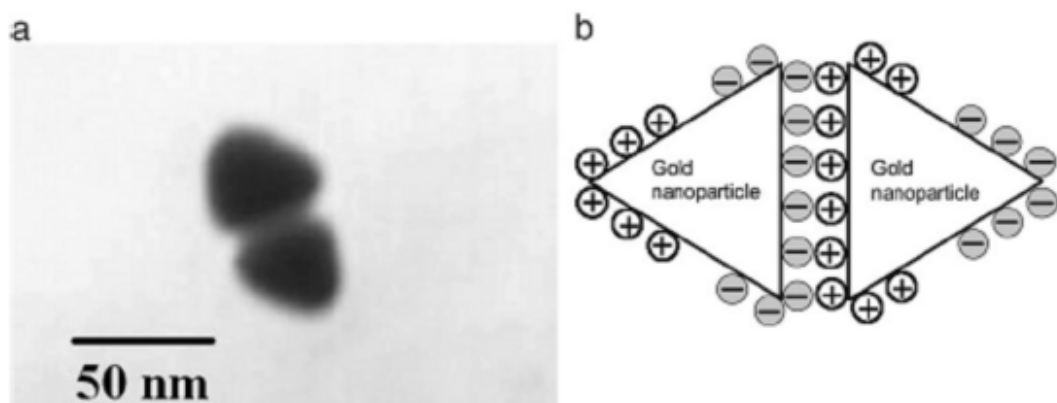


Figure 2.10 (a) TEM image of pairs of gold triangular nanoplates and (b) corresponding dipole assembly model. ^[36]

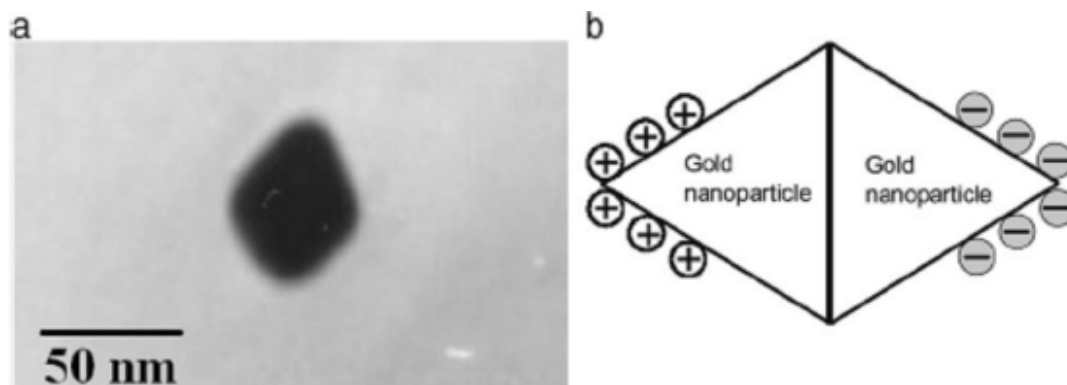


Figure 2.11 (a) TEM image of rhombic nanostructure and (b) corresponding dipole assembly model. ^[36]

However, this double layer charge produced ζ potential that can be neutralized by either binding of a cation or lowering the pH and decreases the ζ potential. This, however, will lead the nanoparticles to aggregation. And small surface charge left on the nanoparticles may cause the nanoparticles repelled to each other and enhanced the formation of chain-like aggregation instead of cluster-shape aggregation. For example, silver ions that were added, not only behaved as a catalyst but also to neutralize the ζ potential and create the local cationic regions. Then due to the electrostatic interaction, two individual Au triangular nanoplates will self-assembly into a rhombic nanostructure. ^[36]

Another factor that enhanced this self-organization is the strong dipole-dipole interaction, which was believed to be the driving force. When two particles approach each other, columbic repelling force would take place and allowed the adsorbed charges to evenly disperse on the surface of the particles. This would lead Au nanoplates assembling to be a dimer or the rhombic nanostructure (Figure 2.11). ^[36]

2.1.7 Nonradiative Relaxation in Metal Nanostructured Systems

2.1.7.1 Nonradiative Relaxation of Gold

To understand the fundamentals, various spectroscopy techniques including time-resolved transmission, reflectivity, ^[38-51] and two-photon photoemission ^[52-57] have been used to study the interaction between the electrons and the lattice vibrations (phonons) in bulk metallic materials. The electrons of the metal can be selectively excited, and the

electron-phonon coupling can be studied in real time, with the advancement of ultra-short laser pulses that are shorter than the electron-phonon energy relaxation time. ^[40, 41] Electron- electron interactions are strong enough to thermalize the electron gas within the duration of the laser pulse excitation because of the high electron density in metals.

It is the high density of the charge carriers in the conduction band that results in fast interband relaxation. If an Auger-type recombination mechanism process takes place for the interband relaxation, then after the excitation pulse, highly excited electrons are present within the conduction. These electrons have an average excess energy above the Fermi level, which is equal to the exciting photon energy, as the holes in the *d* band have already been filled by the initial electron-electron scattering. ^[38, 39] In the case of gold thin films, a typical electron-phonon relaxation process occurs within a few picoseconds. ^[38-57] The influence of size on the electron-phonon coupling can be directly analyzed by measuring the transient optical response of metal nanoparticles. The reduction in the size and dimensionality of the material could introduce new boundaries at the surface. Enhanced electron-surface scattering ^[58, 59] could also be important for the energy relaxation of hot electrons. The relaxation dynamics in these zero-dimensional dots could be further altered by the reduction in the density of electron and phonon states. The bulk band structure of the nanoparticles is well-developed in the size range of 10-100 nm gold nanoparticles. ^[39, 60] Compared with the thermal energy, the average energy spacing between adjacent energy levels within the conduction band is small. Thus, quantum size effects in the relaxation dynamics are expected to occur only in very small gold clusters, which lack intense plasmon absorptions. The presence of a well-developed plasmon band can, however, be very advantageous in following the optical response of excited metal nanoparticles. ^[61-73] For a 20-nm gold nanoparticle with ~200 000 atoms, absorption results in a bleach at the plasmon absorption band maximum with two positive absorption features at higher and lower energies. The rate of the bleach recovery directly monitors the rate of the electron-electron, electron-phonon, and phonon-phonon dynamics. ^[38, 39]

2.1.7.2 Theoretical Modeling of Optical Response

To be more quantitative, a theoretical modeling was proposed (eq. 2.23). The changes in the real ϵ_1 and imaginary ϵ_2 parts of the complex dielectric function induce the broadening of the plasmon band. [43, 46, 47, 61, 62, 70] For continuous-wave thermo-modulation experiments, the changes in ϵ_1 and ϵ_2 are related to the changes in the electron distribution function. [74, 75] In the constant-matrix approximation, the change in ϵ_2 is given by the equation. [47]

$$\Delta\epsilon_2 \propto \frac{1}{(h\nu)^2} \int D(E, h\nu) \Delta\rho \, dE \quad (2.23)$$

where $D(E, h\nu)$ is the joint density of states of the final state with respect to the energy E [45] and $\Delta\rho$ denotes the change in the electron distribution, f .

$$\Delta\epsilon_1(h\nu) = \frac{2}{\pi} P \left(\int \frac{h\nu' \Delta\epsilon_2(h\nu')}{(h\nu')^2 - (h\nu)^2} d(h\nu') \right) \quad (2.24)$$

$$\frac{\Delta T}{T} = \frac{\delta(\ln T)}{\delta\epsilon_1} \Delta\epsilon_1 + \frac{\delta(\ln T)}{\delta\epsilon_2} \Delta\epsilon_2 \quad (2.25)$$

The change ($\Delta\rho$) in the electron distribution for a thermalized electron gas is calculated from the difference between the two Fermi electron distributions at room temperature and at a higher temperature after laser excitation. A given change in $\Delta\rho$ in the electron distribution corresponds to a $\Delta\epsilon_2$. The change $\Delta\epsilon_1$ in the real part of the dielectric constant is then computed from $\Delta\epsilon_2$ using the Kramers-Kronig relationship. [76] The coefficients of proportionality can be calculated using the theoretical expression for the plasmon band absorption. This model has been used successfully in the description of the optical response of metal nanoparticles excited by an ultrashort laser pulse (Eq. 2.24 and 2.25). [38, 39, 61, 62, 70]

2.1.7.3 Electron-Electron Thermalization in Gold Nanoparticles

The thermal response of an excited sample, expressed as temperature changes, can be obtained from the optical changes induced by the pump pulse through a pump-probe laser spectroscopy technique (transient absorption, transmission, or reflectivity); Fermi-Dirac statistics describe the electron distribution within the conduction band of the metal after a

rapid internal electron relaxation.^[76] Each Fermi electron distribution is associated with an electronic temperature. Therefore, the electronic temperature can be used to follow the energy relaxation of the electron gas into the lattice motion.^[38, 39]

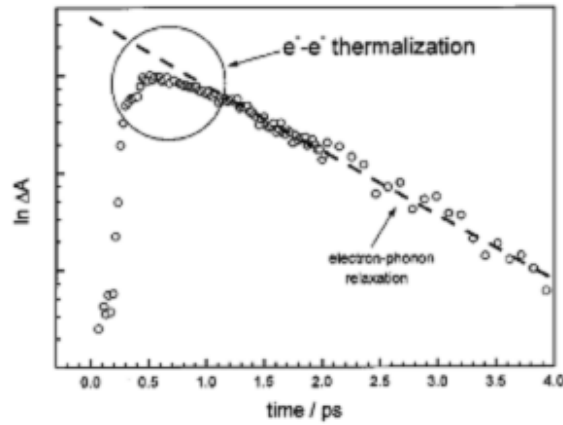


Figure 2.12 Electron-electron thermalization in spherical gold nanoparticles. The plasmon bleach recovery of 22-nm gold nanoparticles probed at 530 nm is plotted against a logarithmic scale.^[39]

Figure 2.12 is the kinetic bleach recovery trace recorded for 22 nm gold nanoparticles at 530 nm after excitation with 800 nm femtosecond laser pulses.^[39, 70] A single-exponential decay should be obtained due to electron-phonon scattering if the long-time component of phonon-phonon interactions is neglected. However, deviations at early times are clearly visible due to the non-thermal electron distribution,^[48] The bleaching of the plasmon band is less intense for a non-thermalized than for a thermalized electron distribution, which is consistent with the calculation of the transient absorption spectrum.^[39, 47, 70] The electron thermalization time is on the scale of <500 fs^[38, 39, 70] and is much longer than a scattering event involving only two electrons, which is on the order of 10 fs according to the Fermi-liquid theory.^[77] It requires all of the electrons to scatter with each other to reach a Fermi distribution. Due to the processes of electron-electron, electron-phonon, and phonon-phonon scattering are not really sequential but overlapping processes, the effect of these processes on the transient absorption spectra is rather small (compared with theoretical results) and only detectable at low pump powers.^[70] Before an equilibrium, Fermi electron distribution can be fully established via electron-electron scattering, electron-phonon coupling.^[38, 39, 70]

2.1.7.4 Electron-Phonon Relaxation in Gold Nanoparticles

Figure 2.13 shows the steady ground-state absorption (top half with positive absorption) and transient absorption spectra (bottom half with negative absorption, thus bleach) of 15 nm gold particles at different delay times after the excitation pulse of 400 nm. [38] Compared with the ground-state absorption, a bleach and two positive absorptions in the transient spectrum (difference spectrum) is observed due to a broader but less intense plasmon absorption at a higher electronic temperature after laser excitation.

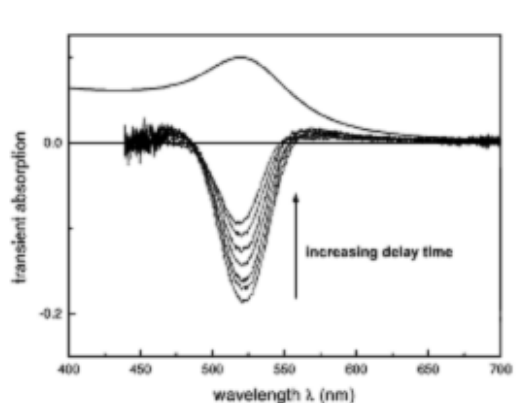


Figure 2.13 Steady-state absorption and transient absorption spectra of 15-nm gold nanoparticles after excitation with 400-nm laser light. The series of spectra corresponds to different delay times between the pump and probe pulses. [38]

The plasmon band bleaches at its maximum, which corresponds to a higher transmission of light of the excited solution. Two weaker absorption bands are also visible at lower and higher energies than the plasmon band maximum. [61, 63-65, 70, 71] This could be attributed to a broadening of the surface plasmon resonance at higher electronic temperatures. The optical response is independent of the excitation wavelength. [38, 39, 70] At 400 nm or shorter wavelengths than the plasmon absorption, interband transitions from the *d* band to above the Fermi level are excited. Excitation at the plasmon resonance causes the oscillation of the conduction electrons and the collective excitation of all the conduction electrons. This could be regarded as intraband transitions, which are also excited to the red of the plasmon band. All of these excitation processes result in heating of the electron gas. [38, 39, 70] After the thermal equilibration is established, the laser-

induced optical changes decay via electron-phonon scattering between the electrons and the lattice.^[38, 39, 62, 64, 70, 71] The absorbed laser energy is then released to the surrounding medium by phonon-phonon interactions.^[62, 64, 71] The electron-phonon and phonon-phonon relaxation times can be obtained by measuring the bleach recovery as a function of time as shown in Figure 2.14.

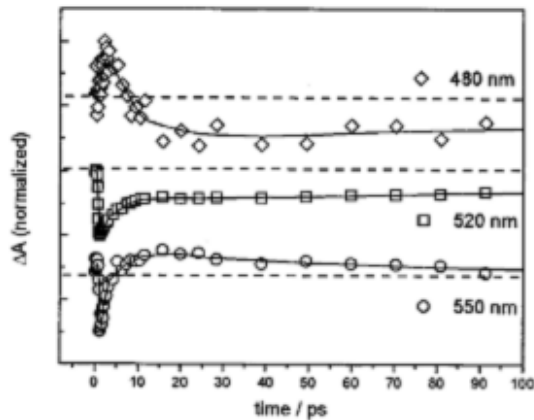


Figure 2.14 Temporal evolution of the plasmon bleach spectra at certain wavelengths: (\diamond) 480 nm; (\square) 520 nm; (\circ) 550 nm.^[39]

The transient signal is most sensitive at the wavelength of 520 nm, coinciding with the plasmon band bleach maximum. The plasmon bleach recovery can be fitted to a biexponential decay function with relaxation times of about 3.4 and 100 ps, corresponding to the electron-phonon interactions and the energy relaxation of the hot lattice via phonon-phonon interactions to the surrounding medium, respectively.^[38, 39, 71] At 480 nm, the signal first shows absorption and then bleaches gradually, which is explained by a red shift of the plasmon resonance because of a volume expansion of the hot particles and, hence, a lower electron density and lower plasmon frequency.^[62] While at 550 nm, the transient absorption signal changes from bleach into an absorption at a comparable time delay of 10 ps, resulting from a red shift and the narrowing of the plasmon bleach.^[38, 39, 70] A 5-20 ps periodic oscillation of the transient absorption signal (Figure 2.15) is found at a longer wavelength than the plasmon band maximum.^[38, 39, 68, 70] These oscillations are caused by the low frequency acoustic breathing modes of the hot nanoparticles, which are excited by the rapid heating of the particle lattice after laser excitation.^[67, 68, 72, 78] Because of the excitation of these modes, the volume of the

nanoparticles periodically increases and decreases, resulting in a shift in the plasmon band maximum as the free-electron density changes with the volume. Since a volume expansion causes a drop in the free-electron density and a red shift of the plasmon, the volume contraction has the opposite effect. The frequencies of the acoustic modes are inversely proportional to the nanoparticle radius. ^[67, 68, 72, 78]

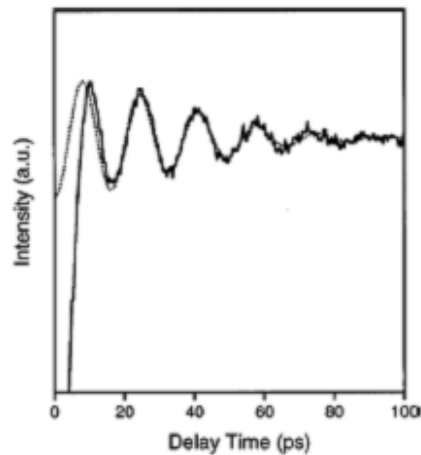


Figure 2.15 Transient absorption data obtained for 60 nm diameter Au particles (solid line) and signal calculated with a distribution of cosine functions with frequencies and weights determined by the measured size distribution of the sample (dashed line). ^[68]

Physically, the transient behavior of the plasmon band broadening is also associated with a faster dephasing time (T_2) of the coherent plasmon oscillation. ^[63-65] For gold nanoparticles embedded in a sol-gel matrix, an increase by 120 meV in the plasmon bandwidth was found, and for a hot electron distribution at 4000 K, an average electron-electron scattering rate was calculated to be $(10 \text{ fs})^{-1}$ by Perner et al. ^[64] This is because higher temperatures will lead the occupation of higher electronic states to an increased electron scattering rate ^[77] and thus to an increased damping of the plasmon oscillation. Figure 2.16 shows the decay of the transient plasmon band broadening following the same kinetics as the decay of the bleach intensity for 15 nm gold nanoparticles. This was concluded from transient absorption spectra obtained with excitation at 400 nm with 100 fs laser pulses at different delay times. The line width decays with a lifetime of 4.8 ps, whereas the plasmon bleach intensity at its maximum (2.38 eV) decays with a lifetime of 4.3 ps.

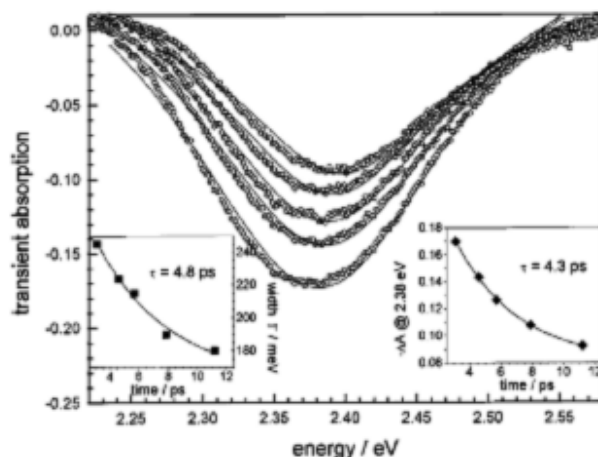


Figure 2.16 Transient absorption spectra of 15-nm gold nanoparticles after excitation at 400 nm with 100-fs laser pulses recorded at different delay times. The left inset shows the decrease in the bleach line width with increasing delay time. The line width was obtained by fitting a Lorentzian function (s) to the experimental spectra (O). The right inset illustrates the decay of the transient bleach signal monitored at 2.38 eV. ^[38]

2.1.7.5 Electron-Phonon Relaxation Rate

Electron-phonon relaxation rate is dependent on the shape and size of metal nanoparticles. Figure 2.17 shows the transient absorption and steady-state absorption spectra of gold nanorods with a mean aspect ratio of 3.8. The spectra were recorded at a delay time of 6 ps after excitation with 100 fs laser pulses having a center wavelength of 400 nm. Both the longitudinal and transverse surface plasmon bands are bleached due to a hot electron gas. ^[69] The bleach of these two bands and the positive absorption around 600 nm are consistent with a broadening of these bands. The magnitude of the bleach is less pronounced for the longitudinal plasmon band than for the transverse plasmon band, which is evaluated by comparing the intensity ratio of the two bands in the transient absorption spectrum with that for the steady-state spectrum. ^[67, 68, 72, 78]

The increased electron-surface scattering is thought to be responsible for the plasmon band broadening in the intrinsic size region. Femtosecond determines whether electron-surface collisions are mainly inelastic and contribute effectively to energy relaxation. For gold and silver nanoparticles with a mean free path of ~40-50 nm, ^[76] the measured

electron-phonon relaxation time should increase with decreasing particle radius if electron-surface scattering becomes an important relaxation pathway for small particles.

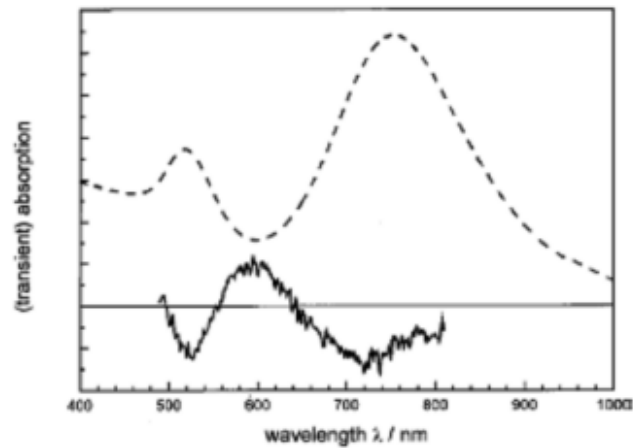


Figure 2.17 Optical response of gold nanorods after excitation with a femtosecond laser pulse. Transient absorption (s) and steady-state absorption spectrum (- - -) of gold nanorods with a mean aspect ratio of 3.8 are shown. Both spectra are scaled to arbitrary units. The transient absorption spectrum was recorded at a delay time of 6 ps after excitation with 100-fs laser pulses having a center wavelength of 400 nm. ^[38]

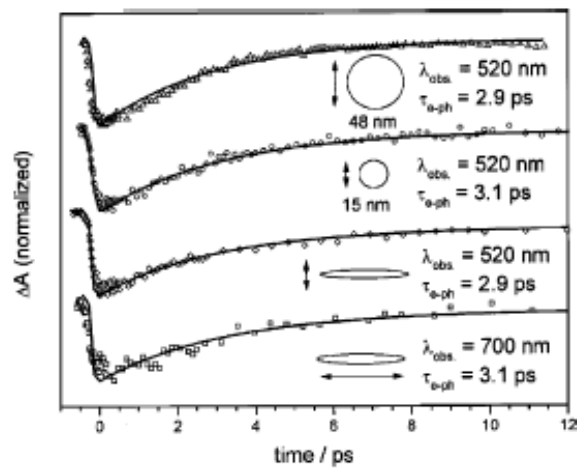


Figure 2.18 Size and shape dependence of the electron-phonon relaxation time. Plasmon bleach recovery was measured for 48- and 15-nm gold nanoparticles and for the transverse and longitudinal modes of gold nanorods with an average aspect ratio of 3.8 (from top to bottom). ^[79]

Figure 2.18 shows that the plasmon bleach recovery measured for 48 and 15 nm gold nanoparticles in comparison to the bleach recovery of the transverse and longitudinal modes of gold nanorods with an average aspect ratio of 3.8 (top to bottom). The laser pump power and optical densities of the samples at the excitation wavelength were adjusted to induce comparable initial electron temperatures by the exciting femtosecond laser pulse to ensure the measured relaxation times can be directly compared with each other. For 15 and 48 nm gold nanoparticles, the slight difference in the electron-phonon relaxation dynamics can be observed,^[38] and the relaxation dynamics appear to be independent of the particle shape and the specific plasmon band excitation modes (transverse or longitudinal mode).^[38, 69]

The electron-surface scattering as a dominant energy relaxation pathway was excluded from these experiments and other studies and on other metal nanoparticles such as silver nanoparticles.^[61, 68, 80] In other experiments, however, contradicting results were also observed.^[72, 81-84] For example, a size dependence was found by Smith et al.^[81] in the comparative study of 15 nm gold nanoparticles with small Au₁₃ and Au₅₅ clusters.

The electron-phonon coupling decreases and the electron-surface scattering increase with the nanoparticle size decreasing. In addition, enhanced electron-surface scattering was found for tin, gallium, and silver nanoparticles as the size of the particles decreased from >10 to <1 nm.^[72, 81-84] The difference in the size dependence of the electron-phonon relaxation in different metallic nanoparticles was reported by Hodak et al.^[85] who explained the contribution of the electron-surface coupling constant to the total (bulk) coupling constant. When gold nanoparticles are as small as 2.6 nm, the excitation of capillary and acoustic surface modes by the scattering of the electrons with the particle surface is calculated to account for <10% of the electron energy loss. The ratio of the electron density to the metal density in a specific metal determines the relative magnitude of the electron-surface coupling constant compared with the total electron-phonon coupling constant. Due to gold nanoparticles consisting of heavy atoms, the excitation of surface vibrations is suppressed as the electrons scatter rather elastically. While in nanoparticles made of lighter atoms, a size dependent energy relaxation becomes possible

via electron-surface interactions with more valence electrons contributing to the conduction band and smaller atomic mass. [72, 81-84]

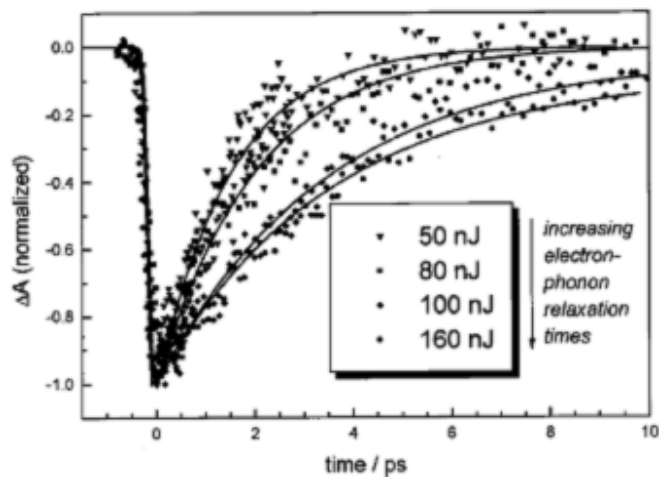


Figure 2.19 Pump power dependence of the electron-phonon relaxation time in gold nanoparticles. The Plasmon bleach recovery of 15-nm gold nanoparticles is probed at 520 nm after excitation at 400 nm with laser pulses of various energies. [72, 81-84]

Moreover, the electron-phonon relaxation times are pump power dependent, [61, 62, 66, 70] as demonstrated in Figure 2.19. [72, 81-84] The measured lifetimes increase from 1.5 to 3.6 ps as the pump power increases from 50 to 160 nJ. With increasing pump power and, hence, increasing electron temperature, the electron-phonon relaxation time increases. [61, 62, 66, 70] However, the effective rate constant [$g/C_e(T_e)$] of the thermal relaxation of the electron gas (dC_e/dT_e) is temperature dependent, because the electronic heat capacity depends on the electron temperature ($C_e \propto T_e$). [76] From a plot of the measured electron-phonon relaxation times versus power, the electron-phonon coupling constant can be obtained, [62, 66] which compares well with the value measured for bulk gold films.

2.1.7.6 Other properties of Gold nanoparticles

Melting point. Various materials ranging from metals to semiconductors to insulators, a decrease in solid to liquid transition temperature has been observed with size decreasing. [86-89] This is because the surface atoms tend to be coordinatively unsaturated at such a size scale. A large energy is associated with this surface. The key to understanding this

melting point depression is the fact that the surface energy is always lower in the liquid phase compared to the solid phase.

In the dynamic fluid phase, surface atoms move to minimize surface area and unfavorable surface interactions. While in the solid phase, rigid bonding geometries cause stepped surfaces with high-energy edge and corner atoms. Melting can reduce the total surface energy. This stabilizes the liquid phase over the solid phase. The smaller the nanocrystal, the larger the contribution made by the surface energy to the overall energy of the system and thus, the more dramatic the melting temperature depression.

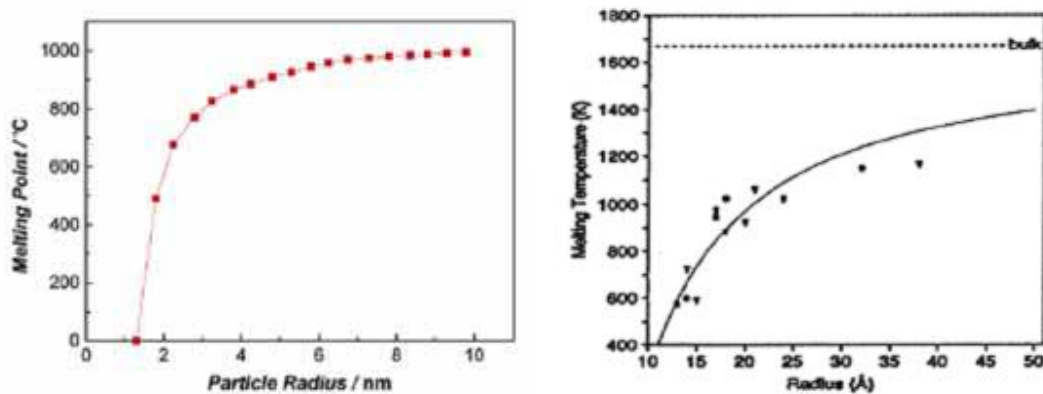


Figure 2.20 Relationship between the melting points and the sizes of gold (left) ^[90] and CdS nanoparticles (right). ^[91]

As melting is believed to start on the surface of a nanocrystal, this surface stabilization is an intrinsic and immediate part of the melting process. ^[92, 93] Figure 2.20 shows the relationship between particle size and melting point of metallic gold and semiconductor CdS nanoparticles. Clearly, the melting point decreases as the size of the particles decreases, and there is a dramatic decrease in the melting points for particles that are smaller than 3-4 nm. ^[90, 91]

Conductivity and Coulomb Blockade of Metals. Electrical conductivity of bulk metals is based on their band structures. The mobility of electrons is described by (Eq. 2.26):

$$\mu = \frac{e\lambda}{4\pi\epsilon_0 m_e V_F} \tag{2.26}$$

where λ is the mean free path of the electrons between two collisions, m_e is the effective mass of the electron in the lattice, V_F is the speed of the electrons (Fermi speed), and ϵ_0 is the dielectric constant of vacuum. The expression λ/V_F can be interpreted as the mean time, τ , between two collisions of electrons. For example, in copper, V_F is $\sim 1.6 \times 10^6 \text{ ms}^{-1}$ and λ is $\sim 4.3 \times 10^{-8} \text{ m}$ (43 nm), and as a result, τ is equal to $2.7 \times 10^{-14} \text{ s}$ (270 fs). In any metal, there are two scattering mechanisms: one is caused by lattice defects (foreign atoms, vacancies, interstitial positions, and grain boundaries) and the other is caused by phonons (thermal lattice vibrations).

The collective motion of electrons in a bulk metal obeys Ohm's law $U = RI$, where U is the applied voltage, R is the resistance of the material, and I is the current.^[90] However, as the electron band becomes discrete energy levels, the above Ohm's law is no longer valid. If an electron is transferred to the particle, its Coulomb energy (E_C) increases by $E_C = e^2/(2C)$, where C is the capacitance of the particle. Thermal motion of the atoms in the particle can initiate a change in the charge and the Coulomb energy so that further electrons may tunnel uncontrolled. To produce single electron tunneling processes, the thermal energy of the particle must be much smaller than the Coulomb energy, $kT \leq e^2/(2C)$, to keep the energy on the particle. With an additional charge, a voltage $U = e/C$ is produced, leading to a tunneling current $I = U/R_T = e/(R_T C)$, where R_T is the tunnel resistance. The resulting additional charge has a mean lifetime of $\tau = R_T C$. The related Heisenberg uncertainty of energy, $\delta E = h/\tau = h/(R_T C)$, leads to unexpected tunneling if it exceeds the Coulomb energy. The Heisenberg fluctuation energy is expressed as $E = h/R_{QH} C$, where R_{QH} is the quantum Hall resistance. Thus, a second condition for single-electron tunneling is $R_{QH} \ll R_T$. The quantum resistance can also be elucidated from classical transport as follows: quantum $\rightarrow \delta e \delta t \sim h \rightarrow e^2/RC \times RC \sim h \rightarrow R \sim 2h/e^2$, where such lower R means classical. The current-voltage characteristic for an ideal quantum dot shows no current up to $U_{\text{Coulomb}} = e/C$. If this value is reached, an electron can be transferred. Following this, an electron tunneling process occurs if the Coulomb energy of the quantum dot is compensated by an external voltage of $U = \pm ne/(2C)$.

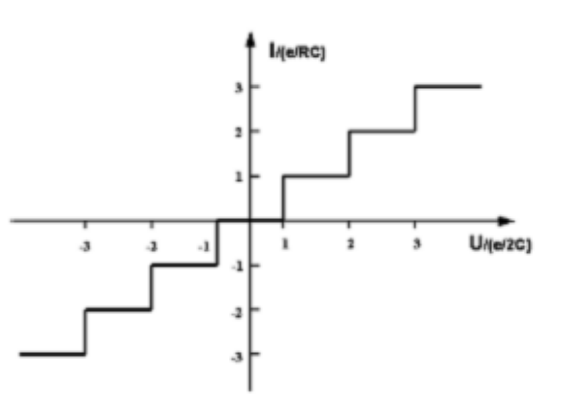


Figure 2.21 I - U characteristic of ideal single electron transport, where Coulomb blockade is shown as the step function. ^[16]

An idealized “staircase”, resulting from the repeated tunneling of single electrons, is shown in Figure 2.21. The step height ΔI corresponds to $e/(RC)$, and the width ΔU corresponds to $e/(2C)$. As the size of semiconductors and metals approaches nanometer length scales, the finite size of the materials also leads to unique electronic properties. To add a single charge to a metal nanocrystal costs energy because a charge carrier is no longer solvated in an effectively infinite medium. For a nanocrystal surrounded by a medium of dielectric constant, ϵ , the capacitance of the nanoparticle, depends on its size as $C(r) = 4\pi\epsilon r\epsilon_0$ and the energy required to add a single e charge is given by the charging energy $E_C = e^2/2C(r)$. Tunneling of single charges onto metal or semiconductor nanoparticles can be seen at temperatures $k_{BT} < E_C$ in the I - V characteristics from devices containing single nanoparticles ^[94, 95] or from STM measurements of NCs on conductive surfaces. ^[96, 97]

Figure 2.22 shows one approach to measure the Coulomb blockade. ^[94] First, metallic lead with a spacing of a few nanometers is fabricated using electron beam lithography and shadow evaporation. Then, an organic monolayer is used to bind nanocrystals to the leads and serve as a tunnel barrier. When a nanocrystal bridges the gap between the leads, it can then be electrically investigated. Figure 2.23 shows the measured current (I) as a function of the source-drain bias, V_{sd} , for a 5.8 nm Au nanoparticle system at 77 K. A

Coulomb staircase is observed due to incremental charging of the dot by single electrons with increasing V_{sd} . The period of these steps, ΔV_{sd} , is 200 mV.

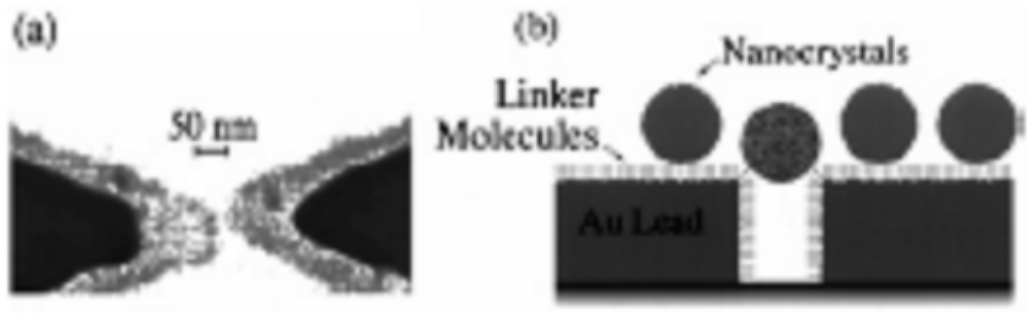


Figure 2.22 (a) Field emission scanning electron micrograph of a lead structure before the nanocrystals are introduced. The light gray region is formed by the angle evaporation and is 10 nm thick. The darker region is from normal angle evaporation and is 70 nm thick. (b) Schematic cross section of nanocrystals bound via a bifunctional linker molecule to the leads. Transport between the leads occurs through the mottled nanocrystal bridging the gap. ^[94]

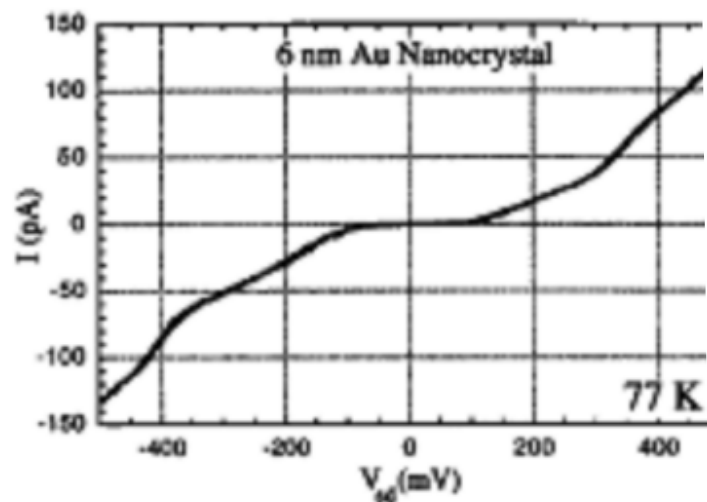


Figure 2.23 I - V characteristic of a 5.8-nm diameter Au nanocrystal measured at 77 K. Several Coulomb steps of period $\Delta V_{sd} = 200$ mV can be seen. ^[94]

2.2 Synthesis method

This section will demonstrate different methods for the synthesis of metal nanoparticles, including physical methods and chemical methods as below.

2.2.1 Irradiation Methods

2.2.1.1 Sonochemistry Method

Within the pores of silica, the synthesis of Au/Pd bimetallic particles can be achieved through a sonochemistry technique as shown in Figure 2.24. Moreover, controlling the Au nanoparticles size by using solutions radiolysis can be taken into account. This will also involve in the mechanism of Au nanoparticles formation upon γ -irradiation. ^[3]

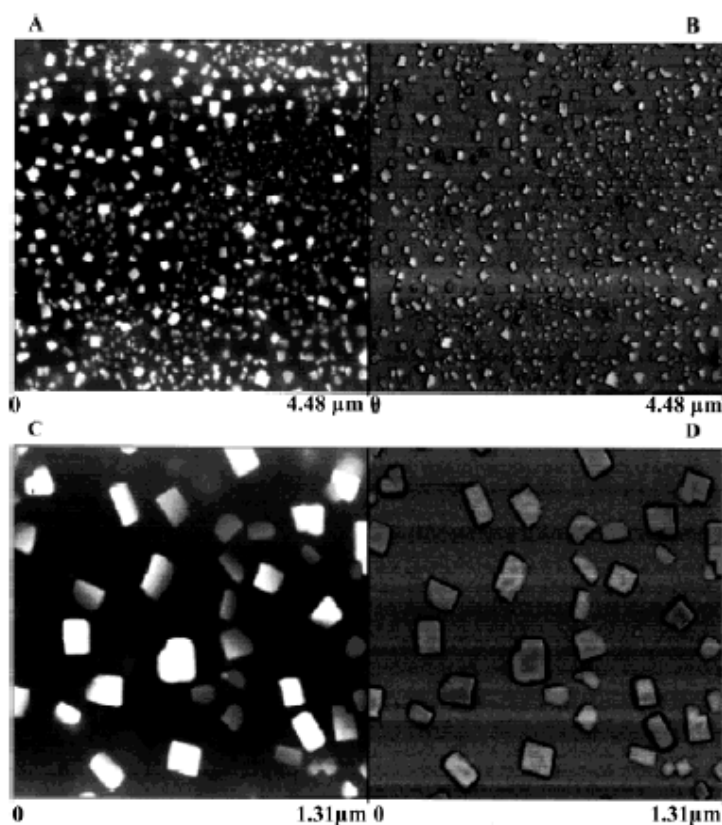


Figure 2.24 Tapping-mode AFM images of the species formed in a solution irradiated with γ rays (1.5 kGy) and then deposited on highly ordered pyrolytic graphite (HOPG) 30 days after the irradiation and dried under a mild N_2 stream for visualization. The solution contains 10^{-3} mol.L⁻¹ AuIII and poly(vinyl alcohol) but no alcohol. (A) Height-mode (z range 80.0 nm) image and (B) phase (z range 42.2°) image, run simultaneously on the

same area of the sample. (C, D) Close-up images showing the same area as in (A) and (B), respectively. [3]

2.2.1.2 Thermolysis Method

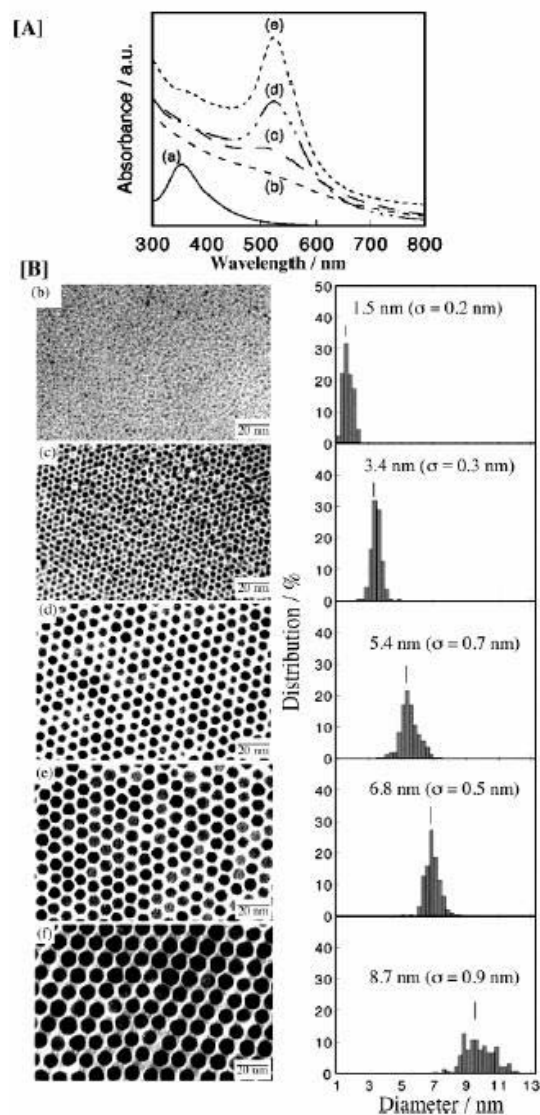


Figure 2.25 UV-vis spectra (A) and TEM images and size distributions (B). [3]

Through decomposition of $[\text{AuCl}(\text{PPh}_3)]$ Au nanoparticles can be produced upon reduction in a monolayer at the gas/liquid interface. Alkyl-groups-passivated Au nanoparticles of 26 nm can be prepared by using the thermolysis technique of $[\text{C}_{14}\text{H}_{29}\text{-Me}_3\text{N}][\text{Au}(\text{SC}_{12}\text{H}_{25})_2]$ at 180° for 5 h under N_2 . Basically thermolysis technique allows gold nanoparticles to grow bigger without removing the phase-transfer reagent. Upon heating, the Au nanoparticles formed 2D superlattice with hexagonal packing as can be seen from this figure on left hand side. Figure 2.25 A shows the UV-spectra of different samples and B the TEM images of dodecanethiol-AuNPs (b) as prepared and after heat treatment at (c) 150, (d) 190, and (e) 230 $^\circ\text{C}$; and (f) octadecanethiol-AuNPs heat-treated at 250 $^\circ\text{C}$, along with the corresponding size distribution. [3]

2.2.1.3 Laser Photolysis Method

This technique was developed to produce Au nanoparticles in block copolymer micelles, called laser ablation. This method has been used under many different conditions in

which the laser induced may control the size of the nanoparticles. Daniel and Astruc,^[3] found the evolution of thiol-stabilized Au nanoparticles that has been induced by and monitored upon heating. They found the spheroid diameter was reduced to almost 70% of the original size because of the irreversible “coagulative” transition as the effect of fusion among the nanocolloids in spheroids.^[3]

2.2.2 Chemical Synthesis

The chemical synthesis of one-dimensional nanostructures of gold and silver via surfactant-directed routes has been widely studied. A precursor such as HAuCl_4 or AgNO_3 can be reduced to atomic species by chemical, electrochemical or photochemical means in the presence of surfactants at different concentrations. The aspect ratio i.e., the ratio of length to width of resultant nanostructures can be readily controlled over a wide range by finely adjusting experimental parameters including temperature, solvent composition and surfactants. Several chemical synthesis methods are summarized in this section.^[16]

2.2.2.1 Solvothermal Method



Figure 2.26 Thin films of FeCo, CdSe, CdS, Co and Ag formed on glass microslides prepared under solvothermal conditions.^[98]

This technique assists in producing uniform nanoparticles thin films of very large area. The basic idea of this method is held at high temperature, and then pressure developed

during reactions will enhance the formation of coatings over large areas and on curved surfaces. Therefore by adjusting the pressure and the temperature of the reactor vessel, the diameter and the thickness of the film and coating can be controlled. This picture (Figure 2.26) shows the typical solution color after the solvothermal process for different elements.^[98]

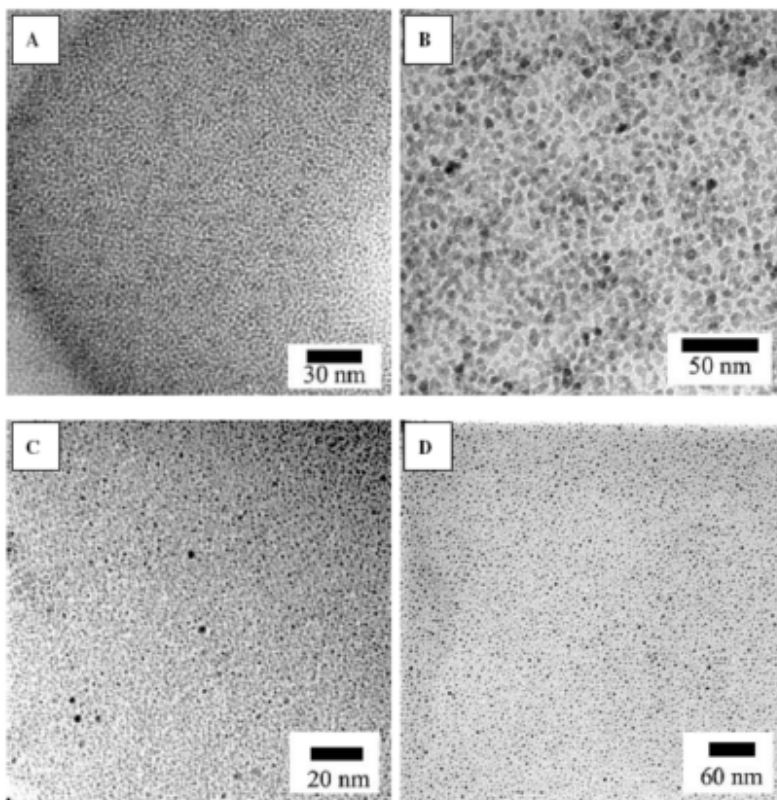


Figure 2.27 (A) Bright-field image of FeCo nanoparticles drop-cast on a carbon-coated Cu grid showing particle size around 5–6 nm. (B) Bright-field image of FeCo film directly grown on a Cu grid under the same condition as in (A), having average particle size around 9–10 nm. (C) Bright-field image showing a FePt nanoparticle film formed on the 100 plane of a NaCl crystal. The particle size was found to be around 1–1.5 nm. (D) Gold nanoparticle film formed directly on a carbon-coated TEM grid with particle size around 2–3 nm.^[98]

The commonly used substrates, such as silicon, glass and alumina have to be cleaned at the beginning by immersing it in the boiling trichloroethylene, followed by immersion in

boiling acetone. Then the substrates were ultrasonicated in isopropyl alcohol followed by washing in flowing de-ionized water for grease and organic deposits removal. Next step was to store the substrates overnight in chromic acid and finally washed in both boiling aqua regia and flowing de-ionized water at separate stages and drying. Nanoparticles were prepared by using the common used technique; however it is necessary to use a 75 ml stainless steel autoclave/solvothermal reactor in order to allow the synthesis carried out at low-boiling point solvents such as toluene. [98]

Table 2.1 Characteristic of transition and noble metals nanoparticles using solvothermal technique. [98]

	Transition metals & their alloys	Noble metals
Nature of the substrates	Smooth, dense and good quality thin films on glass, silicon and mica, metal and Teflon surfaces	Not as dense
Particle size	Much larger when compared to noble metals hence forming better deposition	Relatively small
Pressure, temperature and duration	<ul style="list-style-type: none"> • ↑ thickness as pressure ↑ by changing the filling fraction in the autoclave • ↑ thickness as deposition time ↑ • Linked to the agglomeration and growth of the particle 	<ul style="list-style-type: none"> • Form the deposition at much lower temperature • Increase in temperature will lead to significant coarsening of the particles
Adherence on the thin films	Strongly adherent due to the chemical bonding between the nanoparticles and substrate	Relatively weaker when compared to transition metals. However this adherence will increase when they are coated on functionalized substrates

The substrates are placed vertically in the autoclave held by aluminum/Teflon sample holder. Sample must be washed with acetone and then methanol. These TEM images (Figure 2.27 A and B) show the bright-field images of FeCo particles formed in the solution (nanoparticles size $\sim 5\text{-}6\text{nm}$) and in the film (nanoparticles size $\sim 9\text{-}10\text{nm}$). Figure 2.27 C displays FePt nanoparticles film prepared on NaCl substrate and moved to a carbon-coated grid (size $\sim 1\text{-}1.5\text{nm}$); and Figure 2.27 D a gold nanoparticles film prepared on a carbon-coated grid (size of $\sim 2\text{-}3\text{nm}$).^[98] Table 2.1 summarizes the particle characteristics by using solvothermal technique.^[98]

2.2.2.2 Hydrochemical Method

Hydrochemical method means the chemical reactions occur in water or aqueous solution but not in organic or polyol solutions. Its advantages in synthesis of metal and other nanoparticles can be summarized as below^[99]:

- (1) promising uniform size,
- (2) simple so that it can be used to understand readily the growth mechanism, and
- (3) the growth rate is relatively slow, which is favorable for kinetically control.

In a hydrochemical method, various techniques can be combined to prepare the nanoparticles under different conditions, described briefly as below.

2.2.2.3 Photochemical Method^[98]

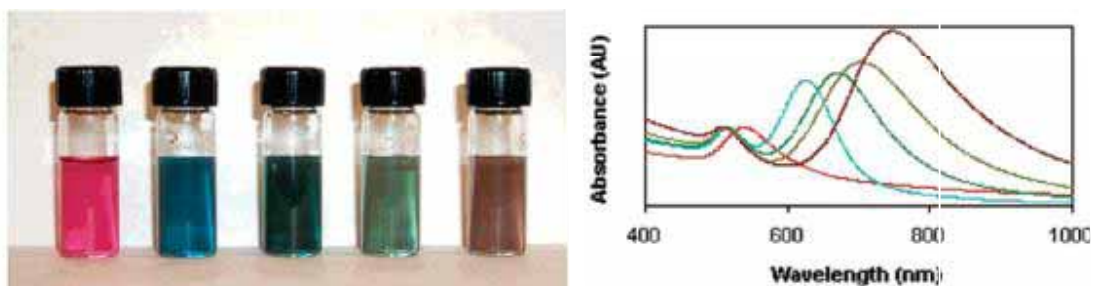


Figure 2.28 (a) Image of photochemically prepared gold nanorods solution, and (b) corresponding UV-vis spectrum. The leftmost solution was prepared with no silver ion addition. The other solutions were prepared with addition of 15.8, 31.5, 23.7, 31.5 μL of silver nitrate solution, respectively. The middle solution was prepared with longer

irradiation time (54 h) compared to that for all other solutions (30 h), and the transformation into shorter rods can be seen.^[99]

The growth solution containing gold salts and others such as surfactants and reducing agents, was irradiated with a 254-nm UV light ($420 \mu\text{W}/\text{cm}^2$) for about 30 h. The resulting solution was centrifuged at 3000 rpm for 10 minutes, and the supernatant was collected, and then centrifuged again at 10,000 rpm for 10 minutes. The precipitate was collected and redispersed in deionized water. The colour of the resulting solution varies with the amount of silver ions added, which is indicative of gold nanorods with different aspect ratios^[98] as shown in Figure 2.28.

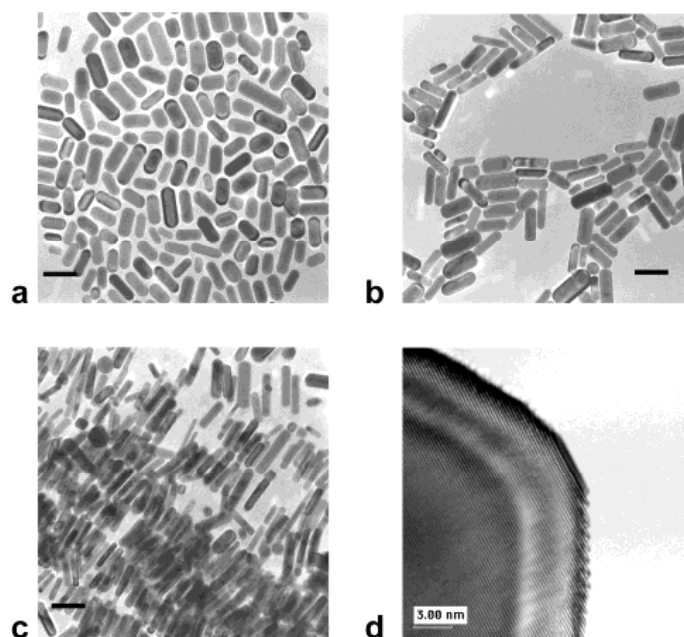


Figure 2.29 Transmission electron microscopy (TEM) images of gold nanorods prepared with (a) $15.8 \mu\text{L}$, (b) $23.7 \mu\text{L}$, (c) $31.5 \mu\text{L}$ of silver nitrate solution. The bar indicates 50 nm. (d) High-resolution image of a gold nanorod.^[99]

Seen from Figure 2.28 two absorption peaks were obtained, which resulted from the longitudinal and transverse surface plasmon (in the UV-vis spectrum) that indicates gold nanorods are formed when silver ions are added.^[99] The addition of silver ions could affect the growth of Au nanorods, Figure 2.29 shows the TEM images of gold nanorods

produced by addition of different amounts of AgNO_3 solution. An apparent increase in the aspect ratio accompanied with a decrease in the diameter was observed when more silver ion is added. Nevertheless, one limitation was addressed on how much silver ion can be added, and with the current conditions the largest aspect ratio could be obtained was ~ 5 . However, longer rods could be expected by controlling the concentration of gold.

In addition, irradiating the solution with UV light for an excess time produces shorter rods under a given silver ions concentration because the transformation of the rods into the thermodynamically more stable spherical form. TEM studies at different stages during the growth have been carried out. Preliminary results indicated that irregular polycrystalline particles of both gold and silver alloy were produced in the early stage right before the formation of rod. This is quite surprising since elemental analysis using energy dispersive X-ray spectroscopy (EDS) confirms that there is little or no detectable amount of silver within the final gold nanorod products. For comparison, time-resolved TEM studies on the electrochemical nanorod synthesis were also concluded, and it was found that the polycrystalline nanoparticles similar at the initial stages.^[99] To understand the mechanism of the rod formation, controlled experiments have been carried out. It was expected that Ag ions (in form of AgBr) were photochemically reduced into Ag nanoclusters through the UV irradiation in the absence of AuCl_4^- ions. Nevertheless, these Ag clusters can be oxidized back into AgBr in the presence of AuCl_4^- ions. This confirms that the absence of Ag in the final nanorod products. Amusingly, nanorods with similar aspect ratios are observed when chemically synthesized Ag nanocrystals added in the photochemical process.^[99]

A rod-like micellar templating mechanism is less likely in the current process since direct UV photo reduction of AuCl_4^- ions in the absence of Ag results in mainly spherical particles, indicating that silver plays a vital role in regulating the nanocrystal shapes.^[99] It can be seen that this redox dynamics varies the growing surfaces of Au nanocrystals in an as yet-to-be-determined manner, and afterwards the growth rate along a particular direction is increased. It is worth to note that the previously reported electrochemical

method ^[16] and photochemical method ^[99] have also relied on silver ion addition for controlling the aspect ratio.

2.2.2.4 Electrochemical Method

Wang, et. al., ^[99] firstly introduced an electrochemical route to form gold nanorods. The idea of electrochemical is just a package of electrochemical cell. Thus to synthesize uniform Au nanorods using this particular technique would involve a simple two-electrode type electrochemical cell as can be seen from the Figure 2.30 (a). And Figure 2.30 (b) shows the TEM images of Au nanorods formed using this technique.

In a representative electrochemical process, the following conditions are necessary and important:

1. Current of 3 mA and electrolysis time 30 minutes
2. Gold metal plate (3 cm x 1 cm x 0.05 cm) as a sacrificial anode
3. A platinum plate similar as a cathode (3 cm x 1 cm x 0.05 cm)
4. Electrolytic solutions to immerse the both electrodes at 36 °C, it contained:
 - A cationic surfactant, for example: hexadecyltrimethylammonium bromide (C₁₆TAB) to support the electrolyte and to behave as the stabilizer for the nanoparticles to prevent aggregation
 - A small amount of a tetradodecylammonium bromide (TC₁₂AB) as a hydrophobic cationic surfactant to allow rod-inducing cosurfactant
 - Appropriate amount of acetone added to the electrolytic solution for loosening the micellar framework to assist the incorporation of the cylindrical-shape-inducing cosurfactant into the C₁₆TAB micelles
 - Suitable amount of cyclohexane to enhance the formation of elongated rod-like C₁₆TAB micelles
 - A silver plate is gradually immersed close to the Pt electrode to control the aspect ratio of Au nanorods

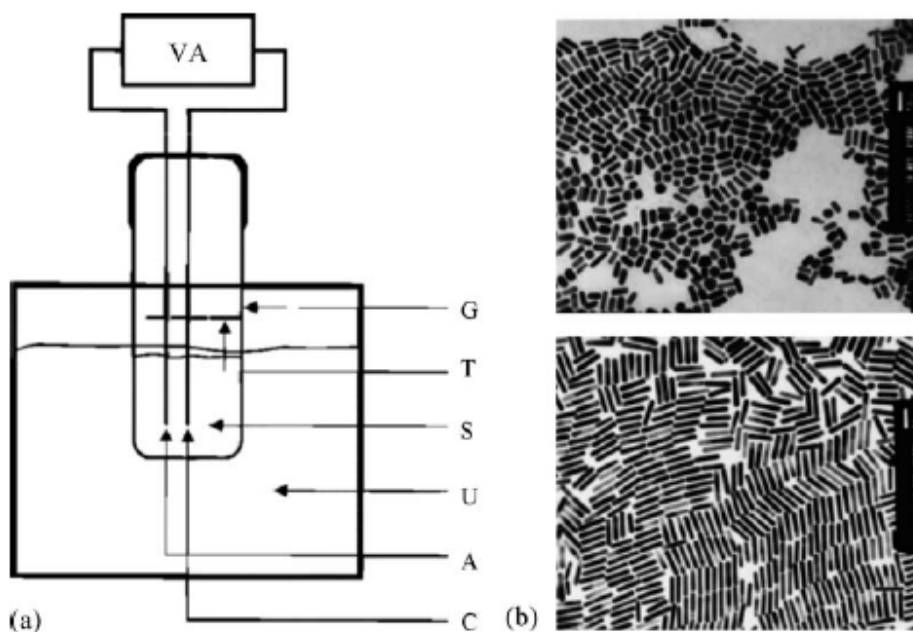


Figure 2.30 (a) Schematic diagram of the set-up for preparation of gold nanorods via the electrochemical method containing; VA, power supply; G, glassware electrochemical cell; T, teflon spacer; S, electrode holder; U, ultrasonic cleaner; A, anode; C, cathode. (b) TEM micrographs of Au nanorods with different aspect ratios 2.7 (top) and 6.1 (bottom). Scale bars represent 50 nm. ^[100]

The gold is consumed during the synthesis of AuBr^- ions, combining with the cationic surfactants. And then relocated to the cathode to allow the reduction occurs. The nucleation itself is occurred either on the cathode surface or within the micelles. The following step was sonication that is necessary to shear the resultant rods as the formation was away from the surface or in another case to break the rod off the cathode surface. The gold ions generated from the anode would react with silver plate and produce silver ions.

The microstructure of gold nanorods can be checked using TEM and HRTEM. It was found that there was a tendency to align the rods on the substrate after dried, with an even spacing between short rods. This is affected by the shape effect, concentration and the length of the surfactant capping molecules.

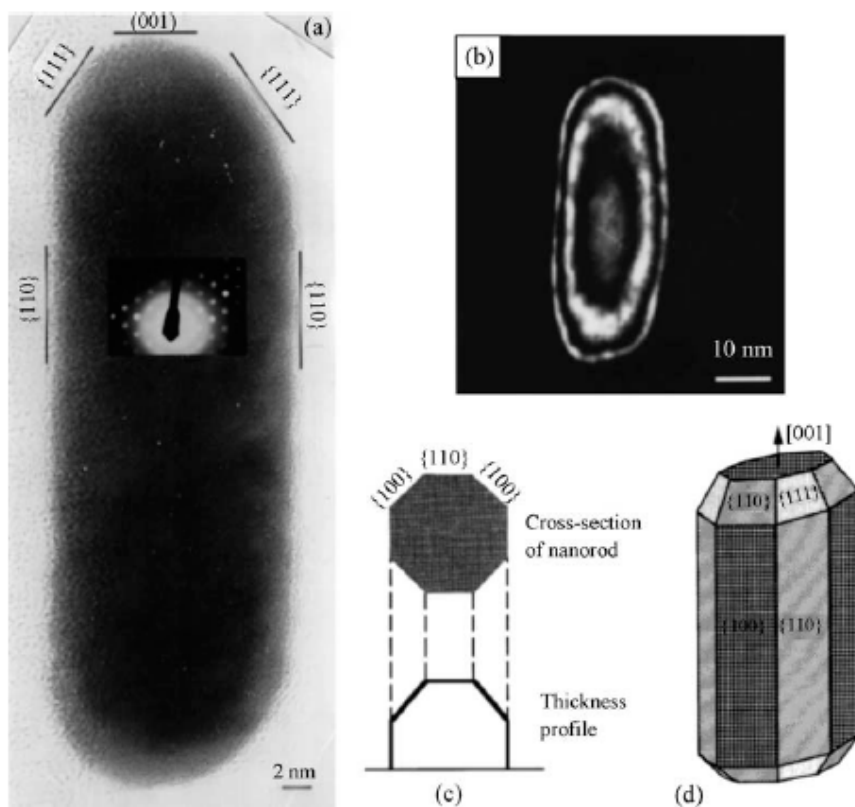


Figure 2.31 (a) High-resolution TEM image of a gold nanorod showing the faceted crystal structure of the rod. The inset is the electron diffraction pattern, which confirms its single crystalline structure. (b) Dark-field TEM image of a gold nanorods. Cross-section and the corresponding profile of crystal thickness (c) as well as the structural model (d) proposed by Wang et al. ^[73]

Based on the diffraction contrast, the nanorods are single crystal without stacking faults, and lie on the substrate through the $\{110\}$ face preferentially, although some of them are lying on $\{100\}$ face. Figure 2.31(a) shows a HRTEM image of single short nanorod oriented along the $[110]$ direction, where the dominant side faces being $\{110\}$. It grew along $[001]$; the edges are ended by the $\{001\}$ and $\{111\}$ faces moreover the $\{100\}$ faces present at the side of the nanorods hence there will be a broad centre band. This is confirmed by the dark-field TEM technique shown in Figure 2.31 (b). So the cross-section of the nanorod can be illustrated as seen from Figure 2.31(c) and hence the geometrical structure can be simulated as Figure 2.31(d). ^[73]

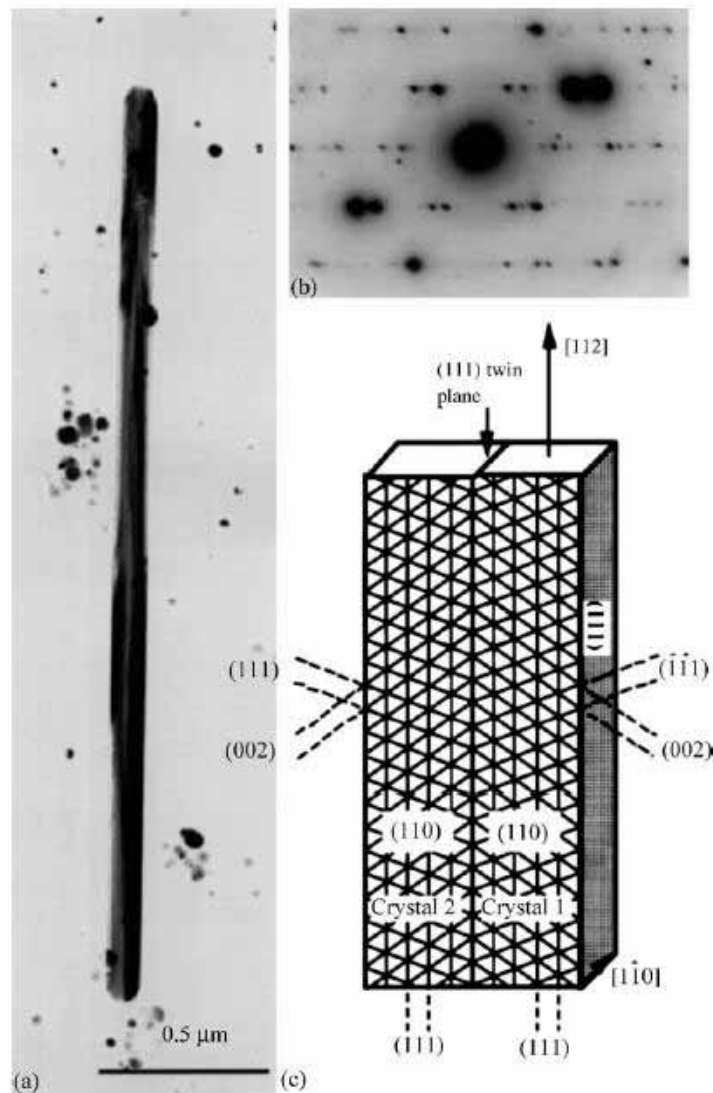


Figure 2.32 (a) TEM image of a long nanorods; (b) the corresponding electron diffraction pattern; (c) the proposed structure model for long gold nanorods. ^[73]

Different from short rods, the long rods display a twin plane parallel to their axes. Figure 2.32 (a) and (b) confirm the presence of a twin parallel to the axial growth direction. FCC Au has {111} twin planes. The main difference between short and long rods prepared by using electrochemical method is the fact that short gold nanorods are single crystals with {110} and {100} as dominant faces, but twin planes of {111} and {110} as dominant facets for long rods (Figure 2.32 (c)). ^[73]

2.2.2.5 Microwave-Polyol Method

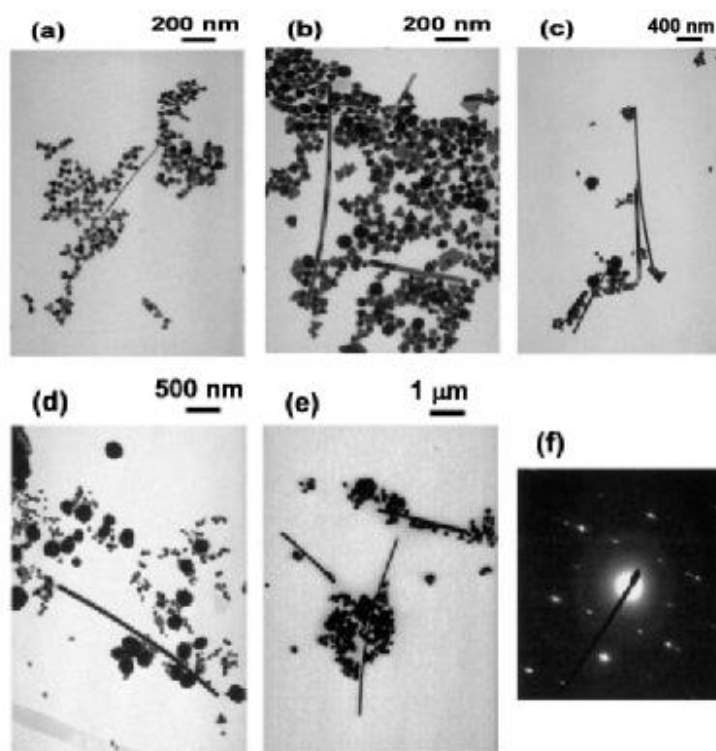


Figure 2.33 TEM photographs of gold nanostructures obtained by MW heating after 2 min. $\text{HAuCl}_4 \cdot 4\text{H}_2\text{O}/\text{PVP}$ molar ratios were (a) 1.2×10^{-3} , (b) 4.7×10^{-3} , (c) 9.3×10^{-3} , and (d) 1.9×10^{-2} at a PVP concentration of $1.03 \text{ mmol}/\text{dm}^3$, and (e) 9.3×10^{-3} at a PVP concentration of $2.06 \text{ mmol}/\text{dm}^3$, (f) Electron diffraction pattern of the longest nanowire shown in panel (e).^[101, 102]

One rapid method to reduce hydrogen tetrachloroaurate (HAuCl_4) is the microwave (MW)-polyol method. It is very promising for the fast synthesis of gold nanostructures in particular. It was found that HAuCl_4 can be reduced in methanol, ethanol or dimethylformamide (DMF) for 0.5-5 min in the occurrence of non-ionic polymer polyvinylpyrrolidone (PVP) under MW heating (480-1100 W), where monodispersed small spherical Au nanoparticles with diameters below 11 nm were synthesized.^[101, 102] Spherical Au nanoparticles with diameter of 13-85 nm can be prepared by reduction of HAuCl_4 in an aqueous solution if using citrate as a stabilizer but it took 15-30 minutes.^[101, 102] By this method, single crystal two-dimensional triangular, truncated-triangular,

square, pentagonal, and hexagonal Au nanoplates, as well as one-dimensional Au nanorods and nanowires could be successfully produced by reducing HAuCl_4 in ethylene glycol (EG) at 198 °C involving PVP within a few minutes. ^[101, 102] Another study reported that Au nanorods and nanowires can be obtained via reduction of HAuCl_4 in EG under MW heating also involving PVP/sodium dodecyl sulfate/SDS/CTAB at 160 °C. Furthermore, it was emphasized that Au nanorods can also be synthesized in an aqueous solution in the presence of cationic surfactant tetradecylammonium bromide (TOAB) as a surfactant under MW heating, and found that high aspect ratios of Au nanorods could be produced at higher TOAB concentration and faster rising reaction temperature. ^[101, 102]

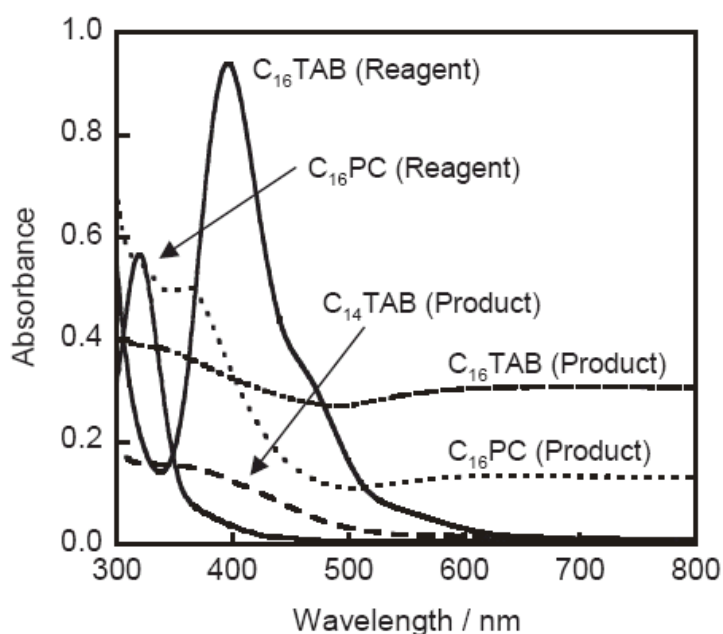


Figure 2.34 UV-vis absorption spectra of reagent solutions of $\text{HAuCl}_4 \cdot 4\text{H}_2\text{O}/\text{EG}/\text{C}_{16}\text{TAB}$ and $\text{HAuCl}_4 \cdot 4\text{H}_2\text{O}/\text{EG}/\text{C}_{16}\text{PC}$ and product solutions of $\text{HAuCl}_4 \cdot 4\text{H}_2\text{O}/\text{EG}/\text{C}_n\text{TAB}$ ($n = 14, 16$) and $\text{HAuCl}_4 \cdot 4\text{H}_2\text{O}/\text{EG}/\text{C}_{16}\text{PC}$ after MW irradiation for 2 min. ^[101, 102]

The MW-polyol equipment used here was MW oven that already been modified by installing a condenser and thermocouple through holes of the ceiling and a magnetic stirrer coated with Teflon at the bottom. In a typical procedure a three-necked flask about 100 ml was connected to the condenser and placed in the MW. The mixture of

HAuCl₄·4H₂O (2.5 mM) and C_nTAB (50 mM) in 20 ml EG was irradiated by MW in a continuous wave mode. After about 1 min, the mixture was quickly heated to the boiling point of EG (198 °C) and held in this particular temperature for 1 minute. Product was then centrifuged at 13,000 rpm for 30 minutes. The precipitation was then redispersed in deionized water for TEM observation. Figure 2.33 (a-d) shows the TEM images of the products obtained at four different HAuCl₄·4H₂O/PVP molar ratios and at a constant PVP concentration of 1.03 mmol/dm³. Seen from the TEM images, different shapes and sizes of Au nanoparticles were synthesized, and the molar ratios between AuCl₄⁻ and PVP produced slight effect on the shape/size of the final product. ^[101, 102] The UV-vis absorption spectra are useful to predict nanostructure based on the analysis of surface plasmon resonance (SPR) band of Au. Isotropic spherical Au nanoparticles show one single SPR band central around 580 nm, whereas anisotropic polygonal Au nanoplates present a broad SPR in the 550-800 nm region. ^[101, 102]

Figure 2.34 shows the UV-visible absorption spectra obtained from the reagent solutions of HAuCl₄·4H₂O/EG/C₁₆TAB and HAuCl₄·4H₂O/EG/C₁₆PC, and particle solution prepared with the assistance of C₁₄TAB, C₁₆TAB and C₁₆PC. The reagent solution of HAuCl₄·4H₂O/EG/C_nTAB produces a strong absorption due to the C_nTA⁺-AuCl₄⁻ ion pair for the case of C₁₆TAB at about 400 nm. On the other hand, no SPR band is observed from product absorption spectrum probably due to the fact that spherical nanoparticles are composed of aggregates of smaller nanoparticles in case of C₁₄TAB. In addition to the case C₁₆TAB, a strong C₁₆TA⁺-AuCl₄⁻ ion pair peak at 400 nm disappears and a weak SPR band is observed in the 500-800 nm region after 2 min reaction. ^[101, 102] In contrast to C₁₆PC, a strong SPR peak is obtained at 328 nm before MW heating, showing that C₁₆P⁺-AuCl₄⁻ ion pair is not produced. A similar broad SPR band is observed in the 500-800 nm region after 2 minute reaction. This emphasizes that optical property of spike balls is similar to that of polygonal plates. ^[101, 102]

In this technique, the formation of Au particle are described as Eq. 2.27 and 2.28: ^[101, 102]





The anisotropic Au nanoparticles formed according to the equation reaction (2.28), in which the Au^{3+} are reduced to Au atoms. C_{16}TAB groups are attached to the shell of these crystal particles, which slowed down the growth speed of the crystal facets. The surface free energy of cubic crystal is in the order of $\gamma_{\{110\}} > \gamma_{\{100\}} > \gamma_{\{111\}}$. C_{16}TAB is likely to attach to the lowest energy $\{111\}$ facet and hold back the growth rate of this facet. This results in anisotropic polygonal plates covered by $\{111\}$ facet. ^[101, 102]

Referring to the reactions above, the nucleation and growth process of gold yield a mixture of polygonal plates and close-to-spherical nanoparticles due to the presence of a polymeric surfactant (PVP) that can chemically adsorb onto the surfaces of gold particles, these nanoplates and nanoparticles were well dispersed. This chemical adsorption occurred through an interaction between $\text{N}-\text{C}=\text{O}$ group and Au. The large particles have lower surface energies than those of smaller ones, so that some small nanoparticles are grown to larger ones via an Ostwald ripening process. Some of the large nanoparticles were grown into anisotropic rodshaped and wire structures with the assistance of PVP. PVP behaves as a kinetic growth rate controller of certain crystalline faces through adsorption and desorption, and hence leads to an anisotropic growth. ^[101, 102]

Furthermore, particle shape changed significantly when hydrophilic group was changed from C_{16}TAB to C_{16}PC . This means that hydrophilic group; counter anion (e.g., Br^- or Cl^-) also plays an important role for shape control. The isotropic structure of spike ball suggests that there is no strong adsorption selectivity for specific surface in the case of C_{16}PC . ^[101, 102] Figure 2.35 shows possible formation processes of Au nanoparticles prepared using cationic surfactants. The cationic head group interacts strongly with the $\{111\}$ facets of Au nanoplates, and the C_{16}TAB formed bilayer structure due to Van der Waals force between hydrophobic groups in the case of C_{16}TAB . In contrast to shorter alkyl chain C_nTAB ($n=10, 12$ or 14) and C_{16}PC , the bonding of cationic parts with specific surface become weak and hence spherical particles are produced.

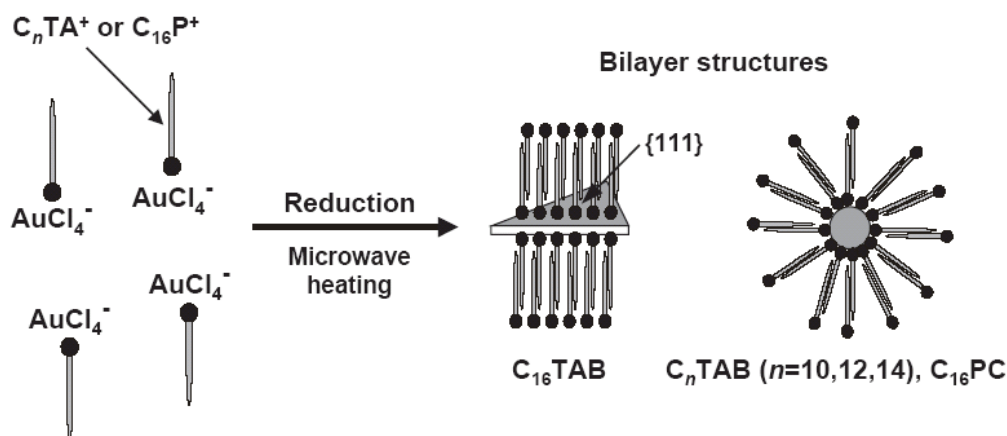


Figure 2.35 Possible formation processes of Au nanoparticles prepared by the MW-polyol method with the assistance of cationic surfactants C_nTAB and $C_{16}PC$. ^[101, 102]

Although a previous study ^[101, 102] reported that in aqueous solution at room temperature, rod-like micelle is formed using C_nTAB ($n=12, 14, 16$) no rod-like micelle was found in the present MW-polyol method. It can be concluded that the stability of plate-type and spherical bilayer micelles is higher than that of rod-like micelle under MW irradiation at a high temperature of 198 °C. ^[101, 102]

2.2.2.6 Gamma Irradiation

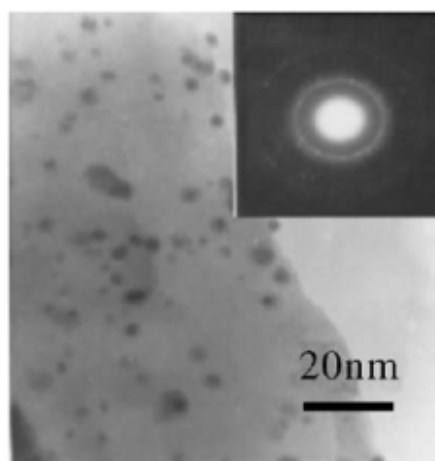
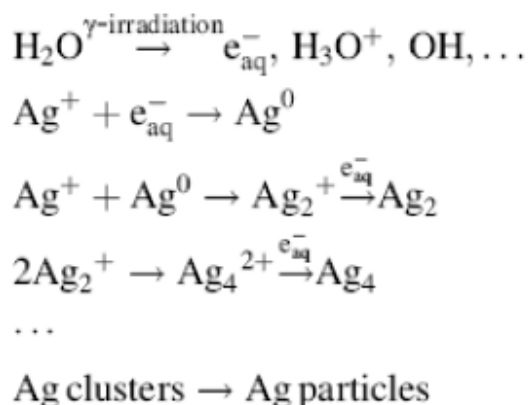


Figure 2.36 The TEM morphology micrograph of the Ag-adopted SiO_2 film under irradiation by γ -ray for 4 h, the inserted image is the corresponding selected area electron diffraction pattern. ^[103]

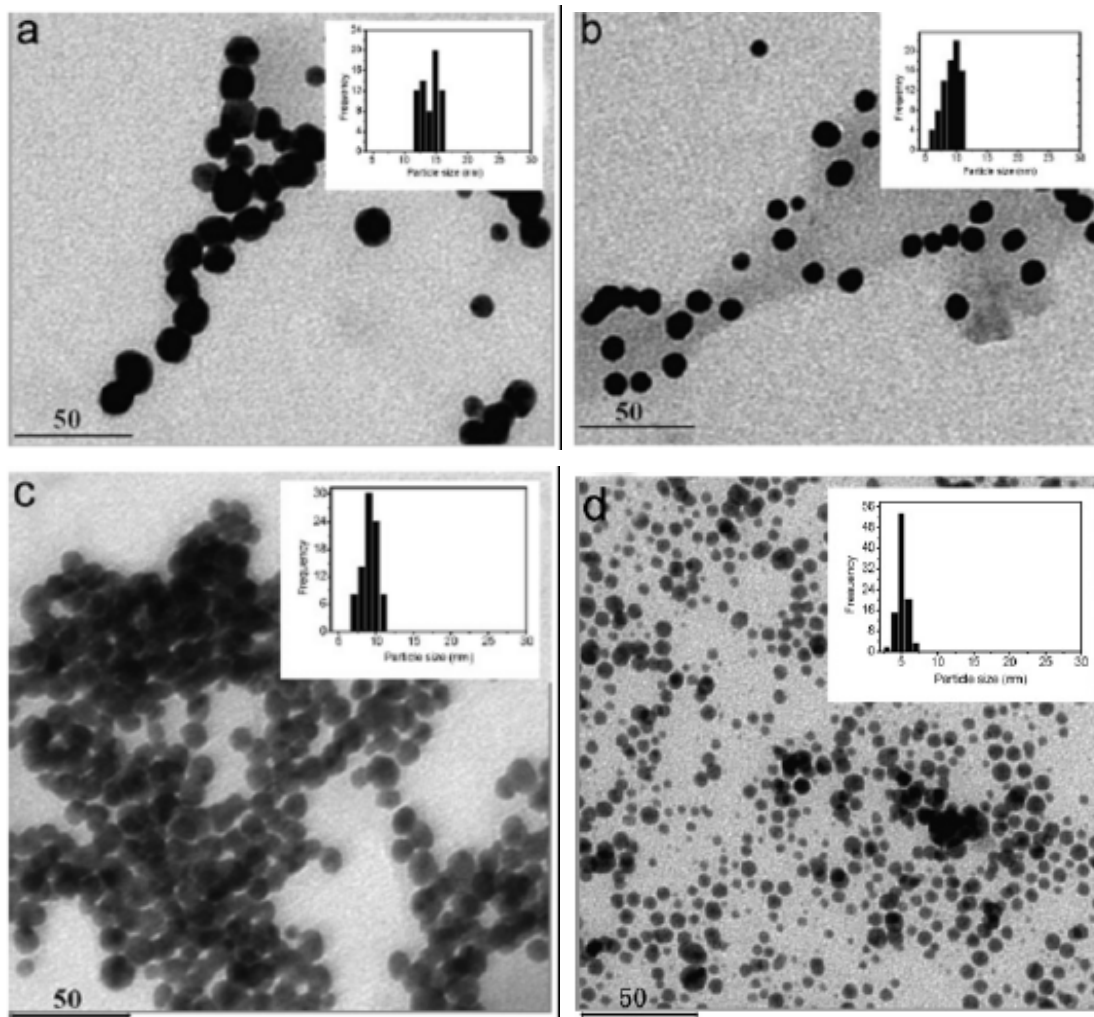


Figure 2.37 TEM images of Ag nanoparticles containing (a) 1.0×10^{-3} M; (b) 4.0×10^{-4} M; (c) 2.0×10^{-4} M and (d) 1.2×10^{-4} M silver and histograms of particle size distribution (inset). [104]

To develop novel nano-materials with unique properties, gamma-irradiation has been used due to its advantages such as room temperature, ambient pressure and easily controlled. In this section, the gamma-irradiation method will be introduced with combination of sol-gel process and dip-coating technique to produce silver nanoparticle doped mesoporous SiO₂ films. The irradiation reactions can be summarized as following. [103]

Following TEM images (Figure 2.37) show the same samples of silver nanoparticles produced by gamma-irradiation. Figure 2.38 shows their UV-vis absorption. In the absence of Ag particles, no obvious surface plasmon band; whereas the doped Ag nanoparticles can lead to strong surface plasmon resonance centred around 400 nm, which is consistent with result in the literature.^[103] This means that the gamma-irradiation method can produce highly dispersed Ag particles with controlled size.^[103]

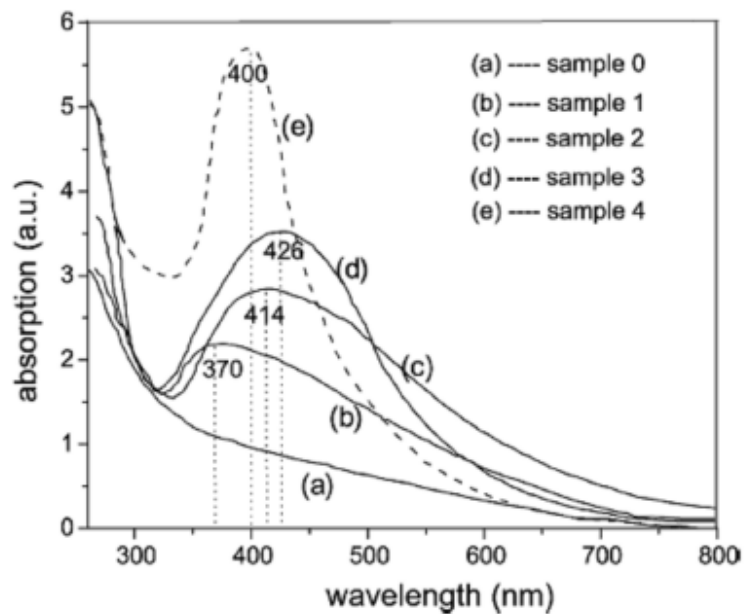


Figure 2.38 Optical absorption spectra for the mesoporous SiO₂ film without doping (a) (sample 0); the mesoporous SiO₂ film soaked in 0.01, 0.05 and 0.1 M AgNO₃, respectively, and γ -irradiated for 4 h (b–d) (samples 1–3) and the annealed sample (e) (sample 4).^[103]

2.2.2.7 Ultrasonication

Besides gamma-irradiation method, another irradiation method named ultrasonication has been widely studied. As an example, we demonstrate the applicability of this technique in preparation of Au nanoprisms.^[105]

In this technique, the solution containing ethylene glycol, HAuCl₄ and PVP were ultrasonically irradiated for certain time under certain frequency at room temperature.

Before irradiation, the solution flask was cleansed with Argon gas to get rid of the oxygen, as illustrated in Figure 2.39. [105]

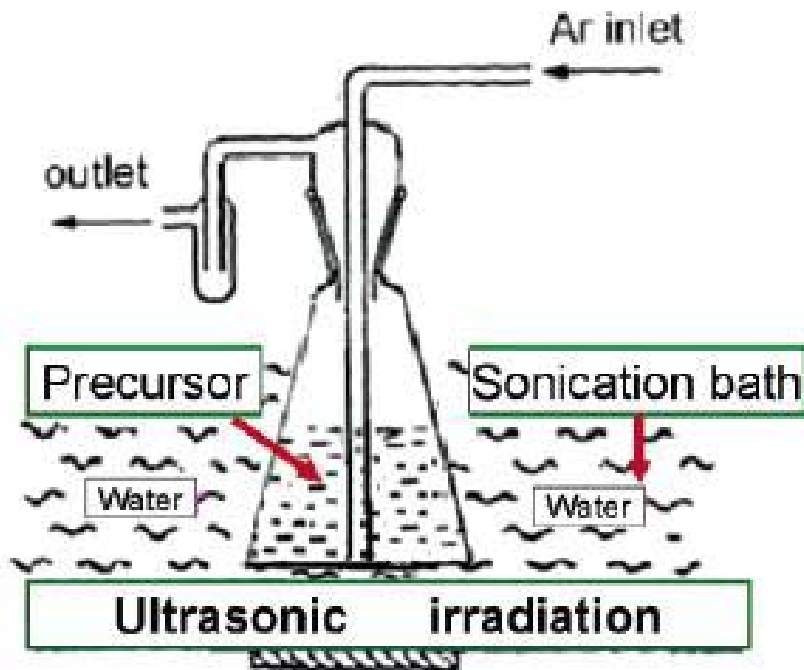


Figure 2.39 Schematic illustration of an ultrasonically irradiated process. [105]

By ultrasonic irradiation, Au nanoprisms with diameter of 30 – 70 nm can be synthesized (Figure 2.40 C-F) and the UV-vis spectra after ageing at different time (Figure 2.40 A) and when different amount of HAuCl_4 was added (Figure 2.40 B). The acoustic cavitation occurs locally and immediately in the solution, and during the irradiation, the cavitation grow up to several micrometers in dimension and sub-microsecond in time scale. Hence Au nuclei develop along favoured orientation and at the end it created platelike particles because of the surface energy of the crystal-plane-dependent and the selective adsorption of PVP. [105]

Furthermore, laser irradiation is also an irradiation technique to lead to temperature plasma, directing to the thermal decomposition and reduction of AuCl_4^- ions. Comparably ultrasonic irradiation provides a good atmosphere causing quasi-equilibrium crystal growth, but laser irradiation persuades a growth condition that leads to the equal-axis growth.

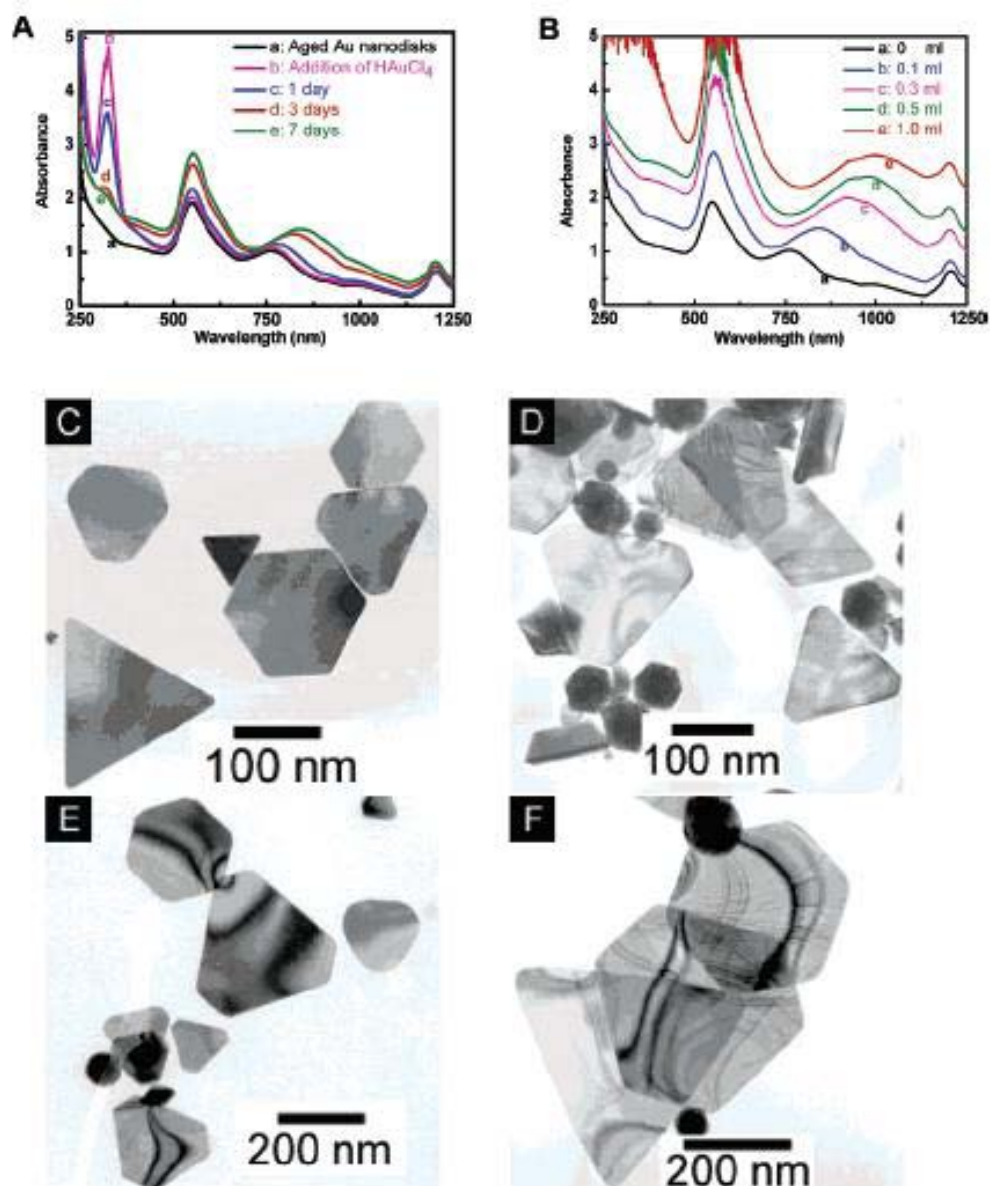


Figure 2.40 (A) Time evolution of optical absorption spectra for the aged irradiated sample (5 mL, ultrasonic-irradiated for 120 min, and then aged at room temperature for 7 days) after an addition of 0.1 mL of 25 mM H₂AuCl₄ solution. (B) The optical spectra for the samples with an addition of different amounts of H₂AuCl₄ after 7 days. (C-F) The TEM images of Au nanoprisms after 7 days for the samples, respectively, are corresponding to the addition of 0.1, 0.3, 0.5, and 1 mL of 25 mM H₂AuCl₄ solution to a 5 mL aliquot aged sample. ^[105]

2.2.2.8 Biochemical method: Aspartate Reduction

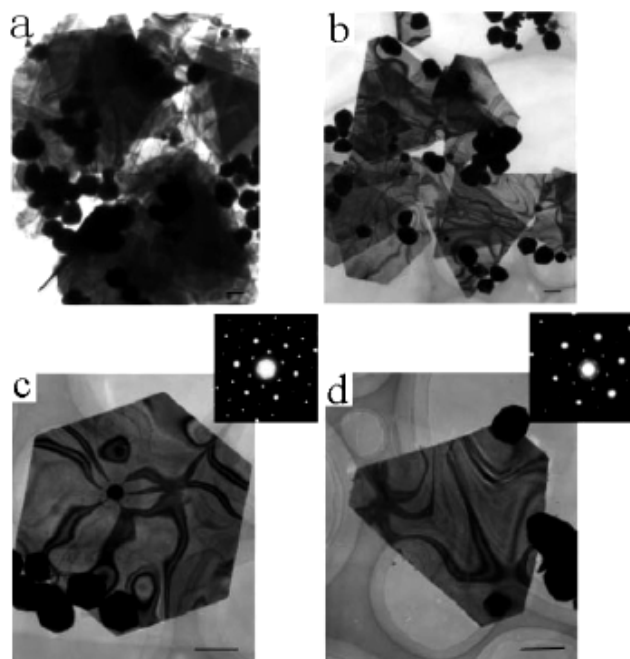


Figure 2.41 Typical TEM images of a sample prepared from a reaction solution containing aspartate, showing the high- (a) and slightly lower- (b) degree assembled nanoplates during the evaporation of solvent. The representative images of individual hexagonal and truncated triangular nanoplates are shown in (c) and (d). The insets show the selected-area electron diffraction patterns. The scale bars are 200 nm. ^[106]

Biochemical method is recently used to reduce metal ions for shape control of metal nanoparticles. Generally, certain amino acid residues from biomacromolecules or organism can be used to shape/size control of metals, such as gold nanoplates. ^[106] No additional reducing agent and surfactant were needed for the gold particle synthesis in this technique. In a typical procedure, aqueous solution containing 0.01% tetrachloroaurate and 0.5 mg/mL amino acids for 12 h reaction were carried out at 25°C. To monitor the crystals of gold nanostructures, ultraviolet-visible (UV/Vis) was used. It was found that the solution incubated with L-tryptophan changed red color immediately, confirmed by a characteristic surface plasmon absorption centred at 560 nm, which indicates the gold nanoparticles are formed. The shape/size of the products was

characterized by TEM and electron diffraction (Figure 2.41), the dominant morphology is nanoplate. ^[106]

In this case amino acid moieties from an organic matrix may influence on the specific contacts between inorganic or biomolecules materials. The above experimental results indicate that amino-acid can affect the size and morphology of the resultant gold nanostructures. In addition, such a biochemical method was extensively used to prepare silver nanoparticles by bacteria, peptides and yeast. ^[106]

2.2.2.9 Non-hydrochemical method

2.2.2.9.1 Polyol Reduction Method

Table 2.2 Synthesis conditions and characteristics for PVP-stabilized Au colloids. ^[1]

Sample code	Weight ratio (NaHCO ₃):(Au)	PVP (g)	Extinction peak (nm)	Stability	Average diameter (nm)	Standard deviation (nm)
A1	10:1	2	523	S	11.65	3.67
A2	5:1	2	524	S	11.82	4.11
A3	3:1	2	531	S	15.13	7.52
A4	1:1	2	534	S	19.75	5.36
A5	1:5	2	-	U	257.70	71.37
B1	10:1	1	526	S	12.78	3.54
B2	5:1	1	527	S	14.82	5.16
B3	3:1	1	539	S	23.70	5.06
B4	1:1	1	-	U	315.41	39.13
B5	1:5	1	-	U	-	-

Reaction time: 24h; S: stable; U: unstable.

Recently, metal nanoparticles have been prepared using polyols such as ethylene glycol, which is known as polyol process. Metal ions can be reduced by redox reaction (between the metallic precursor and the solvent) in this method. This is due to the difference between the oxidation potential of solvent and the reduction potential of metal species at a given temperature (ΔE).

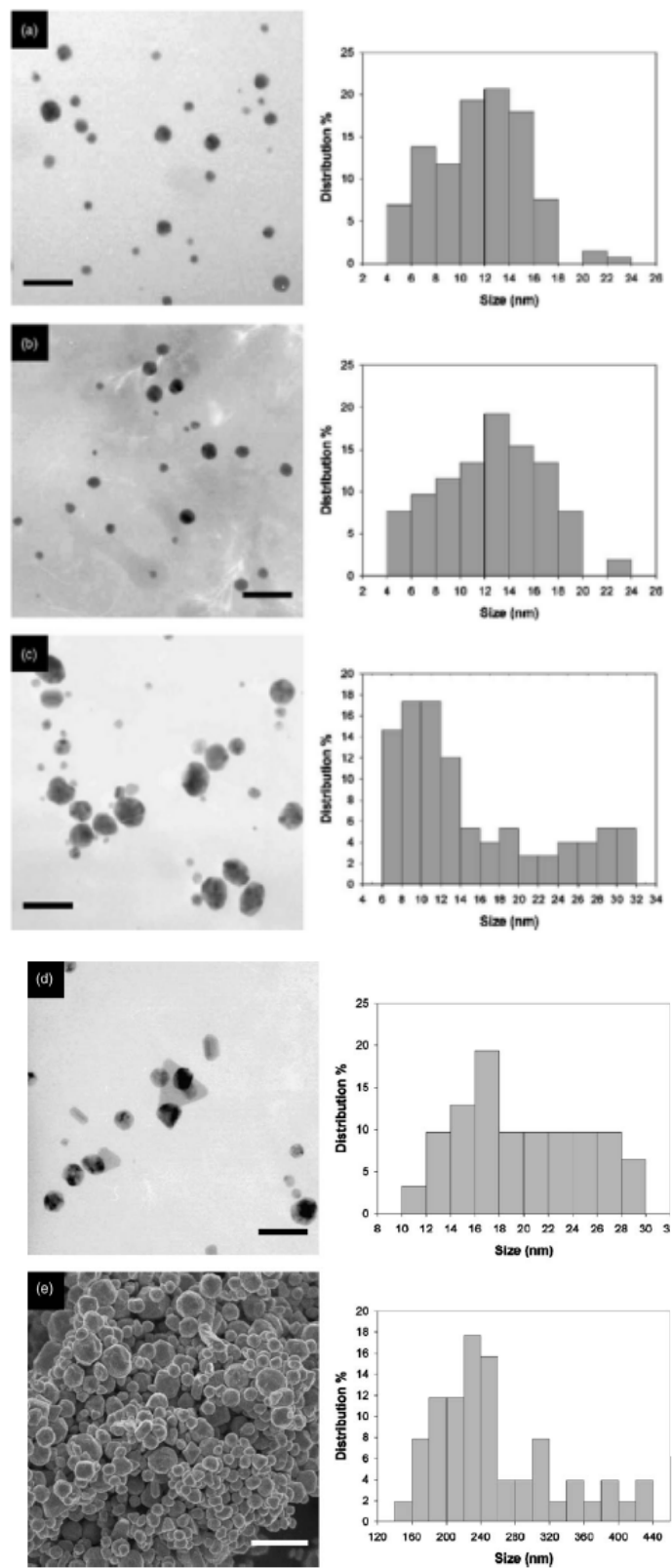


Figure 2.42 TEM images and size distributions of samples (2 g of PVP): (a) A1; (b) A2; (c) A3; (d) A4; (e) A5 (scale bar: 50 nm (A1–A4), 1 μ m (A5)).^[1]

For the reduction reaction, ethylene glycol is used as both a reducing agent and solvent. Using this method, controlling the produced metal nanoparticles can be easily obtained by adjusting the experimental conditions (Figure 2.42).^[1]

2.2.2.9.2 Template Method

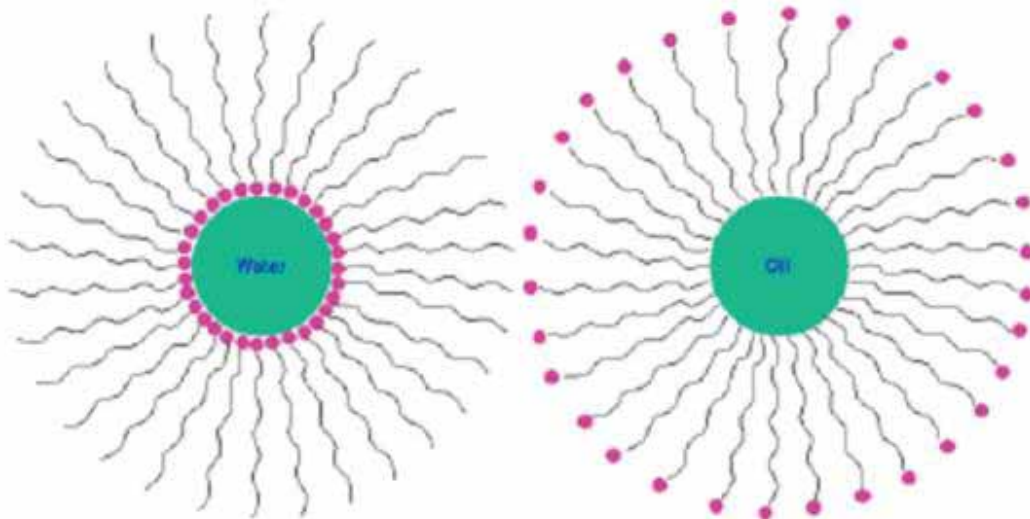


Figure 2.43 Reverse micelle and normal micelle structures.^[1]

Soft template. Soft template commonly means the micelles used for preparing nanoparticles. Micelles normally formed as the surfactant concentration exceeds the critical micelle concentration in water. There are two different kinds of micelles (micelles vs. Reverse micelles) formed by hydrophobic or hydrophilic materials as illustrated in Figures 2.43 and 2.44. The solubilization process will be enhanced when the concentration of surfactant is increased. The size of the droplet can increase bigger than the monolayer thickness of the surfactant molecules. In addition, it was found that the droplet size which controls the size of particles can be tuned by changing w , the ratio $[H_2O]/[AOT]$. A major change in the particle size is obtained at low water content.^[107]

The main difference between these two micelles is no confinement of reactants in normal micelles. Normal micelles act as a template that controls the nanoparticle size. The geometric factors of the surfactant at the interface, such as head group area R_0 , alkyl

chain volume V , and the maximum length l_c to which the alkyl chain can extend will determine the structure of micelles. ^[107]

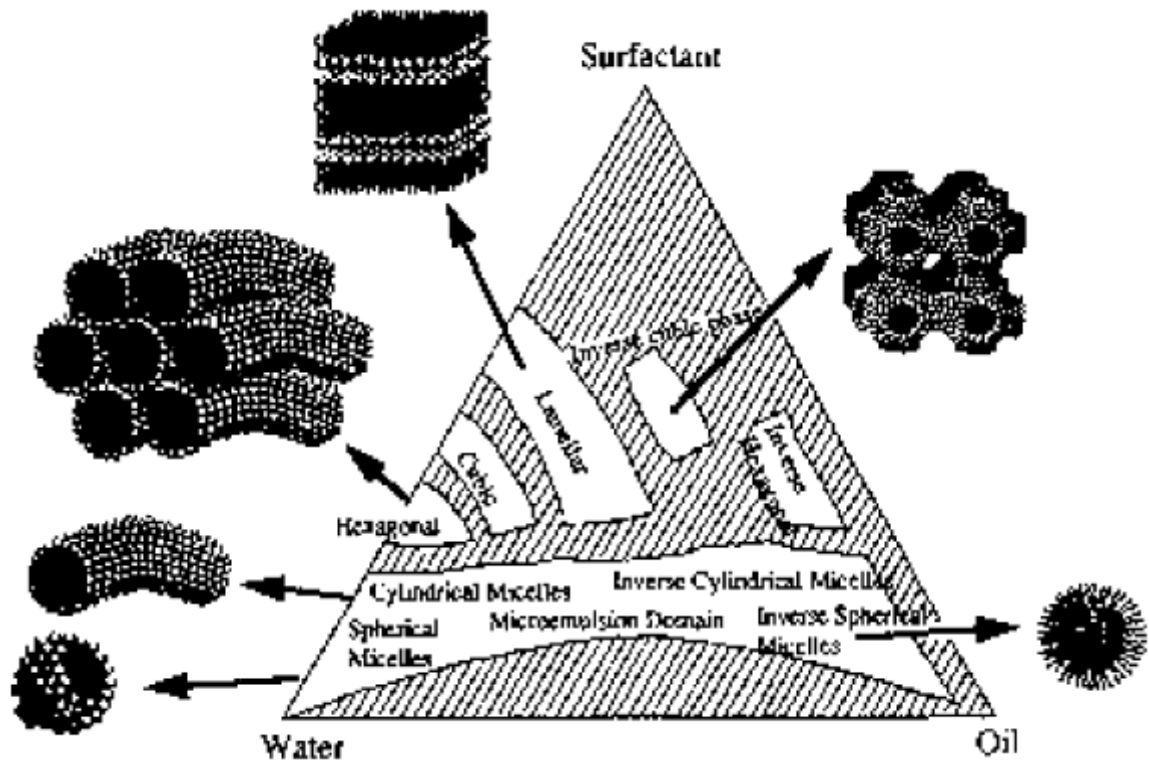


Figure 2.44 Schematic phase diagram of surfactant-oil-water systems showing a variety of self-assembled structures. ^[108]

There are a few rules on packing considerations govern the geometry of aggregation, as below. ^[107]

- (a) spherical micelles: $V/\alpha_0 l_c < 1/3$
- (b) nonspherical micelles: $1/3 < V/\alpha_0 l_c < 1/2$
- (c) vesicles or bilayers: $1/2 < V/\alpha_0 l_c < 1$
- (d) inverted micelles: $1 < V/\alpha_0 l_c$

Furthermore, micelles can be transformed into different shapes as illustrated below, when the concentration of surfactants was increases. Therefore, the synthesis of different nanoparticles shapes is possible.

Figure 2.45 shows the TEM images of the product of the synthesis of the Cu nanoparticles using this micelles method where the larger size of diameter is 12 nm.

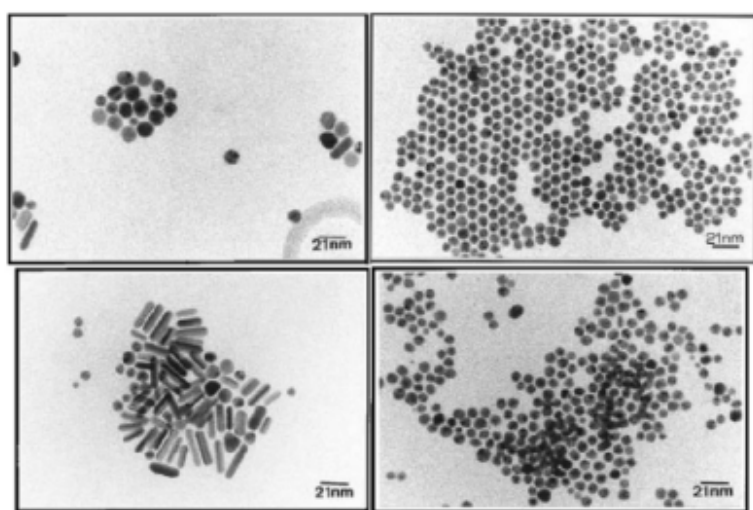


Figure 2.45 TEM images obtained after synthesis at $[\text{Cu}(\text{AOT})_2] = 5 \times 10^{-2} \text{ M}$, $w = 4, 20, 34, 40$, respectively. ^[109]

Hard Template. A new method of supporting gold nanoparticles on multiwalled carbon nanotubes (MWCNTs) with synchrotron X-ray reduction will be discussed here. The gold nanoparticles were prepared using photochemical reduction method as introduced in section 2.2.2.1 (i(a)). Carbon nanotubes have confirmed the physical and chemical reaction in catalytic reactions. Lin, et al. ^[110] studied the unique shape as a result of combination of modified MWCNTs and gold nanoparticles. Gold nanoparticles have been found to be capable of transforming CO to CO₂. Synchrotron X-ray produced by third generation synchrotron radiation facilities was employed to form hybrid Au/CNTs catalytic material. ^[110] Lin, et al. ^[110] suggested that different exposure times of synchrotron X-ray to the gold nanoparticles resulting different shapes attached on MWCNTs. The MWCNTs were boiled in concentrated nitric acid at about 150 °C for 3-6 h to remove impurities, then filtered and washed with distilled water to wash the acid away and finally dried at 80 °C overnight. Figures 2.46 and 2.47 show the TEM images of the gold nanoparticles after 3 h and 6 h treatment with acid and exposed in X-ray at different time.

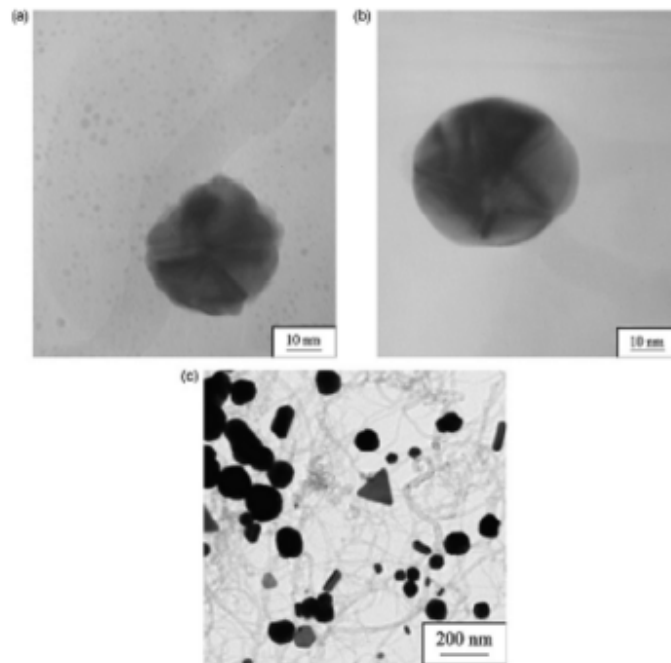


Figure 2.46 TEM images of the reacting colloids with 3 h acid treatment MWCNTs exposed in X-ray for 1, 10, and 30 min as shown in (a), (b), and (c), respectively. ^[110]

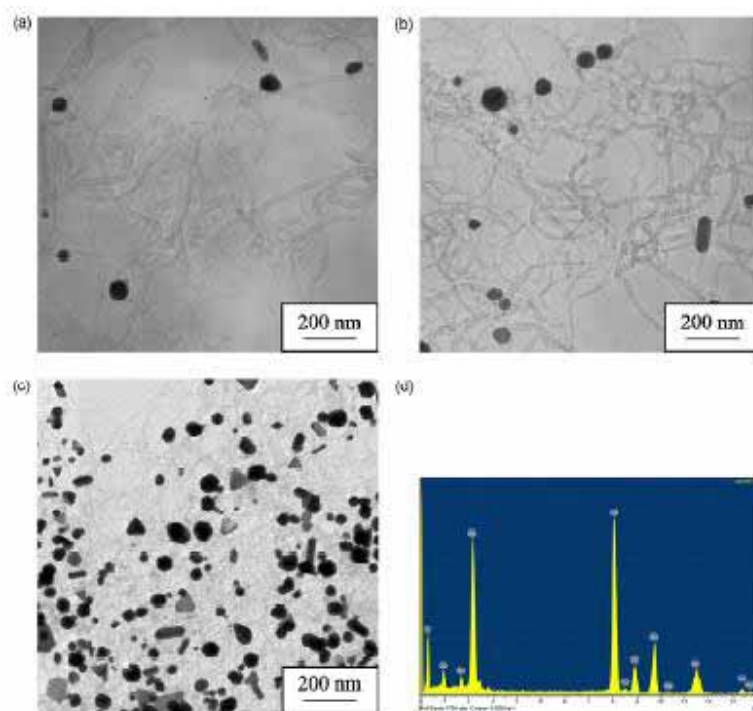
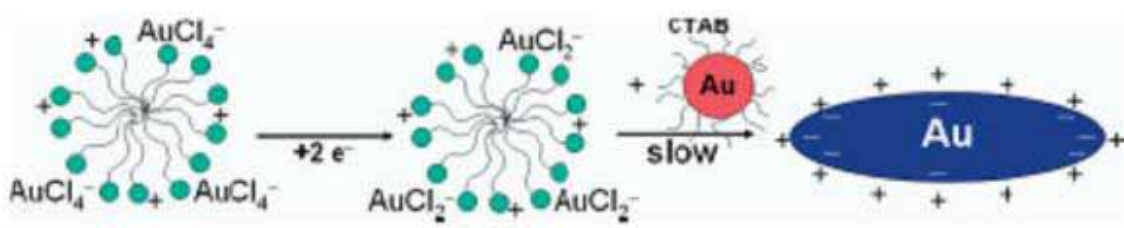
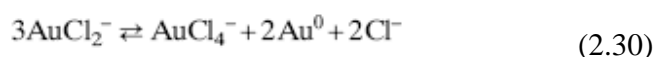
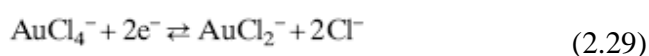


Figure 2.47 TEM images of the reacting colloid for 6 h acid treatment MWCNTs exposed to X-ray for 1, 10, and 30 min, as shown in (a), (b), and (c), respectively. The element characterization by EDS is shown in (d). ^[110]

2.3 Growth Mechanism

2.3.1 Electrical-field induced Mechanism

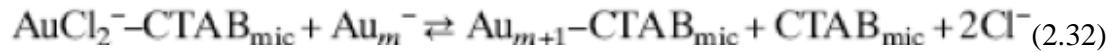
The growth of gold nanoparticles can be achieved by thermodynamically or kinetically controlling the formation of gold atoms and their orientation stacking. Gold atoms can be obtained by reducing AuCl_4^- ions through two distinct pathways. AuCl_4^- was reduced to AuCl_2^- on the surface of the micelles through Equation 2.29, and then further disproportionate on the Au colloid surface (Equation 2.30) or AuCl_2^- may directly release electron via Equation 2.31. ^[107]



Scheme 2.1 Mechanism of gold rod formation. ^[107]

Seen from the illustration in Scheme 2.1, AuCl_4^- ions are reduced on the micelle surface to AuCl_2^- ions, but remain tightly bound. Gold ions may be discharged during encounters of micelles with the CTAB-coated Au seed particles. By assuming that the electron transfer itself is not rate-determined, the rate of reaction is controlled by the collisions of the micelles. No colloidal gold is formed at this stage and the solution of AuCl_2^- -CTAB remains stable indefinitely, i.e., in a CTAB solution disproportionation of AuCl_2^- -CTAB does not occur. Moreover, J. Pérez-Juste et al. ^[107] also found that AuCl_2^- -CTAB solution can be made by adding HAuCl_4 in the presence of CTAB. This means that gold colloids are oxidized by Au^{III} in the presence of CTAB conproportionation rather than disproportionation. Therefore the binding constant of AuCl_2^- to CTAB must be really high. Based on the experimental results, a solution containing both HAuCl_4 and Au

colloids is completely oxidized in the presence of CTAB with the equilibrium constant $<10^{-2}$. So disproportionation of AuCl_2^- is not the mechanism for gold deposition or rod growth in CTAB solution. Consequently, the reduction of Au^{I} in the presence of CTAB can be described by the Equation 2.32:^[107]



When the ions are bound to micelles in solution, the rod formation will take place. The electrons are transferred to the Au particle while dissolved or absorbed AuCl_2^- ions may pick up an electron at any favourable adsorption site during normal microelectrode-type deposition. Under these circumstances, spherical growth will be obtained. On the other hand, the gold seeds or rods are encapsulated in CTAB and the gold ions are likewise micellized in CTAB. The zeta potential of CTAB micelles and CTAB-coated gold surfaces are both around +90 mV. By assuming that the rate of rod formation is determined by the frequency of collisions of AuCl_2^- -laden cationic micelles with the cationic gold seed particles, it can be worked out that the electrical double-layer interaction between micelles and gold rods is the controller (Scheme 2.1).^[107]

2.3.2 Light-induced Reconstruction Mechanism

By using femtosecond laser pulses, Au nanorods could melt into Au nanodots. This is a reverse process to the formation of nanorods (Figure 2.49). It shows the detail mechanism of the rod-to-sphere shape transformation process.^[111]

The steps for this transformation are briefly summarized as below.

1. The sides of defect-free single crystal Au nanorods are enclosed by {111} and {100} facets with small {111} facets at the corners and it grows through [011] direction (Figure 2.48a).
2. The point defects are firstly occurred in the body of the nanorods while being illuminated by pulsed laser light (Figure 2.48 b).
3. The defects formed at the initial stage served as the nuclei for the formation of the twins and stacking faults (Figure 2.48c).

- To allow the growth of the twinned crystal (Figure 2.49d), surface diffusion takes place. It is driven by the reduction of the surface energy through the decrease of the $\{110\}$ surface area and the increase of the $\{111\}$ surface.

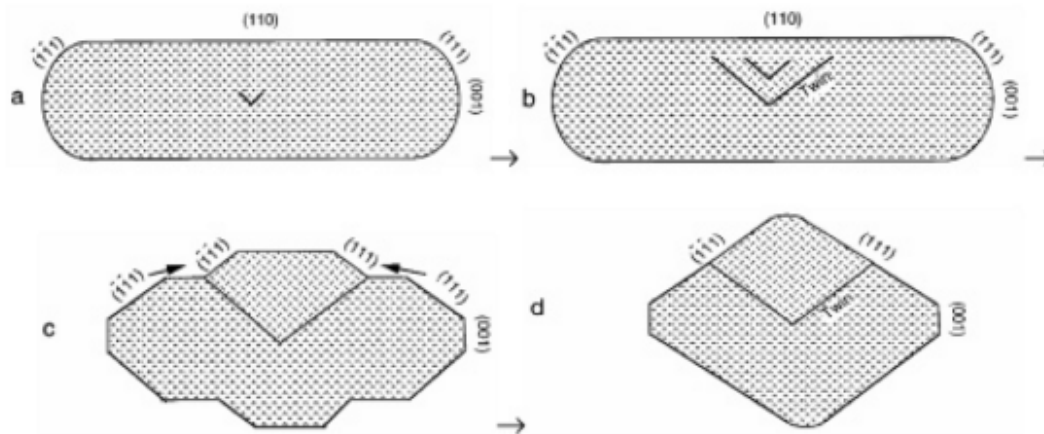


Figure 2.48 Illustration of the structural transformation process from nanorod to gold nanodot.^[111]

The unstable $\{110\}$ surface is eliminated due to the continuation of the growth of the twinned crystal and hence induced the more stable $\{111\}$ and/or $\{100\}$ facets. In the end, it covers all nanoparticle surfaces and Au nanorods transform into spherical nanoparticles. Similar mechanism has been found in the light-induced formation of silver nanodisks from small spherical nanoparticles to bigger nanodisks.^[111]

2.3.3 Stack-fault mechanisms

This growth mechanism for understanding silver nanodisks was suggested by Pileni et al.^[112] Silver nanodisks were synthesized by reverse micellar template method.^[112] Different disk-like particles such as triangular nanoprism, truncated triangular nanoprisms, hexagonal and circle disks have been studied. However, all of them have a general flat plate-like shape with the flat top surface parallel to the (111) plane of their fcc crystal structure. In a typical sample, the presence of the $1/3\{422\}$ reflections is forbidden for fcc metal structure. Figure 2.49 shows the typical selected area electron diffraction (SAED) patterns that indicate the forbidden $1/3\{422\}$ reflections (A). The

presence of these $1/3\{422\}$ forbidden reflections is caused by the (111) stacking faults lying parallel to the (111) plane and extending across the entire disk. ^[112]

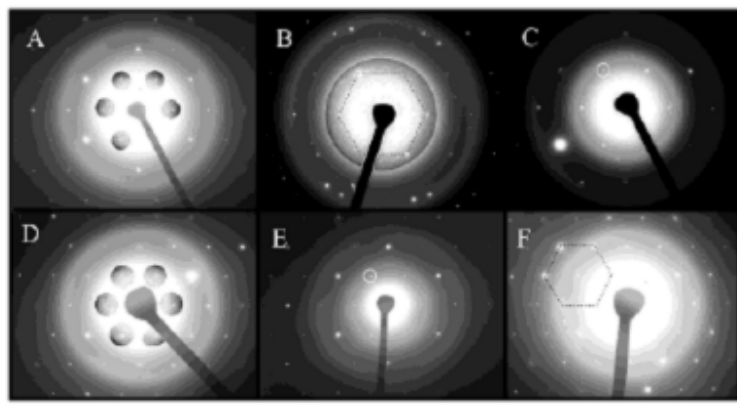


Figure 2.49 Typical SAED patterns that show the $1/3\{422\}$ forbidden reflections. ^[112]

Generally, there are two types of stacking faults: ^[112]

- (i) Stacking Fault I (intrinsic): An atomic A layer is removed and the stacking sequence is then ABCABCABC... Compared to B and C position, A position will be lower by one atom. For single stacking fault, a strong superlattice diffraction effect could be induced. It is similar to the effect caused by a single surface mono-atomic step. This is due to the subnanometer thickness of the stacking faults, their reciprocal points are elongated strongly along [111] direction. This makes it easy to intersect with the Ewald sphere and the $1/3\{422\}$ reflections will be very easy to observe in the [111] diffraction pattern.
- (ii) Stacking Fault II (extrinsic): There is an extra insertion (111) layer, A layer is added into the regular stacking sequence of ABCABCABC ..., a sequence of AB(A)CABCABC ... will occur. In comparison to B and C positions, the projected potential in A position will be one atom higher.

Moreover, it is hard to distinguish between these two models as in both cases the projected crystal potential along [111] are identical. However, if two or more (111) stacking faults exist within the nanodisk, the same effect will appear in the HRTEM image and diffraction pattern, except if there are three stacking faults produced by

intrinsic/extrinsic of A, B and C layers. This is because the different stacking faults will produce the same superlattice periodicity.^[112]

The (111) stacking fault(s) plays an important role in the formation and growth of the (111) dominated disk. The growth in parallel to the stacking fault plane is more likely the fastest. Figure 2.50 shows that the (111) stacking fault(s) planes are exist. Moreover, an accelerated growth along the (111) twin plane leads to triangular or hexagonal nanoplates.

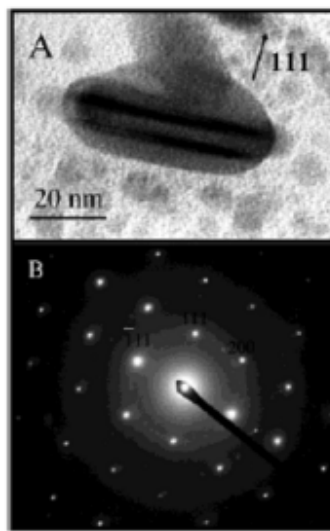


Figure 2.50 (A) TEM image of the silver nanodisk taken in side view, showing the contrast from (111) stacking faults and a preferential growth along the stacking faults. (B) A typical SAED pattern of silver nanodisk at 100 kV in the [011] orientation (side view).^[112]

For an fcc crystal structure, (111) stacking faults lying parallel to the (111) surface are found to extend across the entire disk-like particles. The existence of the $1/3\{422\}$ forbidden reflections and the $3 \times \{422\}$ superlattice fringes determine the (111) stacking fault. Based on the TEM analysis, stacking fault may be the key to the formation and growth of the nanodisks, where the shape and size managing of the nanocrystal will be possible by controlling the nucleation, growth and elimination of the defect (stacking fault). This will also give an insight to the controllable synthesis of nanoparticles.^[112]

2.4 Applications

Metal (e.g. Au, Ag) nanoparticles have found more applications in many areas, including biomedical, materials science, and catalysis. This is because of their unique properties when compared with their bulk solid. This part of the literature will give a brief description.

2.4.1 Biomedical application

2.4.1.1 Gene Delivery

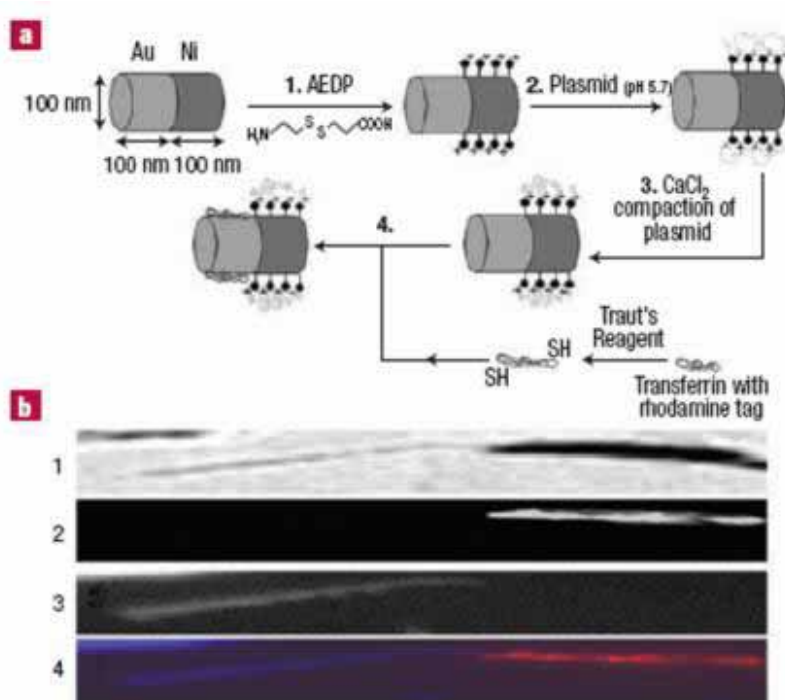


Figure 2.51 Spatially selective binding of DNA plasmids and transfer into multicomponent nanorods. (a) Illustration of nanorod functionalization. At this step, nanorods are incubated with the 3-[(2-aminoethyl) dithio] propionic acid (AEDP) linker (1). The carboxylate end-group binds to the Ni segment. The disulphide linkage acts as a cleavable point within the spacer to promote DNA release within the reducing environment of the cell. Plasmids are bound by electrostatic interactions to the protonated amines presented on the surface of the nickel segment (2). CaCl₂ compacts the surface-immobilized plasmids (3). Rhodamine-conjugated transferrin is selectively bound to the gold segment of the nanorods (4). (b) Confirmation of selective functionalization of

nanorods is observed by light and fluorescent microscopy, in which (1) Light microscope image of dual functionalized Au/Ni nanorod 20 μm long; (2) Fluorescence image of the rhodamine-tagged (633 nm) transferrin on the Au segment; (3) Fluorescence image of the Hoechst-stained (350/450 nm) plasmids on the Ni segment; and (4) Fluorescent overlay image combining b2 and b3. ^[113]

The absorption and scattering cross sections of gold and silver are 5-6 orders in magnitude larger than molecular species like organic chromophores. These allow them to be explored as a class of therapeutic and contrast agents for photo-thermal treatment and optical imaging of tumours, through finely controlling the wavelengths at absorption and scattering. ^[113]

Of the achieved gold nanoparticles, gold nanorods are particularly applicable for gene delivery. This can introduce foreign genes into somatic cells to supplement defective genes or provide additional biological functions. It can be achieved by using either viral or synthetic non-viral delivery systems. In comparison with viral vectors, synthetic non-viral delivery systems like liposomes and polymers offer a few advantages including: ease of producing, lower risk of cytotoxicity, and immunogenicity. However, they have been limited by the relatively low transfection efficiency. The following scheme shows the summary of how this gene delivery works. ^[113]

A typical example in gene therapy community is that gold nanoparticles were surface-immobilized by DNA, which is useful to intradermal genetic inoculation. Non-viral gene-delivery system based on multi-segment bimetallic nanorods can bind compressed DNA plasmids and target ligands in a spatially defined manner. By this process, precise control of size, composition, and multifunctionality of the gene-delivery system is possible (Figure 2.52). ^[113]

2.4.1.2 Detection of Cancer with Gold Nanocages

Gold/silver nanocages can be used to detect human cancer. By using chloride-mediated polyol synthesis in particular, large quantities of nanocubes of 20-30 nm in dimension

can be produced at high yields. These small cubes are then converted into Au/Ag hollow nanostructures, correspondingly their SPR peak shifts from the visible to the near-infrared (Figure 2.52); specifically to the ~800 nm wavelength that can be employed in optical coherence tomography (OCT). OCT is an efficient technique to noninvasively obtain image with biological features on the micrometer scale, which makes gold or silver promising candidates for the early detection of cancer.

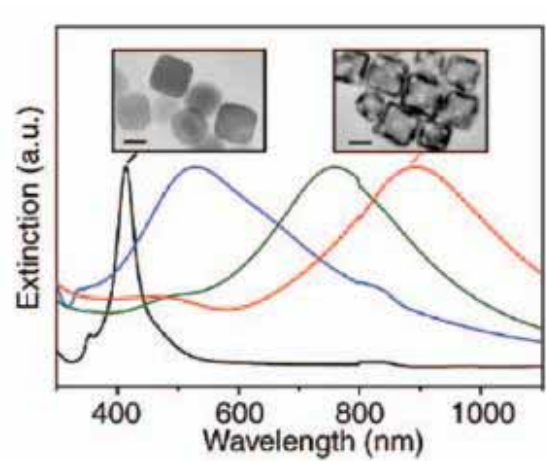


Figure 2.52 Transformation of 30 nm Ag nanocubes into Au/Ag alloyed nanoboxes and nanocages results in a continuous shift of their surface plasmon resonance (SPR) peak from 400 to 900 nm, which is in the transparent window of biological tissue. The SPR peak position is determined by the molar ratio between HAuCl_4 and Ag involved in the replacement reaction. Insets show TEM images of the cubes and cages; scale bar in each Figure 2.52 represents 20 nm. ^[113]

To detect cancer at an early and treatable stage using OCT, the contrast (difference in optical properties) between the tumor and surrounding healthy tissues must be enhanced. Gold nanocages can be employed as a contrast agent. Wiley et al. ^[114] reported that they could functionalize gold nanocages with tumor-specific antibodies through thiol-based conjugation. ^[113] Moreover, these antibodies enabled Au nanocages can specifically attach to tumor cells, making the contrast between tumor cells and the healthy tissue greater during OCT imaging. Notably, the relatively small size of the nanocages will enhance their biocompatibility and mobility within biological tissues. ^[113]

2.4.2. Sensing Application

Gold and silver nanoparticles can be used in sensing application. The sensitive response of surface plasma resonance (SPR) peaks to environmental changes can be exploited to optically detect and monitor binding events on the gold or silver surface. One typical example in this connection is based on the excitation of propagating SPR in a metallic thin film deposited on a transparent substrate. ^[115]

The localized SPR of gold or silver colloids have been widely explored for optical sensing in two different configurations. The first one involves the use of individual nanoparticles. Based on the scattering theory, any variation in the refractive index of the surface layer leads to changes in the intensity and/or position for the localized surface plasma (LSP) peak, as well as the increase in the refractive index often causes the LSP peak shifts to short wavelengths. And the second one relies on the red-shift of the peak caused by the aggregation of gold or silver particles due to the coupling between their LSP modes. The difference from the first configuration is that the attendance of an analyte can be visually sensed by naked eye. This is applicable to detect DNA and single-base mismatches in DNA hybridization, as well as to probe the protein occurrence for immunoassays. ^[115]

2.4.3 Wave-Guiding Materials

Xia, et al. reported that silver and gold nanoparticles could be useful in nanoscale wave-guiding. They also found that there is no significant loss of the flow of electromagnetic energy over distances of hundreds of nanometers in a linear chain of gold or silver channel. However, the nanoparticles are required to separate with gaps quite narrow (<1 nm) to permit near-field coupling of the SPR band modes with individual nanoparticles. ^[115] The fabrication of nanoscale optical waveguides was achieved by taking advantage of the SPR coupling between adjacent metallic nanostructures. A number of methods have been developed to fabricate plasmonic waveguides with a spatial confinement well under the limit of diffraction <100 nm, including e-beam lithography, high energy ion irradiation, and self-assembly. In particular, e-beam writing generates ordered arrays of metallic nanoparticles with well-controlled dimensions and spatial separations. However,

the development of this technique to a practical use in large scale of nanostructures at minimum cost is still challenging. ^[115]

2.4.4 Catalysis

The better catalyst/support structure is one that has a high surface area along with a uniform distribution of catalyst nanoparticles throughout the support structure. ^[107] Different shapes are applicable to catalyze different reactions. Gold nanoplates that were made via electrochemical method can be useful for producing such catalysts. ^[116] The porous support material in which the nanoparticles can concurrently take place in a spatially fix template are also applicable to be a catalyst. Moreover, the inorganic nanoparticle-mesopore composites are likely to allow three dimensional designer catalysts with separately tuning the microscopic catalytic rates on the nanoparticles surfaces in addition to controlling over material transport by changes in the pore size. ^[116] Generally, these catalysts can be classed into two main groups, i.e., homogenous ^[117] and heterogenous catalysis. ^[118]

2.4.4.1 Homogenous Catalysts

In a colloidal solution, transition metal nanoparticles can be used as catalysts. However, it is necessary to stabilize the colloidal nanoparticles beforehand, to avoid possible aggregation and to be potential recyclable catalysts. The better the capping of the nanoparticles, the more stable these particles in the solution, but the problem is that. The catalytic activity becomes lower as the active surface sites are better protected. There are several common reactions of nanoparticles in colloidal solution, ^[117] including:

- i. **Suzuki cross-coupling reaction**, it is a C-C bond formation reaction that couples arylboronic acids and aryl halides to form biaryls, in which the often used metallic catalysts including palladium, ruthenium, copper, and bimetallic nanoparticles.
- ii. **Heck cross-coupling reaction**, it is a C-C bond formation reaction that occurs between alkenes and aryl halides, in which the common used metallic catalysts including palladium, ruthenium, and trimetallic gold-silver-palladium nanoparticles.

- iii. **Electron-transfer reaction**, have been catalyzed using transition metal nanoparticles in solution, such as platinum nanoparticles with different morphologies like spherical, tetrahedral and cubic shapes.
- iv. **Hydrogenation**, is the most common reaction that has been carried out using transition metal nanoparticles in colloid solution e.g. Pd nanoparticles were used as catalyst for hydrogenation of dehydrolinalool to form linalool.
- v. **Oxidation**, catalyzed by transition metal nanoparticles such as palladium nanoparticles in water/AOT/heptane microemulsions, to catalyze N, N-dimethyl-p-phenylenediamine (DMPPD) and N, N, N', N'-tetramethyl-p-phenylenediamine (TMPPD).

2.4.4.2 Heterogeneous Catalysts

Such cases normally take place in the transition metal nanoparticles that are supported on various substrates. Various methods have been used to prepare the heterogenous nanocatalysts, including: ^[16, 107, 117, 118]

- Adsorption of the nanoparticles onto supports
- Grafting of the nanoparticles onto supports
- Fabrication of nanoparticles onto supports by lithographic techniques

Alumina, titanium, gold, palladium, and platinum are the typical metal nanoparticles commonly used, and they are grafted onto oxide supports for different applications. Several reactions have been catalyzed by metal/oxide nanoparticles, including:

- i. **Fuel cell**, e.g. methanol oxidation can be achieved on the oxide supported platinum and platinum-ruthenium nanoparticles.
- ii. **Catalytic oxidation**, e.g. gold/titanium dioxide can be used many gas oxidation and reduction reactions (CO, H₂, CH₄, NO_x).
- iii. **Hydrogenation**, e.g. hydrogenation of benzene, cinnamaldehyde, N-heterocycles, arenas, crotonaldehyde, ethylene, and olefins is catalyzed using supported transition metal nanocatalysts.
- iv. **Reduction reactions**, e.g. the supported transition metals have been used to catalytic decomposition of methane, and reduction of SO₂ and NO.

2.5 Conclusions

In this chapter, the properties of metal particles, including the optical absorption, the effect of aspect ratio, refractive index, a shell layer and nonradiative relaxation in metal nanostructures systems have been described. Subsequently, wide ranges of synthesis methods, from physical up to chemical techniques have been discussed. However, these previous techniques have obtained some success yet some limitations such as the use of toxic reagents that are harmful to the environment, critical experimental conditions that are hard to operate, e.g., high temperature, gamma-irradiation, photochemical with specifically selected wavelengths of light or laser. The growth mechanisms of the nanoparticles have been explained but most of them relied on the experimental observations, and lack of theoretical understanding at this stage. The selection of stabilizers or surfactants is still very empirical. To develop more powerful simulation method to fundamentally understand the particle growth mechanism is still a challenging task.

The aim of this project is to develop novel synthesis techniques to produce nanoparticles that can be used to control particle shape and size readily and conducted under ambient conditions. Moreover, the theoretical methods including density function theory (DFT) and molecular dynamic (MD)) simulations will be used to understand the fundamentals of particle growth at a molecular scale, facilitated by advanced experimental techniques.

CHAPTER 3

Experimental Work

3. 1 Gold Nanostructure Synthesis

3.1.1 Chemicals

The major chemicals including hydrochloroauric acid ($\text{HAuCl}_4 \cdot 3\text{H}_2\text{O}$, 99.9%), sodium citrate (99.5%) and poly(vinyl pyrrolidone) (PVP, 99%, with mean molecular weight 55,000), were purchased from Sigma-Aldrich and used as received. The sodium salts (e.g., NaF, NaCl, NaBr, NaI, and Na_2S) and thiols (e.g., C_{12}SH) were also purchased from Sigma-Aldrich used as received. All the solutions were freshly prepared for the synthesis of gold nanoparticles with Milli-Q water. All glassware was cleaned with aqua regia, thoroughly rinsed with Milli-Q water, and dried prior to use.

3.1.2 Synthesis of worm-like gold nanoparticles

To optimize experimental conditions such as concentrations, reaction time and temperature, many tests have been carried out. In a typical procedure, three steps were involved. First, the solution containing HAuCl_4 and PVP was mixed in a vial and the total volume is fixed to 20 ml, in which the final concentration was fixed at 2.5×10^{-4} M and 2.0×10^{-3} M for HAuCl_4 and PVP, respectively. Second, the mixture was pre-heated at 50°C for 30 min with vigorous stirring, and the light yellow color of the solution remained as it was. Heating and stirring were kept constant during this step. Third, the vial containing the preheated solution was placed into boiling water for reflux heating at 95°C . After ~5 minutes, an appropriate amount of sodium citrate solution (the molar ratio of citrate to AuCl_4^- ions is 3) was added into the preheated mixture, followed by continuously reflux heating. Upon the addition of sodium citrate, the reaction solution turned from bright yellow to ruby red and finally dark purple.

3.1.3 Sensing detection of anions

Many tests have been conducted for optimizing the sensing detection of inorganic anions, such as addition time, concentration, and stirring rate. Briefly, two steps were involved in

our case. First, an appropriate amount of Na₂S solution (0.01 M) was added into 10 ml solution containing worm-like gold nanoparticles, followed by vigorous stirring to ensure that the mixture is homogeneous. Second, 3 ml of the mixed solution was taken for measuring the optical absorption by UV-vis spectrum. The other measurements involved in the various inorganic anions (e.g., F⁻, Cl⁻, Br⁻, and I⁻) were carried out by following the similar procedures as detecting S²⁻ ions. Note that the PVP molecules were not removed to avoid aggregation in the whole sensing process. All procedures were carried out at room temperature (ca. 25 °C).

3.1.4 Density Function Theory (DFT) simulations

The binding energies (BE) between PVP and gold crystal surfaces (i.e., 110, 100, and 111) were calculated based on DFT using DMol3. The geometry optimization and energy calculation steps were performed using the Generalized Gradient Approximation scheme with the Perdew Burke and Ernzerhof (PBE) exchange-correlation functional. A DNP (Double Numerical extra polarization) basis set that accounts for polarization functions was used with Effective Core Potentials (ECP) used as the pseudopotential.

The tolerances for energy, gradient, and displacement convergence for geometry optimization are 2×10^{-3} Ha/Å, 1×10^{-5} Ha and 0.005 Å, respectively. The model was simulated as periodic super cell with at least 10.0 Å of vacuum gap between the upper most portions of the model with the top of the simulations cell. The Brillouin zone integration was performed using a (5×5×1) Monkhorst-Pack grid.

3.2 Silver Nanoplate Synthesis

3.2.1 Chemicals

Silver nitrate (AgNO₃, 99.9%), citrate acid (99%), Lascorbic acid (~99.0%), sodium borohydride (NaBH₄, 99%), sodium bis(2-ethylhexyl) sulfosuccinate (NaAOT, 99%), and HAuCl₄ • 3H₂O (99.9%) were all purchased from Sigma- Aldrich, and used as received without further treatment. All the solutions were freshly made for the synthesis of silver nanoparticles; in particular, the freshly made NaBH₄ aqueous solution was ice bathed before use. Ultra-pure water was used in all the synthesis processes.

3.2.2 Synthesis of silver nanoplates

In a typical procedure, three steps were carried out as follows. First, 3.125 ml aqueous AgNO_3 (0.02 M) and 6.25 ml NaAOT (0.02 M) solution were added to a 500 ml conical flask with ultra-pure water and then stirred for 10 min at room temperature; the final volume of mixture was fixed as 250 ml, and the concentrations of AgNO_3 and NaAOT were 2.5×10^{-4} and 5.0×10^{-4} M respectively. Second, 0.75 ml citrate acid (0.10 M) and 0.625 ml L-ascorbic acid (0.10 M) aqueous solution were added to the 250 ml solution which was then stirred vigorously; finally, 0.05 ml NaBH_4 (0.002 M) aqueous solution was rapidly added into the above mixed solution which was then stirred for 30 s. The colour of the solution changed from light yellow to purple, pink, green, and blue with time. The blue solution contains the as-synthesized silver nanoplates with triangular shape.

3.2.3 Numerical method

Molecular dynamics (MD) simulation with the *NVT* ensemble was performed to understand the mechanisms of anisotropic growth of the silver nanoplates. All simulations were performed using the Discover Module of Materials Studio (*version 3.2, Accelrys Inc., 2005*). The interaction between surfactant AOT and three silver crystal planes (i.e. (111), (110) and (100)) was calculated. For each plane, the representative system consists of one silver crystalline plane and seven AOT molecules on the surface of silver. All the systems were subject to energy minimization for the structural optimization before MD simulation. All MD simulations lasted for 50 ps with the time-step of 1 fs. Data were collected in the last 20 ps for statistical and structural analysis.

3.3 Selenium Nanowire Synthesis

3.3.1 Chemicals

Silver nitrate (AgNO_3 , 99.9%), selenious acid (H_2SeO_3), citric acid (99%) and sodium bis(2-ethylhexyl) sulfosuccinate (NaAOT, 99%), all purchased from Sigma-Aldrich and pyrogallol (99%) from Fluke, were used as received. All the solutions were freshly made for the synthesis of silver nanoparticles. Milli-Q water was used in all the synthetic processes.

3.3.2 Synthesis of silver nanoparticles

In a 30-mL vial, 10 mL aqueous solution containing Ag^+ (2.5×10^{-4} M) and AOT (5.0×10^{-4} M) was stirred for 30 min, and then 60 μL pyrogallol (0.1 M) solution was added and stirred for 10 min. The color of the solution gradually changes to light yellow.

3.3.3 Synthesis of selenium nanowires

1 mL of the above-synthesized solution was centrifuged and the precipitate was rinsed two times with water. The precipitate was then re-dispersed in 5 mL aqueous solution before adding 0.1 mL selenious acid (0.1 M) and 0.1 mL citric acid (0.1 M). The mixture was stirred for 30 s and then kept at room temperature without disturbance. Over 2 days, the solution became light dark-red color.

3.4 Characterization

The morphology and composition of the final product were measured under Philips CM200 field emission gun transmission electron microscope (TEM) and energy dispersive X-ray spectroscopy (EDS), operated at the accelerated voltage of 200 kV. The specimen was prepared by dropping the solution onto the Formvar-coated copper grid and dried in air naturally. Ultraviolet–visible (UV–vis) absorption spectrum was obtained on a CARY 5G UV–visible Spectrophotometer (Varian) with a 1-cm quartz cell. The composition of as-synthesized sample was confirmed by X-ray diffraction (XRD) pattern recorded using Siemens D5000 at a scanning rate of $0.5^\circ \text{ min}^{-1}$ in the 2θ range of 30–85°.

For Gold Nanoparticles. The data for particle size distribution was collected automatically by using Image Processing and Analysis in Java Program. The number of particles was counted is over 1,000 particles.

For Silver Nanoplates. The diameter and thickness of the nanodiscs were measured using a Digital Instruments 3000 atomic force microscope.

CHAPTER 4

Results and Discussion

4.1 Au Nanostructures

4.1.1 Shape/Size Worm-like gold nanoparticles

The microstructure of worm-like gold nanoparticles was characterized by TEM technique. Before injecting citrate ions and reflux heating at 95 °C, the PVP-AuCl₄⁻ system was preheated at 50 °C for 30 minutes. From light yellow, the color of the solution turned to dark purple as shown from Figure 4.1 below. The aim is to separate the nucleation and growth stages as far as possible for shape/size control. A successful separation of nucleation and growth plays a key role in determining the crystal shape and size,²⁰ As seen from TEM images shown in Figure 4.2A, the particles are composed of ~65% spherical shape (~10 nm in diameter), ~30% ellipsoid, and ~3% worm-like particles, together with some small gold dots (1-2 nm in diameter) after reflux heating at 95 °C for 10 min. ^[2]

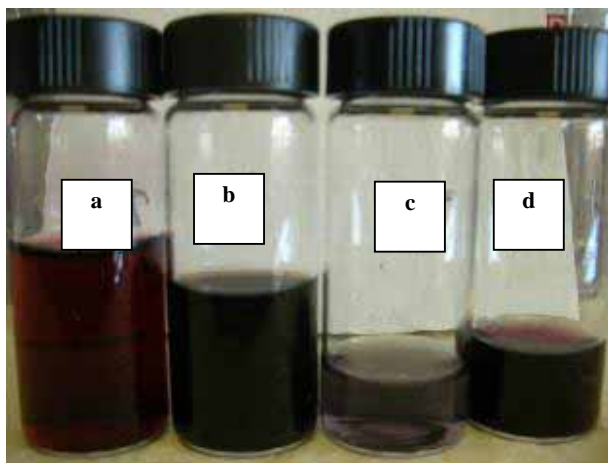


Figure 4.1 Typical solution colors of the wormlike Au nanoparticles.

A twenty-minute difference in reflux heating results in a distinct change in particle morphology. This can be seen from Figure 4.2B that over 50% spherical particles grew bigger to rod-like nanoparticles (~60 nm in length and ~20 nm in diameter), along with some spherical particles. As the reflux heating was extended up to 45 min or 60 min,

almost all the particles grew longer (Figure 4.2C and D). The worm-like particles are shaped as English characters like 'L', 'W', and 'S'. The crystallization of these nanoparticles was further identified by the selected area electron-diffraction (SAED) pattern shown in the inset of Figure 4.2D. Those electron diffraction rings could be assigned to (111), (200), (220), (311), and (222) planes of the fcc Au, respectively. Based on the above TEM analysis, the growth of the crystal worm-like nanoparticles is presented as a function of the reflux heating time in aqueous media.^[2]

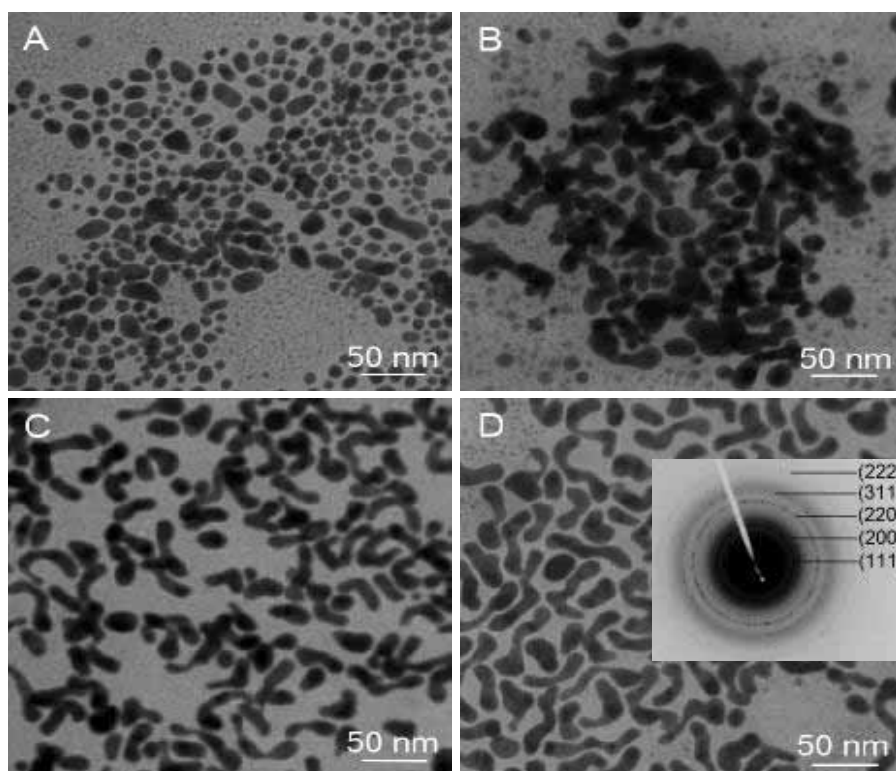


Figure 4.2 TEM images of gold worm-like nanoparticles prepared at 50 °C with different reflux heating times at 95 °C: (A) 10 min; (B) 30 min; (C) 45 min; and (D) 60 min. The inset of Figure 4.2D is showing the corresponding electron diffraction pattern of nanoparticles.^[2]

These worm-like morphologies are related to their atomic arrangement. High-resolution TEM was conducted to check the crystallization orientation of gold nanoparticles (Figure 4.3). The high-resolution TEM images show that the particles are single crystalline structure (Figure 4.3B and C), and the lattice planes continuously extended to the whole particles with one or more twin boundaries. Closer inspection of the individual

nanoparticles reveals that the single crystalline particles have an interplanar distance of ~ 0.285 nm, corresponding to Au{110} planes. The TEM investigation indicates that the particle oriented along the [110] direction as marked by arrowheads in Figure 4.3B and C. This is consistent with previous studies on the growth of gold nanorods. ^[119] Wang et al. ^[119] reported the single crystal gold nanorods oriented along [110] direction.

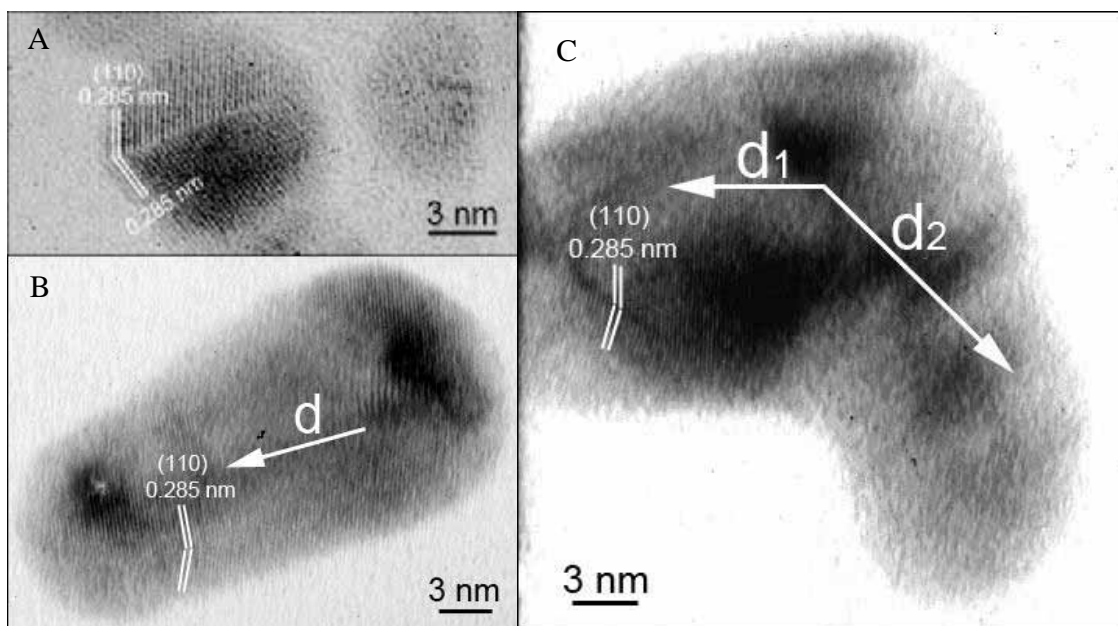


Figure 4.3 (A) HRTEM image of gold worm-like nanoparticles; (B) HRTEM image of a short nanorod; and (C) an L-shaped gold particle, along with the interplanar distance around 0.285 nm. ^[2]

They also described that the faces enclosing the nanorods were identified with the dominant sides being {110} planes and with the growth direction being [001], while the ends of the nanorods are terminated by the {111} planes with smaller areas. In this case, both the rod-like and the L-shaped particles were all identified with dominant sides being Au {110} planes. Detailed analysis of the TEM image (Figure 4.3B) reveals that the starting end of the particle is a slightly wider (ca. 5 nm) than the terminating end that looks like a needle due to the possible surface defects. In consideration of these observations, the body of the worm-like structures differs from the gold nanorods with uniform diameter along the length obtained by using CTAB. ^[16, 33, 120-126] The previous study revealed that the high-concentration CTAB molecules (~ 0.1 M) could form a

double-layer template to restrain the particle growth. [121, 122] Additionally, the crystallization orientation of the worm-like particles seems also different from those gold tripods or tetrapods obtained in CTAB solution. [127]

Those branched gold nanostructures are single crystal and oriented along {111} planes with different growth directions such as [110], [128], [-101] and [01-1] in the tetrapods. The experimental results indicate that the surfactants indeed play a key role in the shape control of gold nanoparticles.

4.1.2 Optical Properties

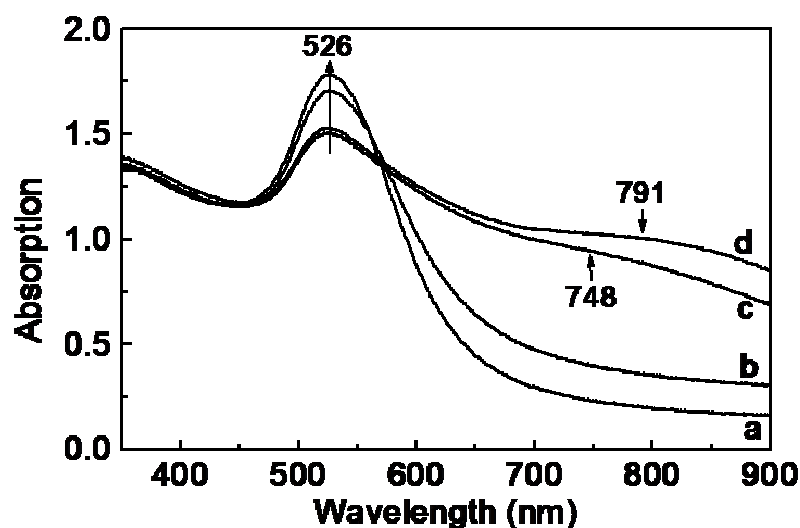


Figure 4.4 UV-vis spectra of the samples corresponding to different reflux heating times: (a) 10 min; (b) 30 min; (c) 45 min; and (d) 60 min. [2]

To trace the particle growth, the optical absorption of gold nanostructures was measured and shown in Figure 4.4. It was seen that the absorption intensity of the four investigated samples decreased a little at the peak ($\lambda_{\max}=526$ nm) but the curve tail progressively increased beyond 620 nm with reflux heating time increasing. For a short refluxing time (10 min), only a single plasma band centered at $\lambda_{\max}=526$ nm was observed (curve a), indicating that the spherical particles are the dominant morphology. This is consistent with our TEM observations (Figure 4.2A). As the reflux heating time increased, a second peak centered at around $\lambda_{\max}=748$ nm (curve c) or $\lambda_{\max}=791$ nm (curve d) was observed

corresponding to 45 min or 60 min, respectively. In analyzing the optical properties, we have tried to assign the second plasma band to the distribution of particle aggregation or to the worm-like particles themselves. ^[2]

However, the transparent dispersion and the well-dispersed particles on TEM image (Figure 4.2D) ensured us that the second surface plasmon resonance was originated from the worm-like particles themselves rather than from the particle aggregation. It was noted that the absorption intensity in the longitudinal surface plasma ranging from 700 to 800 nm is relatively weaker than those obtained from the gold nanorods with uniform diameter. ^[16, 33, 120, 126] This is due to the worm-like shape of particles and/or the wide size distribution (Figure 4.2C and D).

4.1.3 Effects of experimental parameters

4.1.3.1 Reaction temperatures

The mixture containing PVP and AuCl_4^- ions was separately preheated at 40, 60, and 70°C for 30 min before further reflux heating. Low (<30 °C) or high (>80 °C) preheating was not considered for comparing with the samples obtained at 50 °C. After 30-min preheating, it was noted that the solution color turned light yellow. All the three samples stored in the vials were placed into 95 °C water by following vigorous stirring. After ~5 min, an appropriate amount of citrate ions (the molar ratio of citrate ions to AuCl_4^- is 3) was separately injected into each vial. The color of the solution turned purple from light yellow about 1 min later. ^[2]

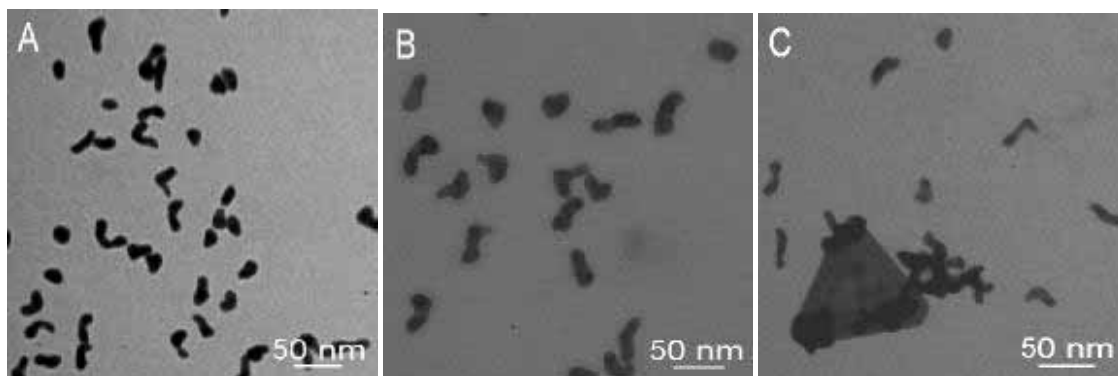


Figure 4.5 TEM images of gold nanoparticles prepared under the same preheating time (30 min) but different preheating temperatures: (A) 40 °C; (B) 60 °C; and (C) 70 °C.

As reflux heating at 95 °C went on longer (e.g., 60 min), the color of the solution turned darker purple finally (Figure 4.1). The corresponded TEM analysis indicates that the as-prepared particles are composed of ellipse (~20%) and worm-like shape (~80%) as it was preheated at 40°C (Figure 4.5A). With increasing the preheat temperatures, most of the particles grew into worm-like shape as shown in Figure 4.5B and C, although the size is slightly different. The TEM images suggest that the preheating temperature (40-70 °C) has a small influence on the morphology of the final products.^[2]

In comparison to the above procedures, 4 vials containing PVP-Au solutions were firstly preheated at 50 °C, and then all were immersed in cold water (~5 °C). This aims to examine the impact of the low temperature on the shape/size of final products. After bathed in cold water for ~3 h, the 4 samples preheated with different time (i.e., 10, 30, 45 and 60 min) were placed into hot water for reflux heating at 95 °C with vigorous stirring. About 10 min, an appropriate amount of citrate solution (the molar ratio of citrate ions to AuCl_4^- is 3) was added into each vial. The light yellow color of reaction systems gradually turned ruby after 60-min reflux heating. See Figure 4.6 below.^[2]

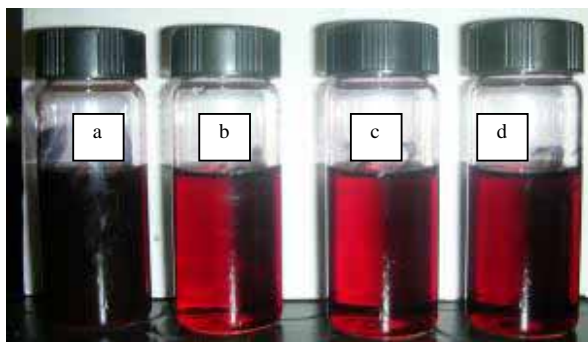


Figure 4.6 Solution color after 60 minutes refluxing time at 95 °C but at different preheating time, a. 10, b. 30, c. 45 and d. 60 min

As seen from TEM images shown in Figure 4.7, almost all the particles are spherical shape except that a very few ellipse-like particles were observed in the sample with 60-min reflux heating (Figure 4.7D). Unfortunately, no worm-like nanoparticles were

observed in all these 4 samples. A possible reason is that the surface activity of gold atoms is greatly reduced in cold water. Thus, it may hinder the potential for Au surface modifications to form worm-like structures as expected. Despite this outcome, it was found that the low-temperature post-treatment could be useful for the synthesis of spherical particles with uniform size.

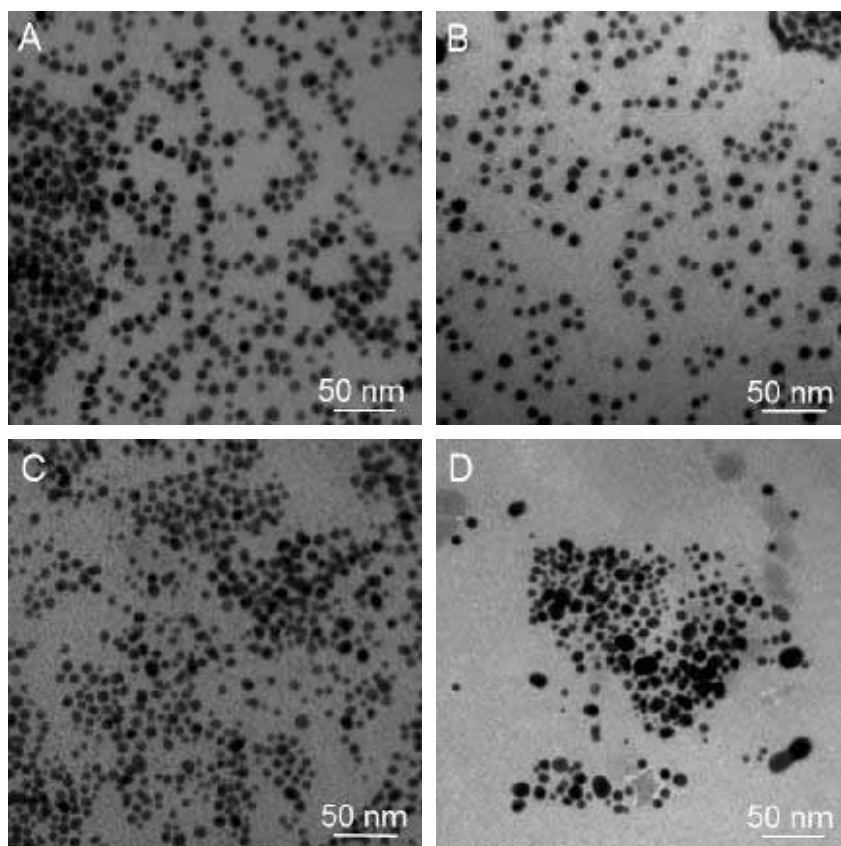


Figure 4.7 TEM images of gold nanoparticles prepared by preheating at 50 °C for different times: (A) 10 min; (B) 30 min; (C) 45 min; and (D) 60 min, following by immersing into cold water (~5 °C) for comparing the effect of temperature on the seed and hence the final morphology of products. ^[2]

Further evidence of the effect on particle shape/size by low-temperature bath could be seen from their corresponding size distributions shown in Figure 4.8 (AA-DD). Those gold nanoparticles are almost spherical shape and the average sizes are measured as ~9.8 nm (AA), ~8.1 nm (BB), ~7.9 nm (CC), and ~13.6 nm (DD) as indicated by the table below.

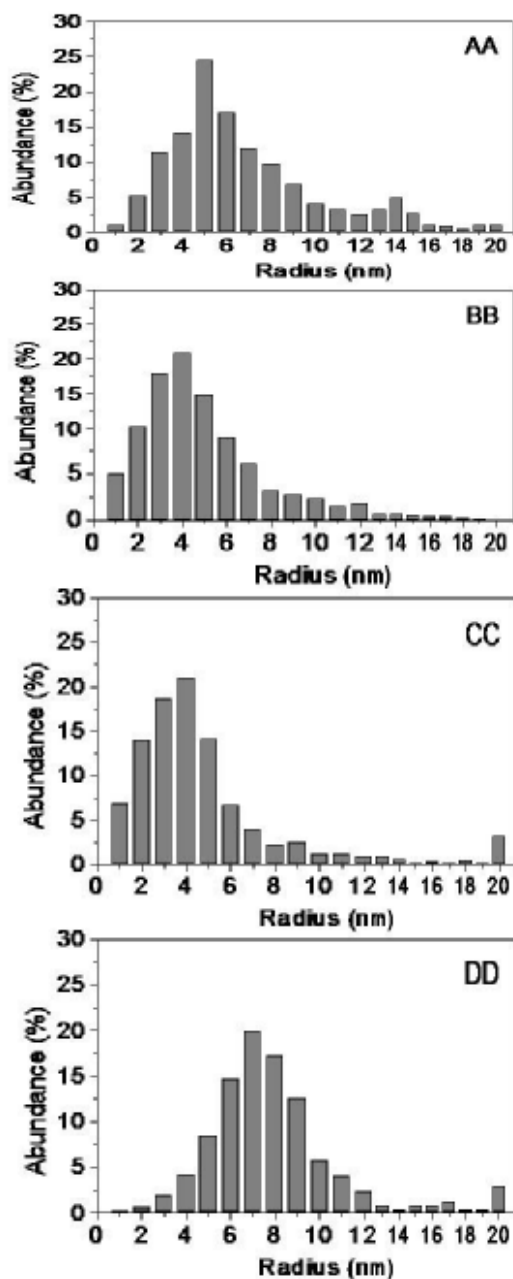


Figure 4.8 Size distribution of different samples preheated at different time (AA) 10 min; (BB) 30 min; (CC) 45 min; and (DD) 60 min

4.1.3.2 Surfactants of AOT and CTAB

In comparison with PVP, two surfactants were tested to shape control including bis(2-ethylhexyl) sulfosuccinate (AOT) and CTAB. Both of them are always employed in

This table was obtained by using software called ImageJ. The size over 20 nm could be assigned to the attachment of two or more particles as shown in Figure 4.8 CC and DD.

Unfortunately, there are no worm-like particles formed in such systems even if they were reflux heated for 60 minutes. This fact is also supported by the corresponding optical absorption shown in the UV-vis spectra (Figure 4.9). Only one single plasma band centered at ~525 nm was observed and no rise occurred in the curve tail beyond 620 nm.

A slight difference in the UV-Vis spectra is due to the small difference in size distributions. From the above analysis, the preheating or post-treatment temperature played a key role in the shape/size control.

shape control of nanoparticles, particularly for metal (e.g., Au and Ag). In previous studies, the AOT molecules were used for making truncated silver nanodiscs in isooctane by forming reverse micelles.^[129] The CTAB molecules were used for preparing truncated silver triangles,^[130-132] gold nanorods or nanowires.^[121-124] In this case, all the experimental conditions were kept the same as using PVP. After preheated at 50 °C for 30 min, there was no color change in both the AOT-AuCl₄⁻ and the CTAB-AuCl₄⁻ solutions, indicating that both AOT and CTAB have no the ability to reduce AuCl₄⁻ ions to gold atoms under current conditions.

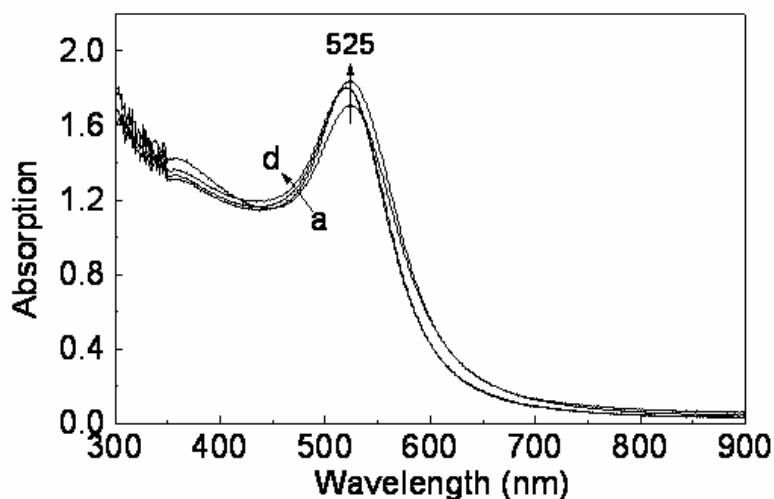


Figure 4.9 UV-vis spectra of the 4 samples shown in Figure 4.7 indicating they have the similar optical absorption profile.

Subsequently, the vials containing the preheated samples were put into hot water with vigorous stirring for ~10 min, an appropriate amount of citrate ions (the molar ratio of citrate ions to Au is 3) was quickly injected into each vial. The solution color turned purple with the reflux heating continuing, revealing that there are more metal gold atoms formed and/or the small gold dots grew into bigger.

The morphology of the gold particles was further characterized by TEM technique. Figure 4.10A shows that the gold particles aggregated together when we used AOT

molecules. It seems that all the particles link together and it is difficult to identify the shape and the accurate size.

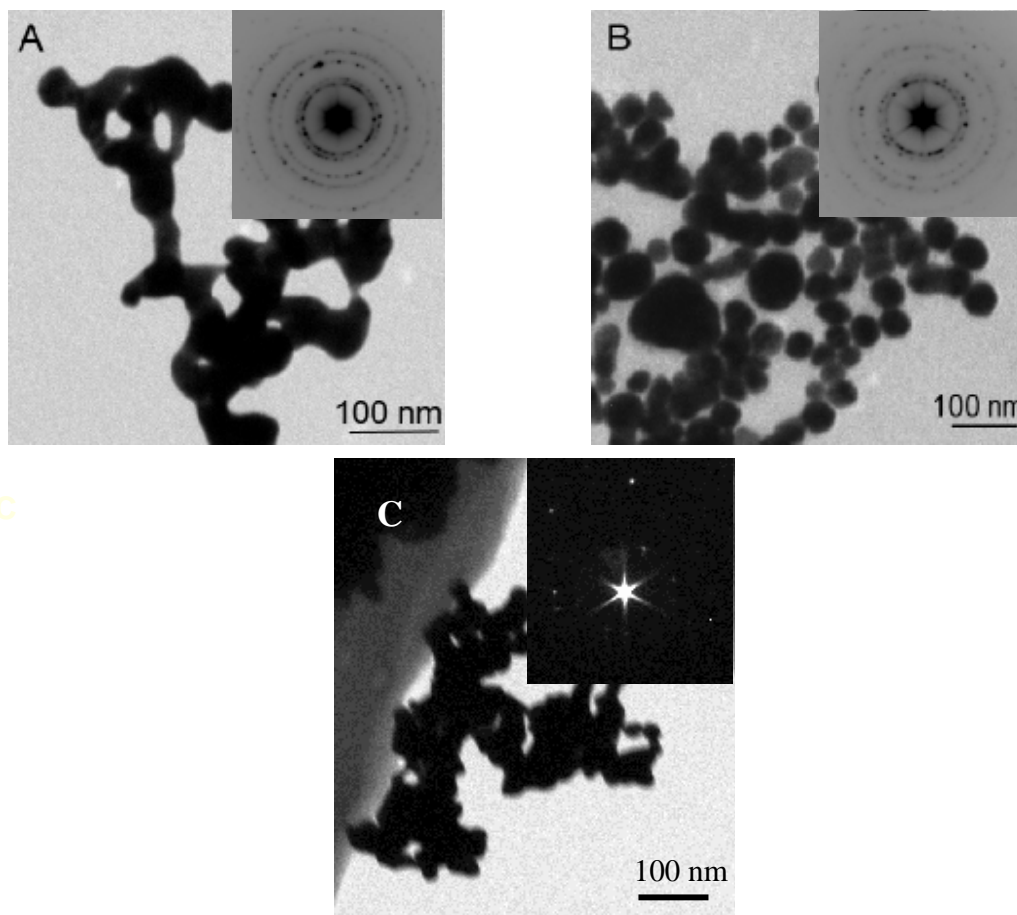


Figure 4.10 TEM images of Au nanoparticles prepared by using different types of surfactants: (A) AOT; (B) CTAB and (C) SDSN. The electron-diffraction pattern (inset of Figure 4.10A, B and C) confirming that the particles are crystalline.

This is different from our previous observations on the control synthesis of silver nanodiscs, where the AOT molecules preferred to adsorb on Ag{111} planes but not {110} and {100} planes, and hence plate-like silver nanoparticles were prepared. The second surfactant (CTAB) appeared to be better than AOT in shape control of gold nanoparticles under current conditions, although the diverse morphologies were still observed (Figure 4.10B). And the last surfactant tested was SDSN. The product appeared in irregular shape and aggregated. Nevertheless, the nanoparticles prepared by using the

two surfactants are crystalline structure based on the electron diffraction rings (inset of Figure 4.10A, B and C). From the TEM analysis, different surfactants have different capabilities in shape and size control, and PVP is suitable for preparing worm-like particles in this work.

4.1.3.3 PVP-AuCl₄⁻ and citrate-AuCl₄⁻ systems

Two reaction systems, i.e., PVP-AuCl₄⁻ and citrate-AuCl₄⁻, were examined for fundamentally understanding the effect of the nucleation and growth in this case. In the first system, 3 vials containing PVP-AuCl₄⁻ solution were preheated at 50 °C for 10, 30, and 60 min, respectively. Figure 4.11A shows the TEM image of the sample that was preheated for 60 min. The particles are very small (~2 nm in diameter) but they are still crystalline structure identified by the electron diffraction pattern (inset of Figure 4.11A). The corresponding optical absorption was recorded and shown in Figure 4.11C. To observe the plasma band clearly, one enlarged part of the 3 curves was shown in the inset of Figure 4.11C, in which only one single plasma band centred at ~541 nm was observed. Further inspection of the UV-Vis spectra (curve a-c) shows that the absorption intensity increased slightly as a function of preheated time, indicative of more gold particles formed with longer preheating.

Different from the first system, the citrate-AuCl₄⁻ solution turned ruby red when it was preheated at 50 °C for 60 min. The microstructure of the particles was further checked by using TEM technique. Figure 4.11B shows that the particles are spherical shape with average size ~25 nm in diameter. The diffraction rings in the electron diffraction pattern (inset of Figure 4.11B) reveals that they crystallized well. The absorption intensity is stronger than those obtained from the PVP-Au system under the same AuCl₄⁻ concentration (Figure 4.11D). This reveals that there are bigger gold particles formed in the second system under the similar conditions. Based on the above TEM and UV-vis spectra analysis, both PVP and citrate ions have the ability of reducing AuCl₄⁻ ions to Au atoms, albeit the capability of PVP is weak. The two systems might play different but important role in shape control of gold nanoparticles in this work.

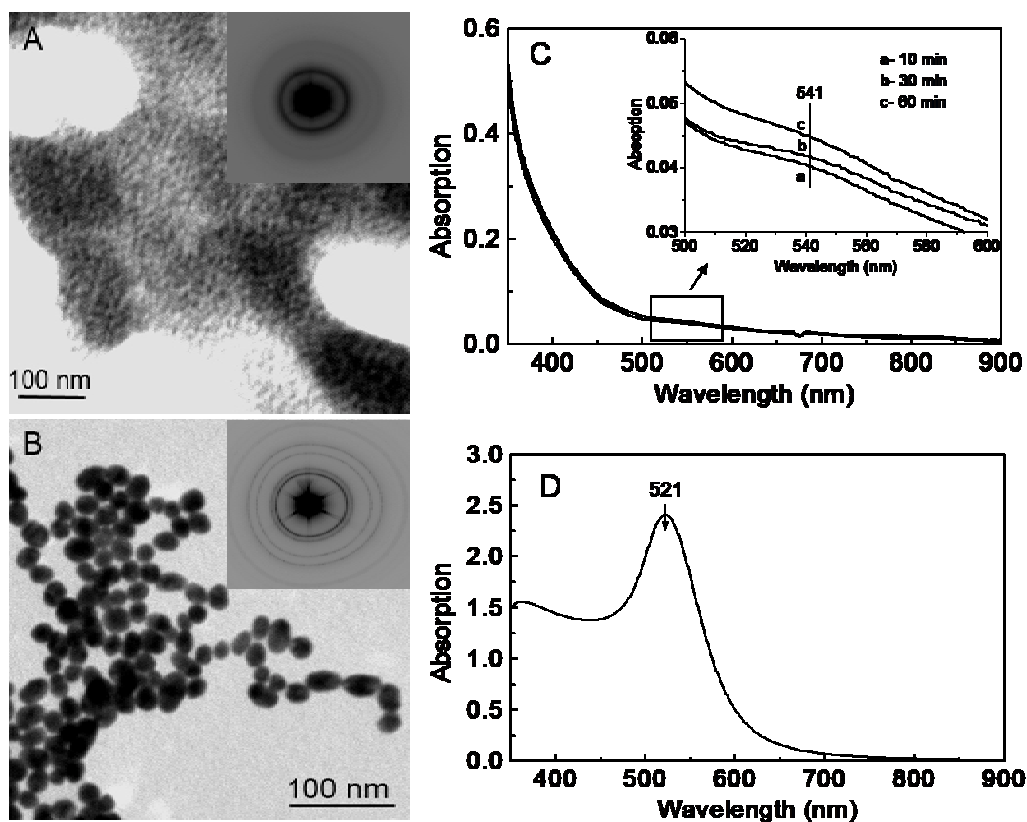


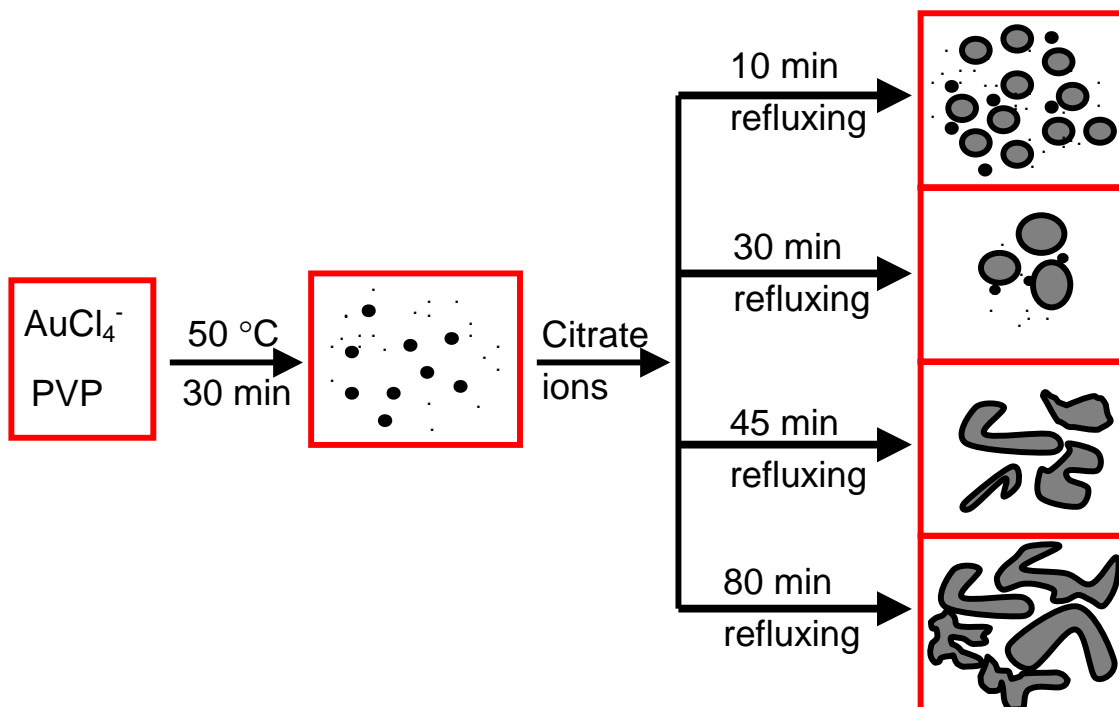
Figure 4.11 (A) TEM image of gold seeds obtained from the preheated PVP-AuCl₄⁻ solution at 50 °C for 60 min, and the inset showing the corresponding electron diffraction pattern; (B) TEM image of gold nanoparticles obtained from the preheated citrate-AuCl₄⁻ solution at 50 °C for 60 min, and the inset showing the corresponding electron diffraction pattern; and the corresponding UV-vis spectra shown in (C) and (D), respectively.

4.1.4 Particle growth mechanism

From the TEM and HRTEM analysis (Figures 4.2 and 4.3), the particles formed a worm-like structure with dominant sides being {110} planes. At the preheating stage, some AuCl₄⁻ ions could be partially reduced by PVP to form gold dots (Figure 4.11A). These gold dots were coated by PVP in solution, and they could provide nucleation sites for further growth when adding citrate ions into such a reaction mixture. At the reflux heating stage, the PVP molecules still adsorbed on the gold surfaces, although there was a

competition between the PVP adsorption and the orientated attachment. Scheme 4.1 below summarizes this growth mechanism.

Scheme 4.1 Schematic growth mechanism of Au worm-like nanostructure



Such an orientated attachment was seen in the formation of gold nanowires, in which the authors reported the orientated attachment of gold nanoparticles took place such that two {111} facets fused together to form a single particle.^[133] Such a fusion in {111} planes represents that there is a preferential removal of the capping molecules from these planes. Similarly, the orientated attachment for PVP coated gold crystals also took place on the fused {111} planes, although there are several ways in which this can be achieved. Only configurations that do not incur a significant interfacial energy penalty will be favored. The formation of a single crystal particle of reduced interfacial energy penalty induces the enhancement of Au structure stability. Thus, the growth of worm-like particles will be determined by the competition between the orientated attachment of the exposed nanoparticles along Au{111} planes and the rate of PVP adsorption from the solution. The similar removal/adsorption is also expected to occur on Au{100} planes. However, this surface will have two neighboring {110} faces with PVP adsorbed. As a result, the probability of {100} fusion will be reduced and the fusion of {111} planes for energy

reduction will be favored. This is consistent with the observations from HRTEM images (Figure 4.3B and C). Figure 4.12 shows a scheme illustrating the formation of worm-like nanoparticles through the fusion of Au {111} planes. Different reaction conditions would lead to different gold nanostructures as described by I-, II-, and III-type particles with different morphologies.

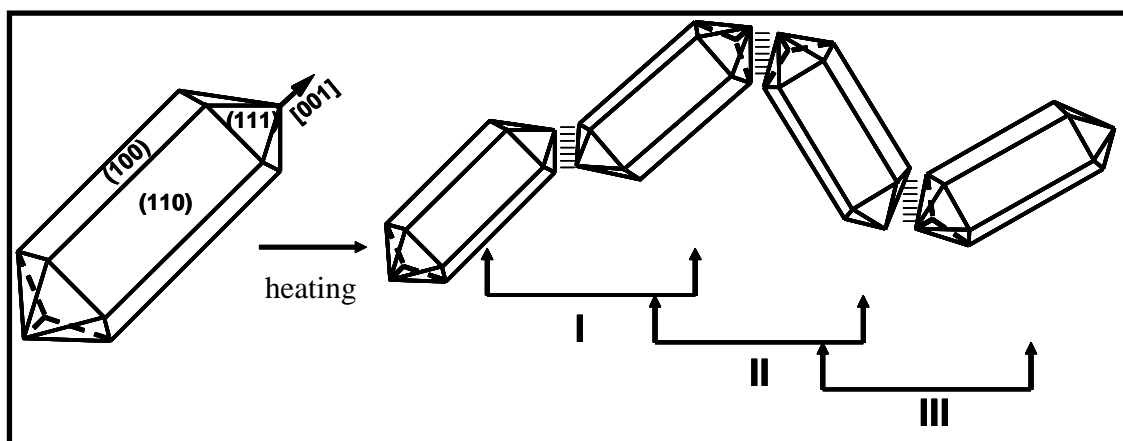


Figure 4.12 A scheme illustrating the formation of gold worm-like nanoparticles through the fusion along Au{111} planes with different lengths (e.g., I, II, and III).

To be more quantitative, DFT calculation was used to analyze the interaction energies of PVP with Au. The theoretical lattice parameter for Au was calculated to be 4.201 Å which is consistent with similar DFT calculations by Boon *et al.* [134-136] However, it is known from previous theoretical investigations that the Au lattice parameter calculated using Perdew-Wang like exchange-correlation functionalities are ~2.5% larger than the experimental lattice parameter of 4.08 Å. [137] Figure 4.13 shows the simulation model that PVP interacts with each gold crystalline plane (i.e., 111, 110, or 100). The preferential adsorption of PVP molecules on gold crystal planes is determined by the binding energies (BE).

Such BE is calculated by the following equation: $\Delta E_{BE} = E_{A-B} - (E_A + E_B)$, where E_{A-B} , E_A and E_B are the binding energies of gold plane with PVP (A-B), isolated gold plane (A) and isolated PVP (B), respectively. The BE between PVP and the gold crystallographic planes was calculated as {111} -0.0531 eV, {100} -0.0425 eV, and {110} 0.0197 eV, respectively. In principle, the higher the BE the stronger the adsorption strength. Thus,

the PVP adsorbed strongest on the Au{110} planes among the three, whilst on the Au{111} and Au{100} planes the PVP molecules are slightly repelled.

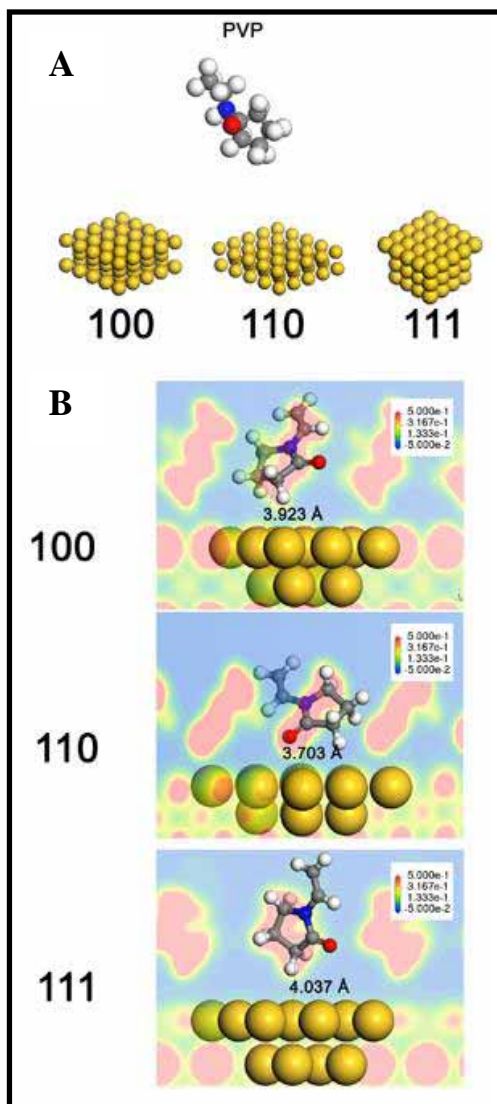


Figure 4.13 (A) The simulation model showing that PVP interacts with each gold crystalline plane (i.e., 111, or 110, or 100); and (B) the planar electron density profile of the PVP/Au system indicating the electrostatic interactions between PVP and Au. The atoms marked with different color as followings; Au (yellow), H (white), O (red), N (blue), and C (grey).

This could also be confirmed by the shorter distance between Au{110} and the closest carbon atom in PVP (3.703 Å) in comparison to 3.923 Å for Au{100} and 4.037 Å for Au{111}. The closest C atom to Au was chosen for the distance measurement because the C atom closest to Au resembles a pivot for PVP, and the electron density resides in the C, O and N atoms of PVP. From this knowledge, regions of high electron density will determine the spatial and geometric reconfigurations of the polymer backbone. On the contrary, H atom has a smaller atomic radius and has only one bond attached to it, thus it

has more degrees of freedom. This leads to the fact that if one was to define H as reference point for distance measurements, the result may not accurately represent the real environment.

Figure 4.13 shows the planar electron density profile of the PVP/Au system indicating the electrostatic interactions between PVP and Au. It can be seen from this plot that there is an electrostatic interaction region between PVP and Au with a tentative redistribution of electrons among this interface. As the BE for PVP adsorption on Au{111} and Au{100} suggests, there is repulsion a barrier at these interfaces. It can be thought that the repulsion effect may induce the formation of worm-like structures through the fusion of Au{111} planes as it is more energetically favorable. It is of importance to mention that PVP in aqueous environments reorganizes itself into a complex network of polymer backbones stabilized by electrostatic interactions. The irregular arrangement of polymers requires simulation models to be simplified. Thus, the PVP molecules are positioned so electrostatic interactions in the polymer backbone will be reflected throughout the periodic boundary cell. In light of this fact, we believe that the qualitative prediction of PVP BE trends to be correct. However, the magnitude of the BE may only reflect one particular arrangement of PVP on Au. Therefore, the BE of the PVP molecules on Au drives the formation of gold worm-like nanostructures. A distinct phenomenon differs from the usual formation of truncated octahedron for free clusters caused by the surface energies in bare gold. ^[138-140] Full details of the interaction between PVP and Au calculated by using DFT model is under progress.

4.1.5 Sensing detection of anions

Determination of common inorganic anions such as fluoride (F^-), chloride (Cl^-), and sulphide (S^{2-}) is significant in the characterization of the quality and extent of water. Surface-modified gold nanoparticles for sensing detection of inorganic cations (e.g., Li^+ , K^+ , Cu^{2+} , and Cd^{2+}) is successful yet has some limitations. ^[141, 142] In this work, the sensitivity using the as-prepared gold worm-like nanoparticles towards inorganic anions was investigated. The S^{2-} ions were separately added into 10-ml suspension containing gold worm-like particles, and the final concentration was fixed at 4, 8, 15, 30, and 60

ppm, respectively. The corresponding optical absorption was recorded to identify the sensitivity. As seen from the UV-vis spectra (Figure 4.14A), both the major surface plasma bands centered at 526 and 778 nm decreased in the intensity (ca. 0.43) with increasing S^{2-} concentration from 4 to 60 ppm. In the meantime, the peak position red shifted to 538 and 835 nm, respectively. Conversely, there is only a slight change in the surface plasma band of gold spheres (Figure 4.14B) and the absorption intensity decreased only ~ 0.1 under similar conditions. This indicates that the worm-like nanostructures are superior to the gold spheres in sensing detection of sulfide ions. In addition they are sensitive to sulfide ions rather than fluoride, chloride, bromide and iodide ions as confirmed by the UV-spectra (Figure 4.14C)

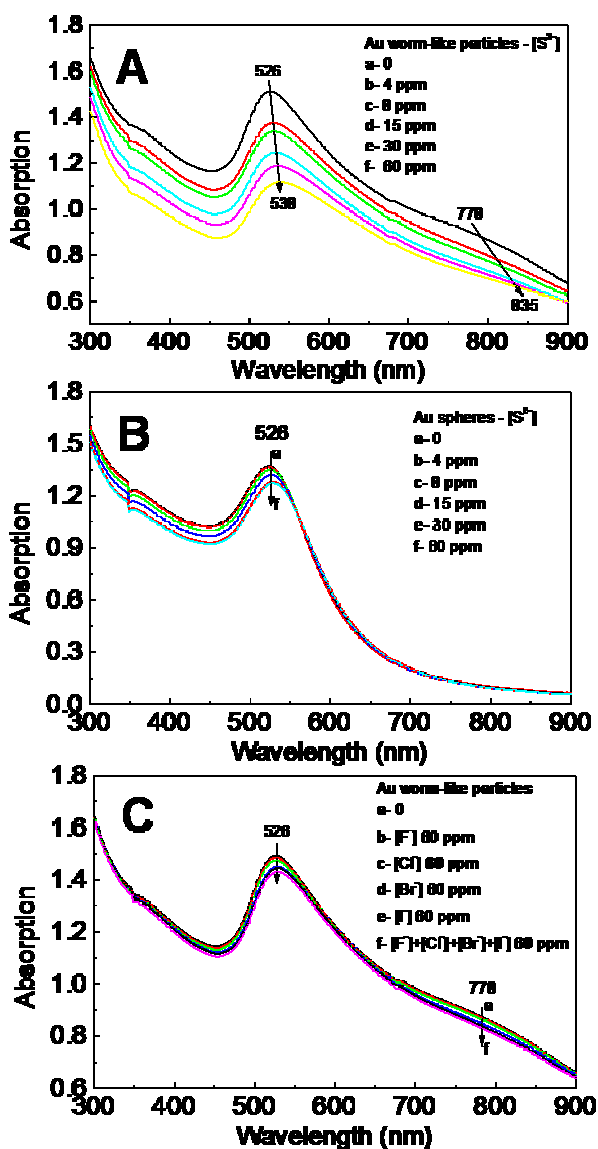


Figure 4.14 The sensing detection of anions examined by UV-vis spectra: (A), the sensitivity of Au worm-like particles towards sulfide ions with different contents; (B), the sensitivity of Au spheres towards sulfide ions with different contents; and (C), the UV-vis spectra showing that the gold worm-like nanoparticles can selectively sense sulfide ions rather than fluoride, chloride, bromide and iodide ions.

Considering the sensing mechanism, the surface plasma modes of small metal particles are sensitive to various perturbations including refractive index changes to the surrounding media, and surface electron charging.^[143] Electron injection into the metal particle can alter the metal plasma frequency and lead to a drift in the absorption spectrum.^[144, 145] The surface plasma modes of anisotropic particles have higher oscillator strengths and are more sensitive to surface perturbations than spheres.^[146] This is also confirmed by our experimental observations as the UV-vis spectra shown in Figure 4.14. In this work, we chose the worm-like particles for sensing detection of inorganic ions because they have two plasma bands and large surface areas than gold spheres. In addition, treating the Au worm-like particles with Na₂S induced a concentration-dependent shift in plasma resonance toward the longer wavelengths. Such a shift in the SPR might be ascribed to the modulations in the particle dielectric function by sulphide adsorption, and the attachment could stabilize the particle in suspension.^[147] The decrease in optical intensity with sulphide concentration indicates that the S²⁻ ions served primarily as a scavenger for AuCl₄⁻ ions, effectively removing them from the reaction mixture.^[126]

The selectivity of gold worm-like particles towards various anions like F⁻, Cl⁻, Br⁻, and I⁻ ions was examined. It was found that they produced less impact on the plasma resonance as shown in Figure 4.14C. The plasma bands centred at 526 and 778 nm still remained as it was even if the concentration was increased up to 60 ppm. The results reveal that the as-prepared worm-like particles exhibit a good selectivity in sensing detection of S²⁻ ions rather than F⁻, Cl⁻, Br⁻, and I⁻ ions under current conditions. This would be useful to extend anisotropic gold structures into chemical or biochemical sensing applications.

4.1.6 Conclusions

We have investigated the shape-controlled synthesis, growth mechanism, and ionic sensing application of gold worm-like nanoparticles by combination of experiments and theoretical simulations. The findings can be summarized as follows: (i) a new synthesis strategy is proposed to control shape/size by separating the nucleation and growth of

particles as far as possible; (ii) gold nanoparticles with different shapes and sizes can be controlled through an environmentally friendly approach by using non-toxic PVP and sodium citrate in aqueous solution; (iii) the worm-like nanoparticles have dominant sides being {110} planes and grow along [001] direction; (iv) the orientation attachment by fusing Au{111} planes has been confirmed by DFT simulations due to the weakest BE of Au{111}-PVP among the three; (v) these worm-like nanoparticles can be used for ionic sensing detection of S^{2-} ions rather than F^- , Cl^- , Br^- , and I^- ions in aqueous solution; and (vi) the third functionality of PVP to reduce $AuCl_4^-$ ions to metal gold atoms was confirmed in our work. This comprehensive study would be very useful for shape-controlled synthesis of metal nanoparticles with potential applications in chemical and biochemical sensors.

4.2 Silver nanoplates

Many methods have been developed to produce nanoplates, however, the results show the particles are in a wide size distributions range and low surface-to-volume ratios, with more than 10 nm is thickness. To maximize the surface-to-volume ratios of nanoplates; for example, Xia *et al* ^[148] previously reported a two-step thermal approach for slim triangular nanoplates with edge length over 100 nm in aqueous solution; however, refluxing the silver nanoparticles for 10 h was necessary, and the product was a mixture of nanoplates and nanobelts. For this reason the development of an environmentally friendly aqueous synthesis strategy to generate 2D silver nanostructures with narrow size distributions and high surface-to-volume ratios is still a challenging problem worldwide.

Here we report a newly developed synthesis method, namely, *a self-seeding coreduction hydrochemical route*, to generate silver nanoplates of triangular as well as circular shapes with narrow size distribution. In this method, the *self-seeding* process means that the silver seeds serving as nuclei for the growth of silver nanoparticles are formed autogenously in a same reaction system rather than added externally. ^[149]

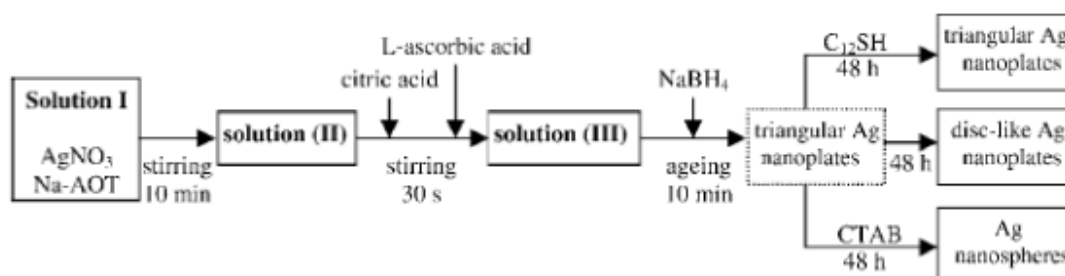


Figure 4.15 Schematic showing the procedures in the self-seeding coreduction approach. ^[136]

This is different from the synthesis of gold or silver nanorods, ^[16, 33, 126] in which the external seeds were first synthesized and kept for at least 2 h before being used for generating nanorods. The *coreduction* means that the nucleation reaction is initiated by adding trace NaBH_4 solution, and the subsequent growth of the freshly formed tiny silver nanocrystals was achieved by the synergetic reduction of citric acid and L-ascorbic acid

at room temperature. The *hydrochemical* method means that the synthesis of silver nanoplates occurs in aqueous solution rather than in organic solvents that are environmentally unfriendly. In this method, the use of surface stabilizer, i.e. sodium bis(2-ethylhexyl) sulfosuccinate (NaAOT), also plays an important role in controlling the preferential growth of silver nanoplates. ^[149] The experiment procedure can be summarized as shown in Figure 4.15. ^[136]

4.2.1 Shape and Size

Triangular silver nanoplates with narrow size distribution can be achieved by the following procedures used in a typical protocol. Trace NaBH₄ (the molar ratio of BH₄⁻ to Ag⁺ is 1/625) solution was quickly injected for bursting tiny silver nuclei, and then the subsequent particle growth was achieved by the combined reduction of citric acid and L-ascorbic acid. The so-formed silver nuclei acted as both nucleation centres and as a catalyst for the reduction of both citric acid and L-ascorbic acid in this system. Then, the silver nanocrystal facets developed and grew into a desired shape stabilized by AOT molecules. ^[149]

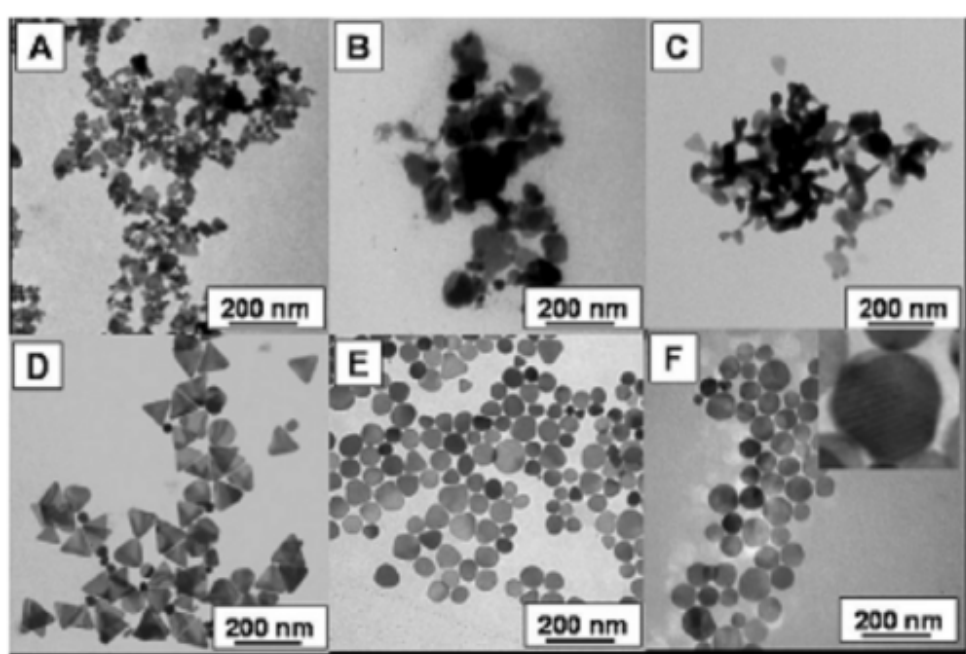


Figure 4.16 TEM images ((A)–(F)) showing the evolution of the silver nanoparticles from unshaped particles to triangular plates, and finally circular discs, over 1, 3, 5, 10

min, 10 h, and 100 h, respectively. The inset of Figure 4.16F shows a TEM image of the Moiré fringe pattern formed by stacking two nanodiscs. ^[149]

TEM images (Figure 4.16) show the formation and evolution of silver nanoplates as a function of time. Silver crystals of irregular shape at 1, 3, and 5 min are shown in Figures 3-16A-C. Monodispersed triangular nanoplates were formed after 10 min growth (Figure 4.16D) through the Ostwald ripening process. ^[150] It is worth noting that the angles of the triangular plates gradually disappeared within 10 h and intermediate products with shapes between triangles and discs were formed (Figure 4.16E). Upon further ageing up to 100 h, the triangular plates could evolve to discs with smooth circular edge at room temperature (Figure 4.16F). So there are two possibilities for the evolution of silver nanoplates from triangular to circular shape:

- (i) the Ag atoms come from the outside of triangular particles to increase the size, and
- (ii) the Ag atoms migrate between crystalline planes in the interior of individual particles.

It should be mentioned that the thickness of the plates was maintained during the shape evolution from triangular to circular. The inset of Figure 4.16F displays a typical TEM image of the Moiré fringe pattern formed with their flat faces touching. ^[151] This clearly confirmed the characteristic features of thin and flat nanodiscs.

Optical Properties

The corresponding UV-vis spectra (Figure 4.17) show that the maximum absorption intensity increases gradually up to 10 min (Figures 3-17A-D), which means the silver content increased and the shape of particles also changed. Due to dipole in-plane resonance of the nanoplates, the maximum plasmon resonance blue-shifted from 877 (curve D, 10 min) to 775 (curve E, 10 h), and 646 nm (curve F, 100 h), over a period of hours. ^[152, 153] Over several hours, it was observed that the plasmon resonance blue-shifted from 537 (D) to 490 (E), and 430 nm (F). This is the result of the shape evolution from triangular plates to circular discs. These time-dependent absorption features are typical for anisotropic silver particles. ^[152-157]

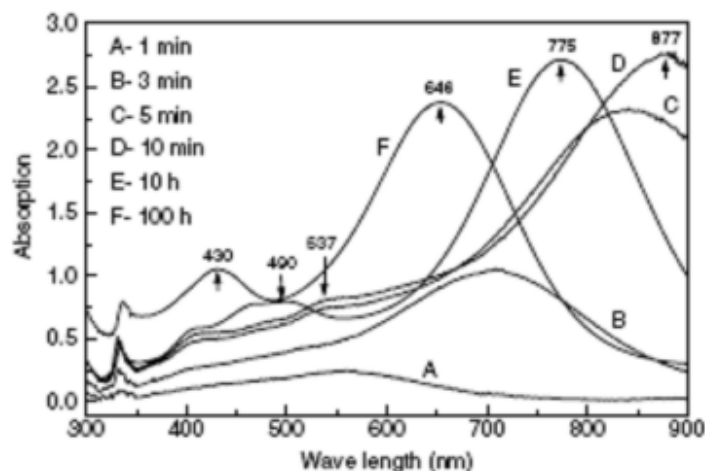


Figure 4.17 The UV–vis spectra corresponding to the silver nanocrystals obtained at different times: (A) 1 min, (B) 3 min, (C) 5 min, (D) 10 min, (E) 10 h, and (F) 100 h, respectively. ^[149]

One representative TEM image of an individual disc is shown in Figure 4.18A and its crystalline structure can be confirmed by the SAED pattern (inset of Figure 4.18A) and high-resolution TEM image (Figure 4.18B). The diffraction spots indicate that the silver disc has a single crystalline structure, and the hexagonal symmetry of the scattered spots indicates that the silver disc is highly [111] oriented with the top normal to the electron beam. The diffraction spots could be indexed based on the face-centre-cubic (fcc) silver structure. Three sets of diffraction spots could be indexed as $(1/3)\{422\}$ (circled spot), $\{220\}$ (boxed spot), and $\{311\}$ (spot circumscribed by triangle) based on Bragg reflections with lattice spacing of 2.5, 1.44, and 1.23 Å, respectively. ^[149]

The presence of the $(1/3)\{422\}$ reflections specifies that the top and bottom of silver discs are atomically flat. ^[158, 159] The lattice spacing of 0.236 nm of the silver disc (Figure 4.18B) could be attributed to an Ag (111) facet, which indicates the single-crystalline silver disc formed with the surface bounded by Ag{111} facets. The thickness of the silver disc was measured by atomic force microscopy (AFM). Figure 4.18C shows the profile (side view) of silver nanodiscs, and the down triangle pairs indicate that the thickness of a disc is ~2.3 nm and the diameter is around 60 nm (Figure 4.18D). ^[149]

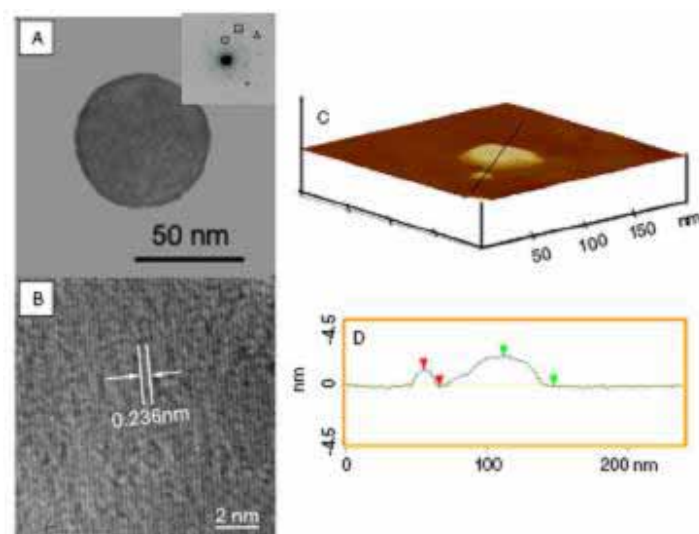


Figure 4.18 (A) A representative TEM image of one individual silver nanodisc with its selected area electron diffraction (SAED) pattern (inset). In the SAED pattern, the circled spot, boxed spot, and spot circumscribed by triangle correspond to $(1/3)\{422\}$, $\{220\}$ and $\{311\}$ Bragg reflections with lattice spacings of 2.5, 1.44 and 1.23 °A, respectively. (B) The HRTEM image shows the lattice spacing 2.36 °A corresponding to Ag $\{111\}$ facets. (C) AFM image (side view) of the silver nanodiscs obtained over 100 h. (D) The thickness of the nanodisc is estimated to be ~2.3 nm. ^[149]

In the past years, some efforts have been made to recognize the growth mechanism of metal nanocrystals. ^[152-167] For example, the surface energies in bare silver as driving the formation of truncated octahedra for free cluster that was described by Ferrando *et al.* ^[165-167] However, such a contribution will weaken upon the adsorption of molecules (e.g. AOT on silver surface), and the interaction potential energies between the metal surface and the adsorbed molecules would play a dominant role in determining the shape formation of the nanoparticles.

In addition El-Sayed *et al.* ^[168, 169] studied the shape distribution of platinum nanoparticles at different growth stages, and the formation and evolution of anisotropic nanoparticles can occur due to two reasons:

- (i) the growth rates differ at different planes of a particle, and
- (ii) particle growth competes with the capping action of stabilizers.

A similar scenario may be operative in our case. The competitive and preferential binding of AOT molecules on different crystalline facets could control the formation of silver nanoplates.

To be more quantitative, following the work of Zeng *et al.*,^[170, 171] molecular dynamics (MD) simulation was used to analyse the interaction energies of AOT molecules with the silver atomic surface. For each silver crystalline plane (i.e. (111), (110), or (100)), simulations were performed on three models with the same MD cell dimension but different components (i.e. silver plane with AOT molecules (A–B), isolated silver plane (A), and isolated AOT molecules (B)). The preferential adsorption of AOT molecules on silver planes is determined by the interaction potential energy. Such energy is calculated by the following equation: $\Delta U_{\text{int}} = U_{\text{A-B}} - U_{\text{A}} - U_{\text{B}}$, where $U_{\text{A-B}}$, U_{A} and U_{B} are the potential energies of silver plane with AOT molecules (A–B), isolated silver plane (A) and isolated AOT molecules (B), respectively. The interaction potential energies between AOT molecules and the silver atomic planes were calculated as Ag{111} – 460.1, Ag{110} – 323.4, and Ag{100} – 249.9 kcal mol⁻¹, respectively. In principle, the lower the interaction energy the more stable the system, so the silver {111}–AOT system is the most stable among the three. This indicates that more AOT molecules are apt to bind at the Ag{111} planes, which maintains Ag{111} as the basal plane and leads to the preferential growth of other facets of crystalline silver. Full details of interaction energies and atom density profiles calculated by using the MD method will be discussed in the next section.

4.2.2 Size Distribution

Our statistical investigation suggests that the transformation of silver nanoplates is consistent with the latter explanation. Figure 4.19 shows the shape evolution from triangular nanoplates (A–C) to nanodiscs (D–F), and the statistical analysis of the circumference and the surface area of individual particles. As can be seen from Figure 4.19 the average circumference decreases by ~20 nm from a triangular plate, 189 nm \pm 27% (B), to a disc, 169 nm \pm 29% (D), whereas the average surface area of the silver

nanoparticle only decreases slightly from the triangular plate, $4393 \text{ nm}^2 \pm 18\%$ (E), to the disc, $4360 \text{ nm}^2 \pm 19\%$ (F).^[149]

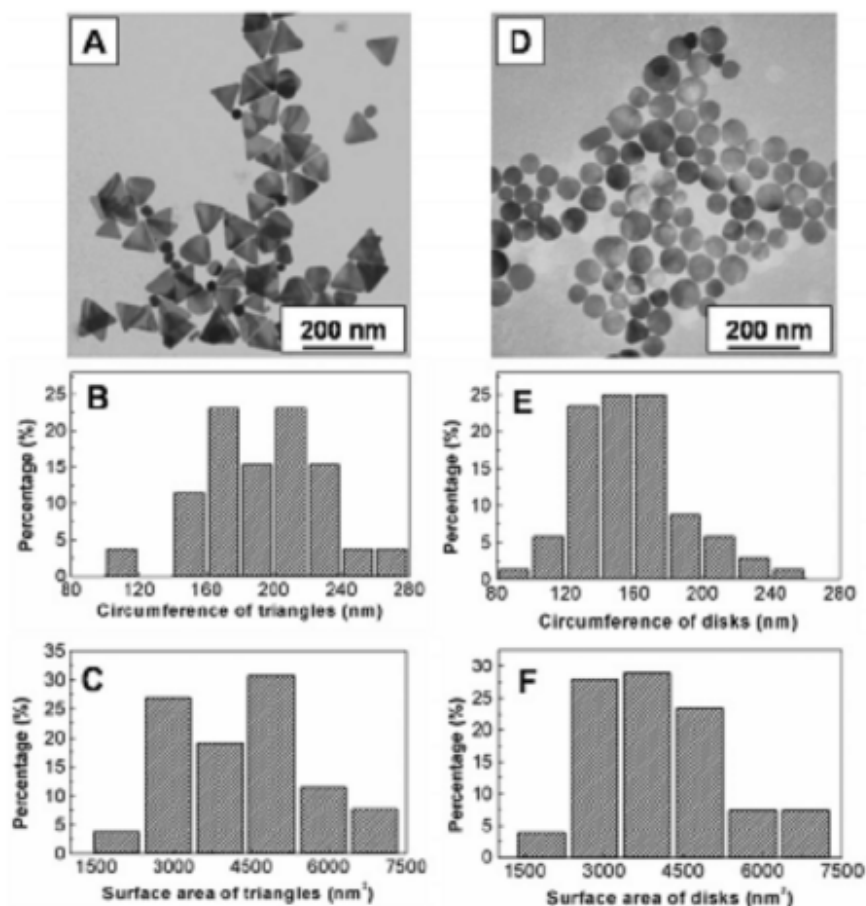


Figure 4.19 TEM images and the size distributions of circumference and surface area showing the transformation from triangular silver plates (A–C) to circular discs (D–F).^[149]

These results indicate that the shape evolution of a particle occurred due to the atomic migration on its side surface (the thickness is constant). This is in good agreement with the theoretical calculations suggesting that the small difference of the interaction energies between AOT–Ag{110} and AOT–Ag{100} planes would provide a possibility of internal atom migration. The evolution from triangular plates to discs can reduce the total surface free energy. Geometrically, a disc has lower surface energy than a triangular plate of the same surface area. More on this will be discussed in the next few sections.^[149]

4.2.3 Effect of Other Surfactants

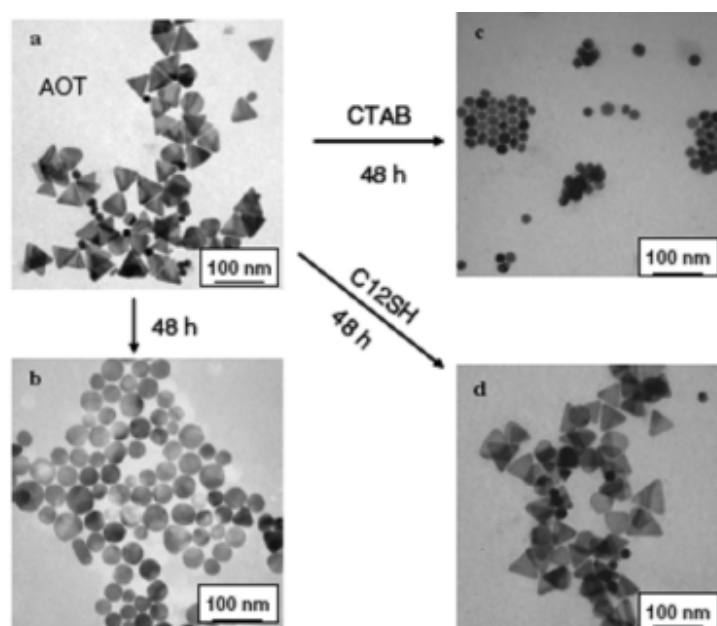


Figure 4.20 Shape transformation of silver nanoparticles under various conditions: (a) triangular silver nanoplates formed after ageing for 10 min under AOT molecules; (b) disc-like silver nanoplates formed after further ageing for 48 h; (c) silver nanospheres formed after further ageing for 48 h under the addition of CTAB molecules; (d) triangular silver nanoplates remaining after ageing for 48 h under the addition of C₁₂SH molecules. [136]

The morphologies of silver nanoparticles depend significantly on the ageing time and the addition of surfactants. As shown in Figure 4.20 the shape evolution of silver nanoparticles is evidenced by the TEM images. The small silver nanocrystals produced at the initial stage in the presence of AOT surfactant were observed to grow into triangular silver nanoplates after 10 min (Figure 4.20A). Due to the unstable condition of these triangular nanoplates capped with AOT, they subsequently transformed into an intermediate after 10 h of ageing. Finally, after 48 h of ageing, all nanoplates were transformed into disc-like silver nanoplates (Figure 4.20B). Therefore, it is imaginable that the generated nanoparticles were transformed sequentially into triangular, polyhedral and disc-like shapes. [136]

Moreover, when CTAB surfactant was added into the freshly prepared suspension of triangular silver nanoplates, these triangular nanoplates were observed to convert into nanospheres after 48 h of ageing (Figure 4.20C). When C₁₂SH surfactant was added, the shape of triangular nanoplates was frozen and after ageing for 48 h or even longer (Figure 4.20D) it went stable. [136]

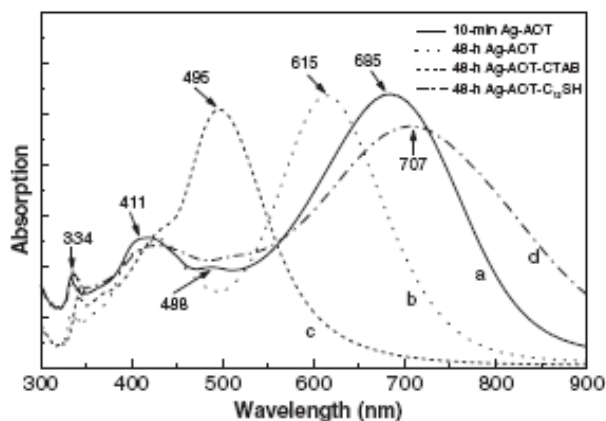


Figure 4.21 The corresponding UV-vis spectra to the silver nanoparticles: (A) triangular silver nanoplates formed after ageing for 10 min under AOT molecules; (B) disc-like silver nanoplates formed after further ageing for 48 h; (C) silver nanospheres formed after further ageing for 48 h under the addition of CTAB molecules; (D) triangular silver nanoplates remaining after ageing for 48 h under the addition of C₁₂SH molecules. [136]

Such morphology evolution, due to its strong dependence on the shift of the plasmon resonances of silver nanoparticles, was also evident from the UV spectra measurement (Figure 4.21). The initial silver nanoplates formed after ageing for 10 min under AOT molecules show the characteristic plasmon resonances of triangular nanoplates centred at 685, 488, 411 and 334 nm. The maximum plasmon resonance of such triangular silver nanoplates (i.e. 685 nm in Figure 4.21 A) shifts after ageing for 48 h toward a shorter wavelength (i.e. 615 nm, Figure 4.21 B) which is attributed to silver nanodiscs. When ageing for 48 h with the addition of CTAB molecules (Figure 4.21 C) it shifts further to 495 nm that is attributed to silver nanospheres. When a C₁₂SH molecule was added, only a slight shift of the wavelength (i.e. 707 nm, Figure 4.21 D) was observed after 48 h of ageing, which means that C₁₂SH can stabilize the shape of triangular silver nanoplates.

[136]

4.2.4 Effect of Reducing Agents

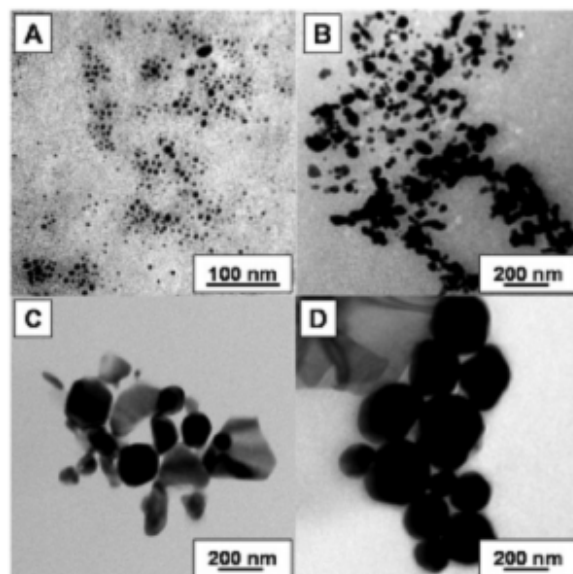


Figure 4.22 The effect of the reducing agents on the shape of silver nanoparticles: (A) NaBH_4 , (B) citric acid + NaBH_4 , (C) L-ascorbic acid + NaBH_4 , and (D) citric acid + L-ascorbic acid.^[136]

The *coreduction* procedure plays a critical role in the shape control of silver nanoplates. Here three kinds of reduction agents, i.e. NaBH_4 , citric acid and L-ascorbic acid, were used in the synthesis protocol. The influences of any one or two of the three reducing agents on the morphology and size of silver nanoparticles were tested, and representative TEM images are shown in Figure 4.22. In the reduction reactions, the molar ratios of NaBH_4 , citric acid, and L-ascorbic acid to Ag^+ ions are maintained at 1/625, 1.2, and 1.0, respectively. The sole use of NaBH_4 could just generate particles around 3–5 nm in diameter (Figure 4.22A), and sole citric acid could produce unshaped particles at room temperature over several hours, but sole L-ascorbic acid had no reduction with Ag^+ ions in the aqueous AOT solution even after 24 h. When using any two of the three, such as NaBH_4 and citric acid, or NaBH_4 and L-ascorbic acid, or citric acid and L-ascorbic acid, we just obtained silver particles with irregular shape, as shown in Figures 4-22B–D. Here the first two combinations could quickly lead to a color change of solution, while the last combination took at least 5min to produce a color change. Notably, no triangular silver nanoplates were synthesized when using any one or two of the three reducing agents.

Therefore, the *coreduction* of all the three reducing agents is critical for the shape control of triangular nanoplates.

4.2.5 Theoretical Simulation

The interaction energies between individual surfactants (i.e. AOT, C₁₂SH, CTAB) and different silver crystalline planes (i.e. (100), (110), (111)) were calculated. For each silver–surfactant system, the three-dimensional model (Model I) consists of one silver crystal plane and a certain amount of surfactant molecules on the silver surface (Figure 4.23A). MD simulations were also performed for two other models: silver crystal plane only (Model II, Figure 4.23B) and surfactants only (Model III, Figure 4.23C) to work out the interaction energy between surfactant and silver crystal plane. To calculate the interaction potential energy, which includes intermolecular (i.e. Ag–surfactant and surfactant–surfactant) interactions (e.g. electrostatic and VDW) and intra-molecular (i.e. surfactant) interactions (e.g. bond, angle, inversion and torsion) the COMPASS force field was used. All the systems were subjected to energy minimization for the structural optimization before MD simulation. The NVT simulations lasted for 50 ps with a time step of 1 fs. Simulation data were collected in the last 20 ps for statistical and structural analysis.^[136]

4.2.5.1 Adsorption of surfactant

The adsorption of surfactant on a silver surface can be observed from the MD results. Initially, the surfactant molecules are placed randomly over the silver surface. During the simulation, it was observed that the molecules moved towards the silver surface and were mixed up due to the intermolecular interactions between the surfactants. Figure 4.24 shows the AOT surfactant movement on the surface of silver (100) during the simulation. Similar adsorption behaviors were observed on other silver surfaces as well as for the surfactants of C₁₂SH and CTAB. However, as can be seen in the following analysis, the interaction strength between surfactant and silver crystal plane and molecular packing on the silver surface are different in these systems. There are a number of active sites on the surface of bare metal nanoparticles. Such active sites increase dramatically with the decrease of particle size because of the obvious increase of surface–volume ratio.

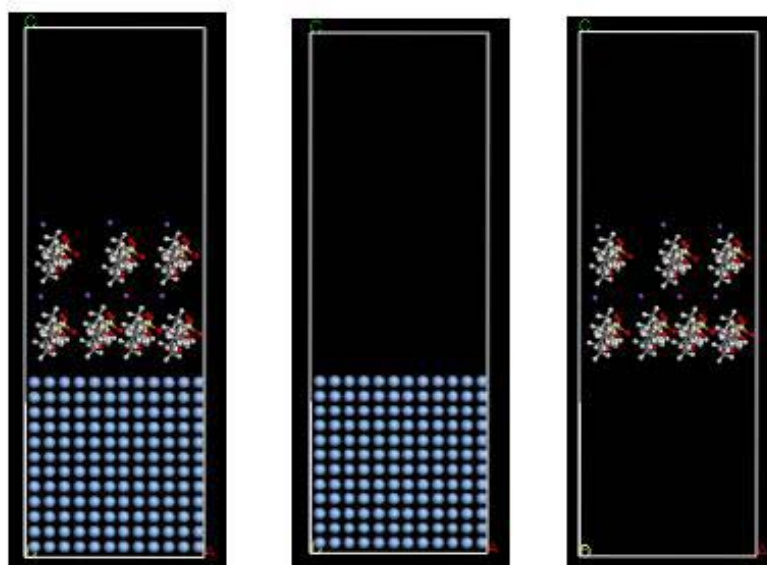


Figure 4.23 Molecular models of: (a) silver crystal plane and surfactants; (b) silver crystal plane only; (c) surfactants only. Here the crystal plane (in balls) is Ag (100) and the surfactant is AOT which contains atoms of sulfur (yellow), oxygen (red), grey (carbon), white (hydrogen) and sodium (purple).^[136]

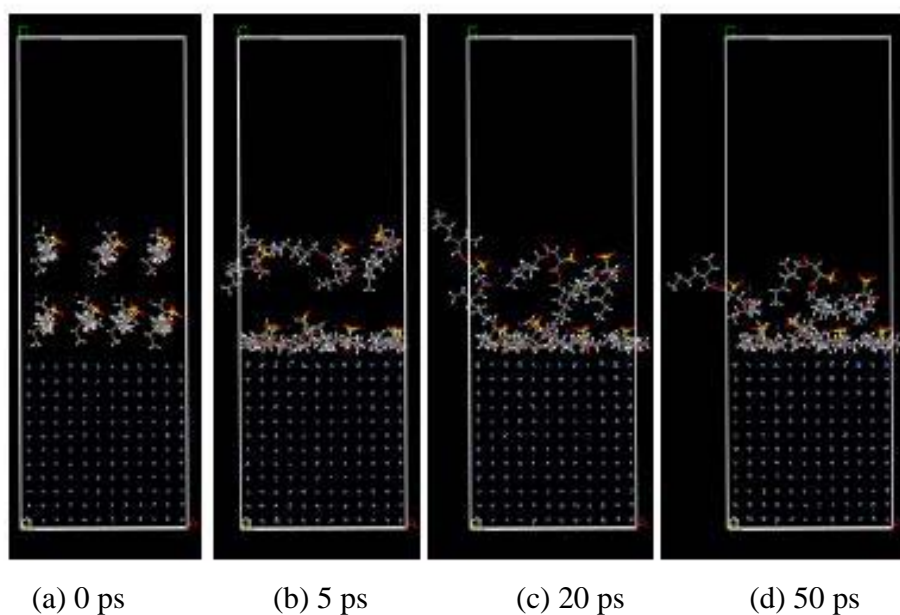


Figure 4.24 Evolution of AOT molecular adsorption on silver crystal surface (100) at time: (a) 0 ps; (b) 5 ps; (c) 20 ps, (d) 50 ps. Here the silver crystal plane (100) is expressed as dots and AOT is expressed as sticks containing atoms of sulfur (yellow), oxygen (red), grey (carbon), white (hydrogen) and sodium (purple).^[136]

Moreover, for the same metal crystal, the features of active sites could be different from one plane to another. Such a difference plays a significant role in determining the molecular adsorption on the metal surface and hence the growth of metal crystals.^[136] Theoretically, molecular adsorption can be reflected from the interaction strength between the molecules and crystal surface. To investigate the growth behaviour observed during the synthesis of silver nanoparticles, the interaction energies (U) were calculated for different surfactant–silver plane systems, given by:^[136]

$$U = E_I - E_{II} - E_{III}$$

where E_I , E_{II} and E_{III} are the potential energies corresponding to Models (I), (II) and (III) as described previously. The calculated potential energy indicates the interaction feature between surfactant and silver surface: a negative value indicates an attractive interaction while a positive value means a repulsive interaction and the larger the value the stronger the interaction. The calculated interaction energies summarized in Table 4.1 provide distinct evidence of the growth behaviors of silver nanoparticles and hence the shape control.^[136]

Table 4.1 The calculated interaction energies (kcal mol^{-1}) for various surfactant–silver plane systems.^[136]

	AOT	C₁₂SH	CTAB
Ag(100)	-249.9	-308.6	-397.9
Ag(110)	-323.4	-361.1	-482.8
Ag(111)	-460.1	-959.0	-503.6

4.2.5.2 Formation of silver nanoplates.

The relatively large negative interaction energy ($-460.1 \text{ kcal mol}^{-1}$) between AOT molecules and Ag (111) specifies that there was a tendency for the AOT molecules to adsorb on Ag (111) rather than Ag (100) and Ag (110) surfaces. The selective adsorption of AOT may lead to a larger coverage of AOT molecules on Ag (111) surfaces than that of the other two surfaces. This prevents the approach of the Ag species to that surface but allows the growth of silver crystal along Ag (100) and Ag (110) surfaces. In addition, the migration of Ag atoms between Ag (100) and Ag (110) surfaces may happen because the

interaction energies between AOT molecules and these two surfaces showed only a small difference of $73.5 \text{ kcal mol}^{-1}$. Such surface atomic migration is further supported from experimental observation. That is, the size of the silver nanoplates in terms of circumference was unchanged despite their shape evolution from triangular to polyhedral and finally disc-like after ageing for 48 h (Figure 4.20B). This is contradicting to the crystal orientation of the disc-like silver nanoplates that was investigated by high resolution TEM (Figure 4.18) and selected area electron diffraction (SAED).^[136] Briefly, the hexagonal symmetry of the scattered spots in the SAED pattern indicates that the silver disc-like nanoplate is highly [111] oriented with the top normal to the electron beam. The lattice spacing of 0.236 nm in the high resolution TEM image indicates that the single-crystalline silver disc-like nanoplate is formed with the surface bounded by Ag {111} facets.

4.2.5.3 Stabilization of triangular silver nanoplates

The interaction energies between C_{12}SH and three Ag surfaces (especially with Ag (111), $-959.0 \text{ kcal mol}^{-1}$) are all larger than those of the corresponding AOT–silver systems. Thus, the addition of C_{12}SH molecules may result in their stronger adsorption on these three surfaces as well as the replacement of the adsorbed AOT molecules. Such a strong interaction would be helpful for stabilizing the shape of Ag nanoplates. Meanwhile, the enhanced molecular adsorption and coverage on the silver surface inhibit the atomic migration between Ag (100) and Ag (110) surfaces. On the other hand, the smaller difference in interaction energy ($52.5 \text{ kcal mol}^{-1}$) between Ag (100) and Ag (110) surfaces indicates a tendency of equivalent coverage of surfactants on both surfaces. Therefore, with the addition of C_{12}SH , silver nanoparticles remain in their triangular shape even after ageing for 48 h (Figure 4.20D). To further confirm the above point, MD simulation was performed for the system consisting of Ag (100) plane, AOT, and C_{12}SH molecules. The C_{12}SH molecules are shown (Figure 4.25) to approach the AOT-coated Ag (100) surface and finally interlace with AOT molecules. The result also indicates that the interaction energy between C_{12}SH and Ag (100)–AOT is $-104.6 \text{ kcal mol}^{-1}$. This negative value indicates an attractive interaction between C_{12}SH molecules and Ag (100)–AOT. Moreover, the addition of C_{12}SH leads to a much more stable system (i.e.

Ag (100)–AOT–C₁₂SH) because the total energy is reduced by 130.0 kcal mol⁻¹ compared to that of the Ag (100)–AOT system.^[136]

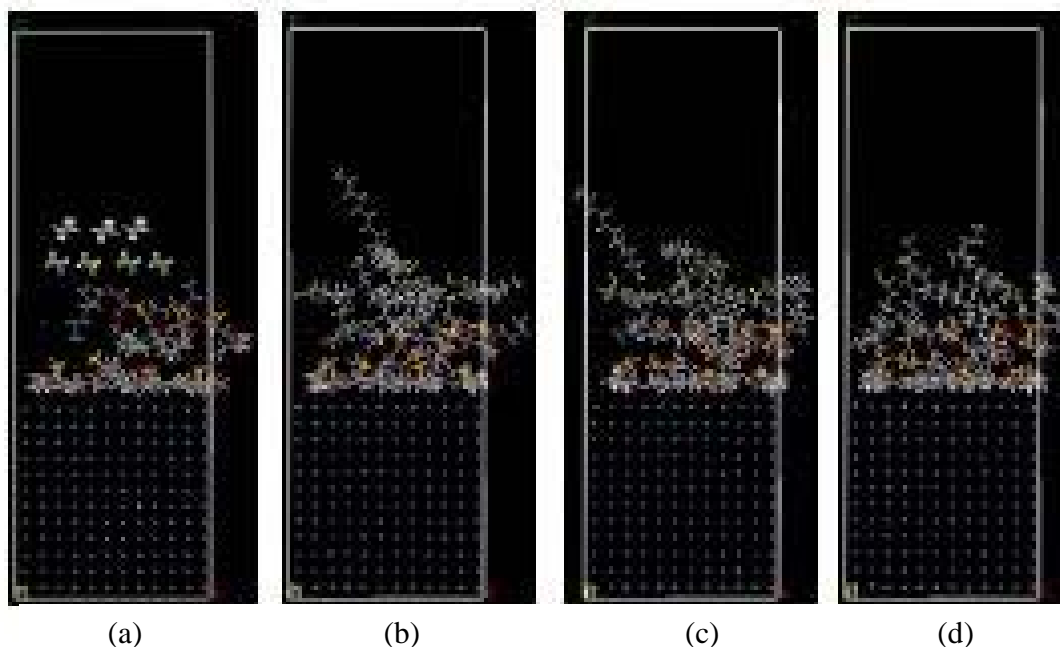


Figure 4.25 Evolution of C₁₂SH molecular adsorption on AOT coated silver nanoparticle surface (100) at time: (a) 0 ps; (b) 5 ps; (c) 20 ps, (d) 50 ps. Here a silver crystal plane (100) is expressed in dots while AOT and C₁₂SH are expressed in sticks containing atoms of sulfur (yellow), oxygen (red), grey (carbon), white (hydrogen) and sodium (purple).^[136]

4.2.5.4 Formation of silver nanospheres

The interaction energies of Ag (100)–CTAB and Ag (110)–CTAB systems (Table 4.1) are much more negative than those of the corresponding systems containing AOT or C₁₂SH. This means that CTAB molecules have much stronger interactions with the surfaces of Ag (100) and Ag (110) than those of AOT or C₁₂SH molecules. Therefore, these two surfaces are likely to adsorb CTAB other than AOT and C₁₂SH molecules, and the replacement of adsorbed AOT with CTAB molecules may happen as well.^[136]

Besides, there is a relatively smaller difference in interaction energies between CTAB and three silver surfaces (i.e. in the range of ~400–500 kcal mol⁻¹). This would lead to an

equivalent adsorption and coverage of CTAB molecules on these three surfaces. The results hence explain well the isotropic growth under the addition of CTAB molecules to the Ag–AOT solution and the formation of silver nanospheres (Figure 4.20C). It appears that the size of these silver nanospheres formed under the addition of CTAB molecules is smaller than that of triangular nanoplates. This is true in terms of surface area but not volume. The average diameter of these silver nanospheres was approximately around 23 nm. For silver nanoplates, the particle size is about 2.3 nm in thickness and 70–80 nm in edge length, estimated from the TEM and atomic force microscope results. ^[136] The results indicate that the average volume of a nanoparticle has not changed in the evolution of particle shape from plate to sphere. ^[136]

4.2.5.5 Atom distributions at silver surface

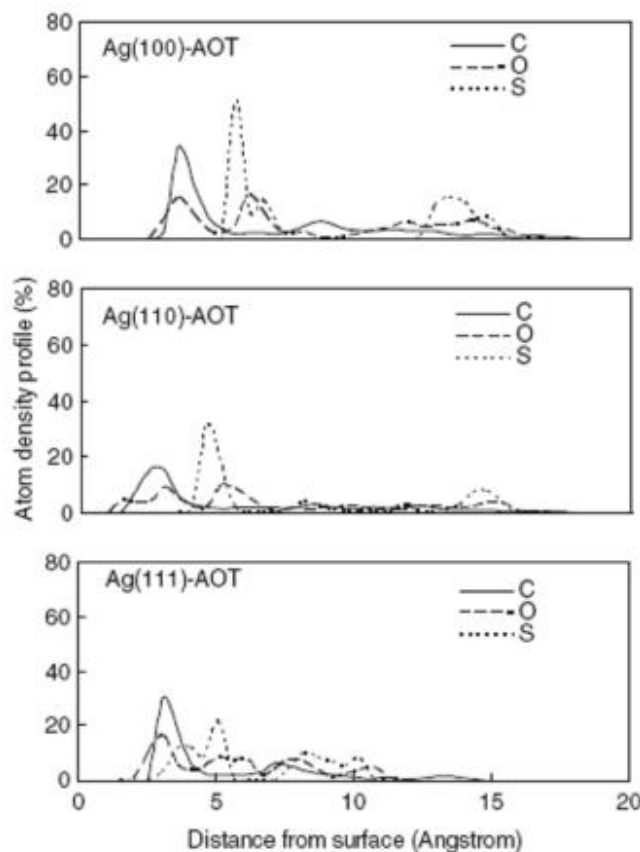


Figure 4.26 Atom density profiles of AOT surfactant on silver surfaces: Ag (100) (top), Ag (110) (middle) and Ag (111) (bottom). ^[136]

MD simulation allows one to estimate quantitatively the molecular structure at the interface. Figure 4.26 shows the atom density profiles of AOT molecules on three Ag surfaces. The distributions indicate that AOT molecules largely stay close to the Ag surface with some of them radiating away from the surface.^[136]

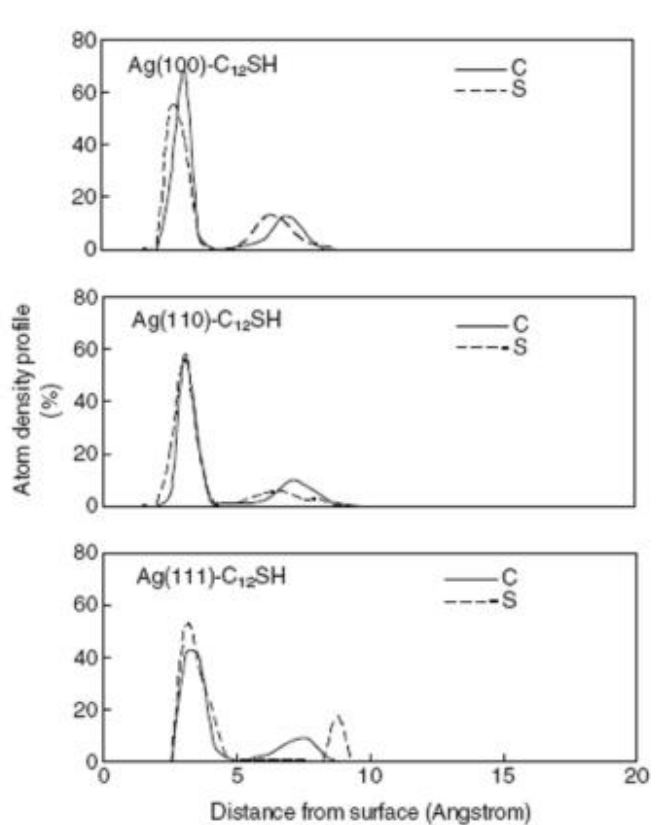


Figure 4.27 Atom density profiles of $C_{12}SH$ surfactant on silver surfaces: Ag (100) (top), Ag (110) (middle) and Ag (111) (bottom).^[136]

However, the overall atoms in the Ag (111)–AOT system stay closer to the Ag surface than those in the other two systems (i.e. Ag (100)–AOT and Ag (110)–AOT). Almost all AOT molecules in the Ag (111)–AOT system lie within 1.2 nm of the silver surface while in the other two systems some AOT molecules lay around 1.4 nm away from the surface. In the case of $C_{12}SH$ molecules, the sharp peaks in atom density profiles (Figure 4.27) indicate that most of the $C_{12}SH$ molecules are closely packed on Ag surfaces and form a monolayer structure with a centre around 0.3 nm. In addition, the distributions of carbon and sulfur atoms around the sharp peak are very similar. Thus, the $C_{12}SH$ molecules predominantly lie flat on Ag surfaces. This behavior is different from that of

AOT molecules. In the case of Ag-CTAB systems, layering structures near the Ag surface are also observed as shown from their atom density profiles (Figure 4.28). However, there are some molecules, which stay away from the surfaces, especially Ag (100) surfaces. As estimated from the distribution of carbon chains, the centre of the layering structure is around 0.30 nm away from the silver surface. Moreover, the carbon chains lie closer to the surface than nitrogen atoms whose peaks are around 0.35 nm from the silver surface. Interestingly, there are also over half of bromine atoms (Figure 4.28) adsorbing on Ag surfaces around 0.41 nm.^[136]

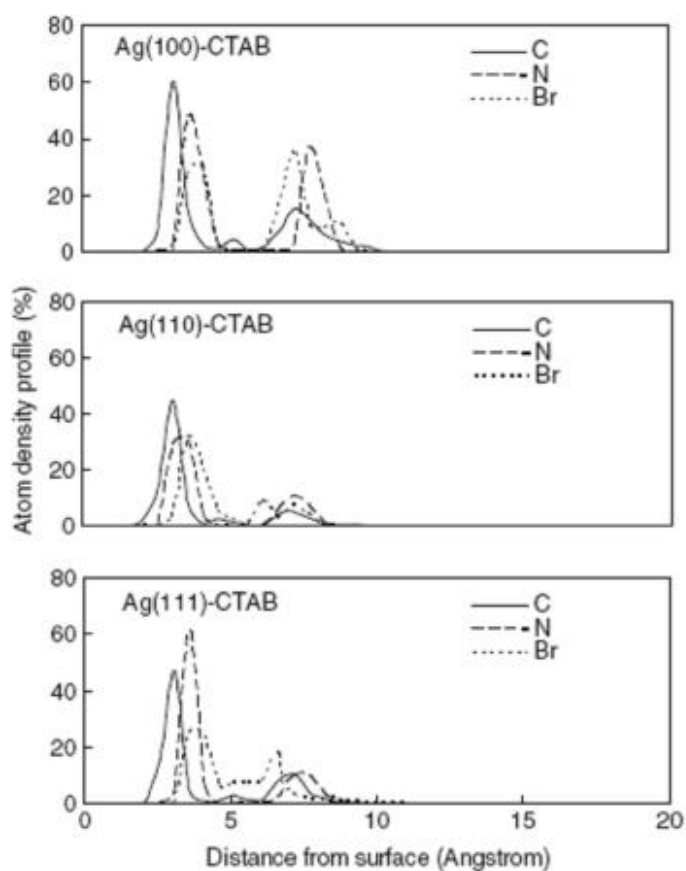


Figure 4.28 Atom density profiles of CTAB surfactant on silver surfaces: Ag (100) (top), Ag (110) (middle) and Ag (111) (bottom).^[136]

4.2.6 Gold Rings

The synthesized silver nanodiscs exhibit high chemical activity and can be applied in areas of physics, chemistry and materials. For example, as explored in some detail in this

work, such nanodiscs can be used as a scaffold template to fabricate gold rings through a galvanic replacement reaction in aqueous AuCl_4^- solution. After reacting with AuCl_4^- ions, Au nanorings other than closed sealed shells formed, as are shown in Figure 4.29A. The diffraction peaks recorded in the XRD pattern of Au nanorings (Figure 4.29B) could be attributed to (111), (200), (220), (311), and (222) planes of fcc gold with a lattice constant of 4.078 \AA according to JCPDS file2 no. 04-784. The diffraction intensity ratios between the planes indicate no preferential orientation in the gold nanorings.^[136]

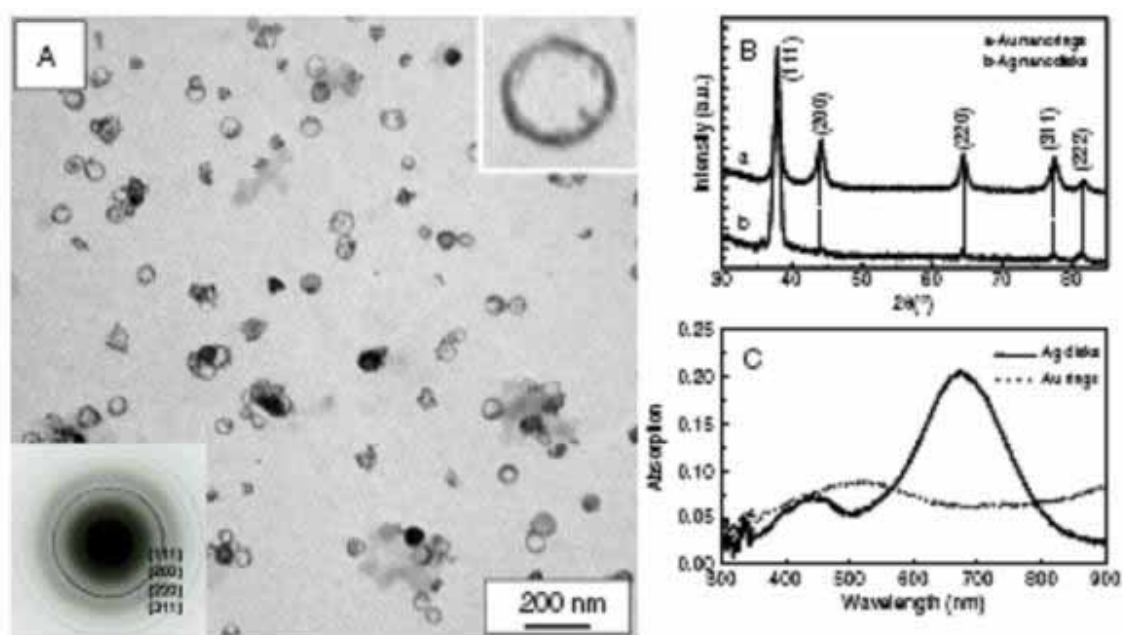


Figure 4.29 (A) TEM image and the inset SAED pattern of gold nanorings, (B) the XRD patterns of gold nanorings (a) and silver nanodiscs (b), and (C) the corresponding UV-vis spectra of gold nanorings (dotted line) and Ag nanodiscs (solid line).^[136]

This can also be evidenced from the SAED pattern (inset of Figure 4.29C) of the Au nanorings. For comparison of the replacement process, the XRD diffraction peaks of silver nanodiscs were recorded and assigned to (111), (200), (220), (311), and (222) planes of fcc silver (pattern b in Figure 4.29B). Here it is worth noting that the intensity ratios between (200) and (111), and between (220) and (111) planes, are smaller than the conventional values (0.14 versus 0.4), and (0.12 versus 0.25) based on the standard card (JCPDS file no. 04-783) (see footnote 2). These abnormal intensity ratios indicate that

silver nanodiscs are abundant in {111} facets and Ag{111} is the basal plane of the nanoplate, with the {111} planes being preferentially oriented parallel to the surface of the supporting substrate. ^[172]

The absorption spectra of silver discs before and after reaction with AuCl₄⁻ ions are shown in Figure 4.29C. The plasmon bands of silver nanodiscs disappeared (solid line) and a new band emerged around 520 nm (dotted line) that was attributed to gold nanocrystals. Considering the formation mechanism of gold rings, the replacement reaction was expected to occur first on the surface of a silver nanodisc {110} and {100} facets, and then {111} facets, based on the results generated by the MD simulation. So a gold ring-like structure formed first around the edge bounded by {110} and {100} facets of a disc, and then the ring could serve as nuclei for further growth of gold layer into a complete shell. The crystallographic reconstruction would be favorable for the formation of gold nanorings via the Ostwald ripening process. ^[150] A similar etching mechanism has been described in making hollow forms of rods, cubes and triangular frames. ^[164, 173, 174] From another point of view, these results show that the silver template used for generating gold nanorings are discs but not spheres. ^[173, 174] It is believed that this template approach based on silver nanodiscs could be extended to produce other metallic ring-like structures as long as their oxidation potentials are higher than the redox pair of Ag⁺/Ag⁰. ^[175]

4.2.7 Conclusions

A *self-seeding coreduction hydrochemical* method has been developed for the shape control of silver nanoplates in aqueous solution. The shape of metal nanoparticles can be controlled by using different surfactants. By this method, triangular silver nanoplates and circular silver nanodiscs (~2.3 nm in thickness) have been successfully synthesized. The choice and addition of surfactants (e.g. AOT, CTAB, C₁₂SH) in the synthesis of silver nanoparticles are found to be one important factor in controlling the growth and morphological formation. By this approach, well-controlled particle shapes, including nanodiscs, triangular nanoplates and nanospheres, have been successfully achieved. Both the triangular and the circular nanoplates exhibit intense plasmon resonances that differ markedly from those for spheres or nanorods. Molecular dynamics simulation has been

used to investigate the mechanisms of the growth and shape control of such nanoparticles. The interaction energies between surfactant (i.e. AOT, C₁₂SH and CTAB) and individual Ag crystal planes (i.e. (100), (110) and (111)) have been calculated. The results indicate that the addition of AOT or AOT followed by C₁₂SH can lead to the formation of silver nanoplates because of the larger negative interaction energies on Ag (111). In Ag–AOT systems, the small difference of interaction energy between Ag (100) and Ag (110) surfaces means atomic migration may happen between these two surfaces. However, in Ag–C₁₂SH systems, such atomic migration may be impeded because they have larger negative energies than those of Ag–AOT systems. Thus, the nanoparticles remain in the triangular shape. In Ag–CTAB systems, the equivalent interaction energies on three surfaces may lead to the equivalent adsorption and coverage of CTAB molecules and hence the formation of silver nanospheres.

Clearly, MD simulation can improve our understanding of the shape control mechanisms in the synthesis of nanoparticles. The method can be used for other systems. The results would provide a useful guide in the choice of capping molecules for shape-controlled synthesis of nanoparticles. The 2D nanoplates have unique properties such as high extinction coefficient in the near infrared (NIR) region and high surface-to-volume ratios, and hence have the potential to be used in optical sensors, NIR absorbers, catalysts, or biosensors. This method would be extendable for the synthesis of 2D nanoplates of other noble metals (e.g. Au, Pd, and Pt). The synthesized silver nanodiscs have been used successfully as scaffold templates to produce gold nanorings through a galvanic replacement reaction.

4.3 Ag Induced Selenium Nanowires

In this part, a newly developed method will be demonstrated called silver-catalyzed growth route, in order to generate Selenium nanowires in aqueous solution at room temperature (RT). Different from the previous studies,^[128, 176-180] this method is advantageous because it uses no stabilizers, no sonichemical process, natural organic acid (e.g. citric acid) instead of toxic NaBH₄ or N₂H₄, particularly all operations being conducted at RT and in aqueous media. The shape and dimensions could be controlled by silver nanoparticles that were synthesized in the presence of sodium bis(2-ethylhexyl) sulfosuccinate (AOT) molecules. More interesting is that this strategy provides a new venue to obtain better understanding in the grow mechanism of t-Se nanowires as well as a new venue to generate 1-D semiconductor or metal–semiconductor heterogeneous nanostructures.^[181]

4.3.1 Shape and Size of Silver Nanoparticles

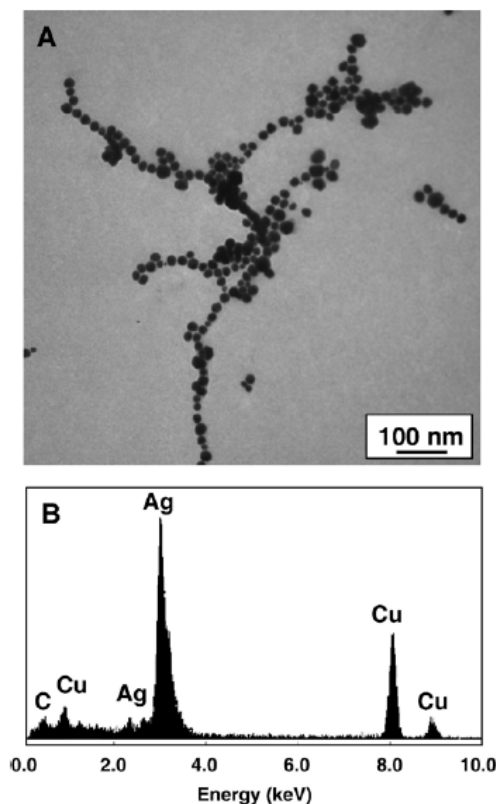


Figure 4.30 TEM image and the corresponding EDS pattern of silver nanoparticles.^[181]

The morphology and composition of the as-synthesized silver particles were checked by using TEM and EDS techniques. Figure 4.30 A shows that the size of particles is around 40 nm in diameter, and the EDS pattern indicates that the as-prepared nanoparticles are composed of silver atoms (Figure 4.30 B).^[181] The peaks of copper and carbon are caused by TEM grid covered by carbon film. The synthesized nanoparticles could be used as an inducer for further fabrication of selenium nanowires after rinsed with water.
[181]

For convenience, the method has already been described in the experimental procedures,^[181, 182] and we here focus on the key findings. The morphology and microstructure of the as-synthesized sample were characterized using transmission electron microscope (TEM) and high-resolution electron microscope (HREM). Figure 4.31A shows one representative TEM image of Se nanowires at low magnification. The uniform diameter of nanowires is around 23 nm and their lengths are in the range from hundreds of nanometers to a few micrometers. For extensive investigation, an individual Se nanowire was captured and shown in Figure 4.31B. Its selected area electron diffraction (SAED) patterns associated with different parts in the t-Se nanowire are inserted in Figure 4.31B. The diffraction spots originated from the squared part reveal that Se nanowire is single crystalline structure, in which two spots close to the center could be indexed to Se(101) (circled spot) and Se(100) (squared spot) planes, respectively. Another SEAD pattern was recorded from the tip of Se nanowire and shown in the up-right corner of Figure 4.31B, the diffraction spots are, however, hard to be indexed due to the overlap of planes caused by Se, or Ag@Ag₂Se, or their mixtures.^[181]

To gain insights of the Se nanostructures, an HREM image was taken from one individual Se nanowire (Figure 4.31B) and displayed in Figure 4.31C. The strong contrast in the tip is caused by two possibilities: (i) the larger particle size of ~50 nm in diameter, and (ii) higher atomic density of Ag₂Se and Ag than that of Se. To observe clearly, two squared parts in the HRTEM image (Figure 4.31C) were enlarged and displayed in Figure 4.31D and E. The fringe spacings of 0.218 nm and 0.309 nm (Figure 4.31D) are consistent with Se(110) and Se(101) planes of hexagonal selenium in the

standard card ($a= 0.437$ nm, $c= 0.495$ nm, JCPDS no. 06-362).^[183] Through careful measurements and comparison, the fringe spacing of 0.337 nm (Figure 4.31E) is consistent with (111) plane of orthorhombic Ag_2Se in the standard card ($a= 0.434$ nm, $b= 0.707$ nm, and $c= 0.775$ nm, JCPDS no. 20-1063).^[183]

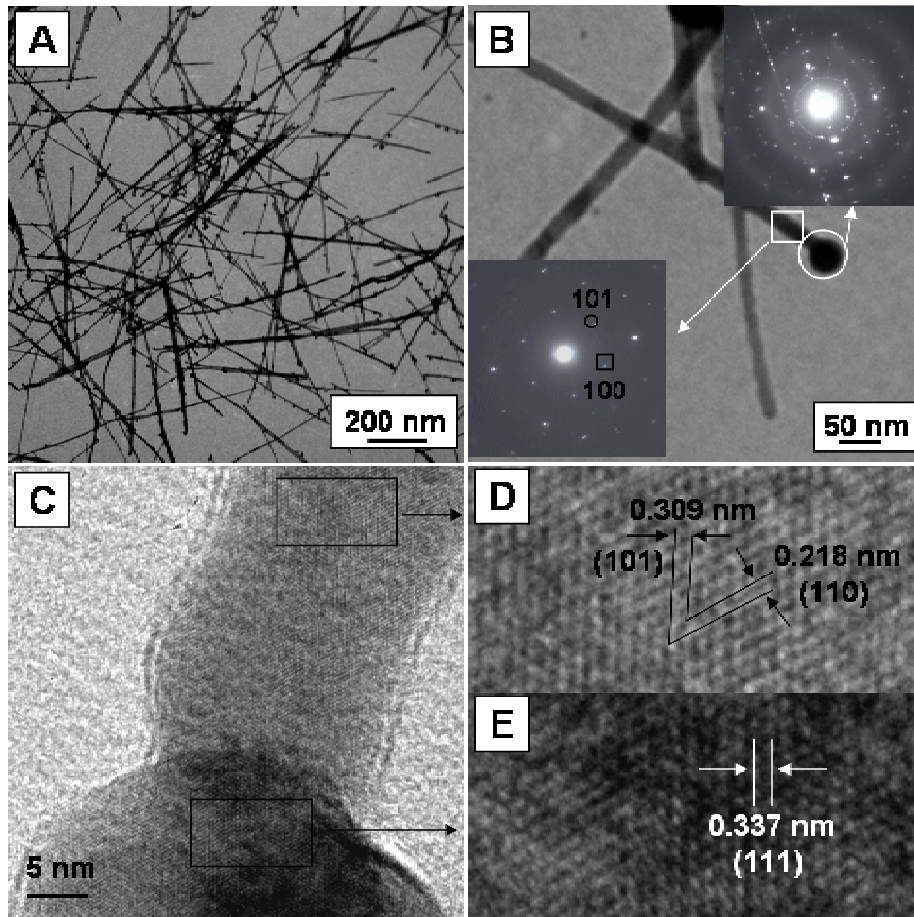


Figure 4.31 TEM image of Se nanowires (A), one individual Se nanowire and the SAED patterns from different parts (B), HRTEM image of the Se nanowire shown in Figure 4.31B (C), and the enlarged HRTEM images from two squared parts of the Se nanowire (D and E).^[181, 183]

It can be noted that the Se nanowires did not grow straight but bended. The TEM and HRTEM images below were used to understand further on this bended structure. As shown in Figure 4.32B, the misalignment of Se atoms is obvious long the direction $d1$

and d_2 with a bending angle of approximately 15° . Therefore the zigzag structure could be produced due to the multiple misalignments along the growth direction of nanowires as seen from Figure 4.32A. Hence it is clear that the atomic dislocation along c-axis is the answer to this bended structure. ^[183]

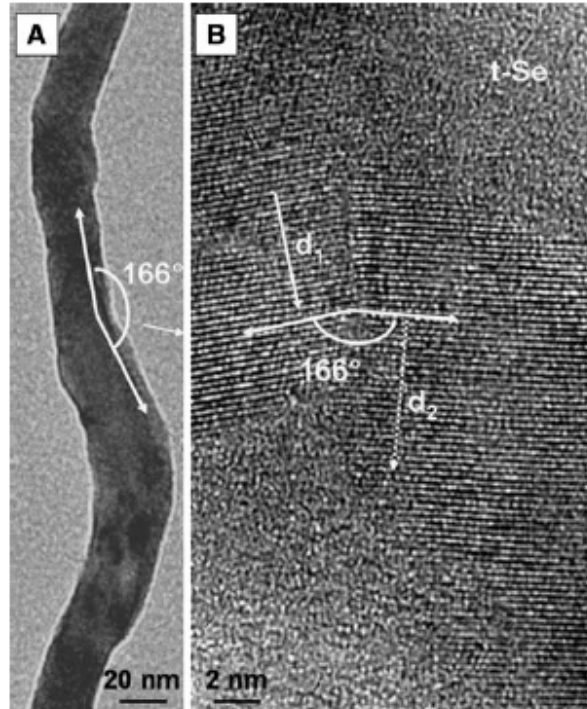


Figure 4.32 (A) TEM image of an individual bending Se nanowire; and (B) its HRTEM with a bending angle of $\sim 15^\circ$. ^[183]

4.3.2 Composition

The composition of the as-synthesized sample was confirmed using X-ray powder diffraction (XRD) and energy dispersive X-ray spectroscopy (EDS). In the XRD pattern (Figure 4.33A), the sharp and strong diffraction peaks can be readily indexed to the hexagonal phase of selenium, which is consistent with the values ($a=0.437$ nm, $c=0.495$ nm) given in the standard card (JCPDS no. 06-362). ^[184] It is worth noting that the abnormal intensity ratio between (100) and (101) planes is bigger than the conventional value (1.3 versus 0.55). This clearly reveals that the t-Se nanowires synthesized in this case are abundant in {100} facets that is parallel to the helical chains of Se atoms (c-axis). ^[183]

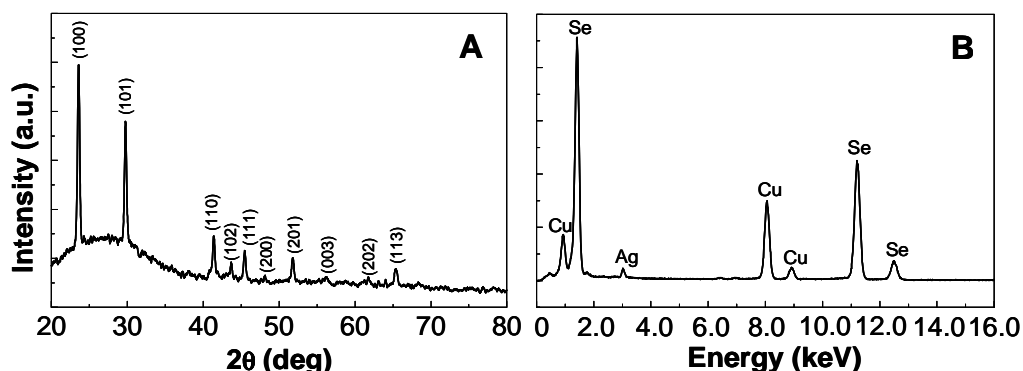


Figure 4.33 The XRD (A) and EDS (B) patterns of the as-prepared Se nanowires. ^[183]

In addition, no diffraction peaks of silver or silver selenide were observed in the XRD pattern (Figure 4.33A). This is probably caused by their small proportions in the final product or overlap of diffraction peaks. In this system, the initial molar ratio of Ag to SeO_3^{2-} is $\sim 1/100$. Fortunately, the EDS analysis pattern collected from the sample deposited on TEM grid reveals that the nanowires are composed of major Se atoms and very minor Ag atoms (Figure 4.33B). The peak of Ag atom is caused by Ag and/or Ag_2Se nanoparticles based on the above discussions. This is also evidenced by the optical absorption spectra before and after Se nanowires formed in aqueous solution (Figure 4.34). ^[183]

4.3.3 Optical Properties

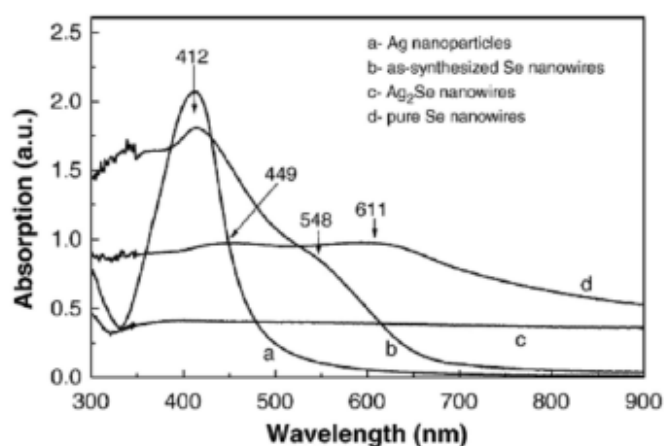


Figure 4.34 UV-vis spectra of Ag nanoparticles (a), the as-synthesized Se nanostructures (b), Ag_2Se nanowires (c), and pure Se nanowires (d). ^[183]

Comparing with Ag nanoparticles (Figure 4.34 curve a), the as-synthesized sample displays two plasmon resonances centered at around 548 nm and 412 nm (Figure 4.34 curve b), respectively, in which the 412-nm plasmon resonance was probably contributed by both Ag nanoparticles and Se nanowires. This could also be confirmed by the plasmon resonances of Ag₂Se nanostructures (Figure 4.34 curve c) and pure Se nanowires (Figure 4.34 curve d) that were synthesized by following the procedures in literature.^[179, 185]

4.3.4 Effects of various parameters

4.3.4.1 Metal Nanoparticles

Different metal nanoparticles (e.g., Au, Ag, Cu, Pt, and Pd) were tested in order to recognize the role of metal nanoparticles itself in the growth mechanism. Figure 4.35 below shows the product as well as their corresponding selenium nanostructures. As can be seen from the TEM images above, the size and morphology of the nanoparticles are quite different from one another but all are nearly spherical in shape. The diameter of the nanoparticles are varied from Au (10 ± 2 nm in diameter, Figure 4.35A), Cu (5–25 nm in diameter, Figure 4.35B), Pt (~5 nm in diameter, Figure 4.35C), until Pd (12 ± 2 nm in diameter, Figure 4.35D). For both Pt and Pd nanoparticles, it is clearly seen that there is tendency to aggregate unlike Au and Cu nanoparticles which exist independently.^[183]

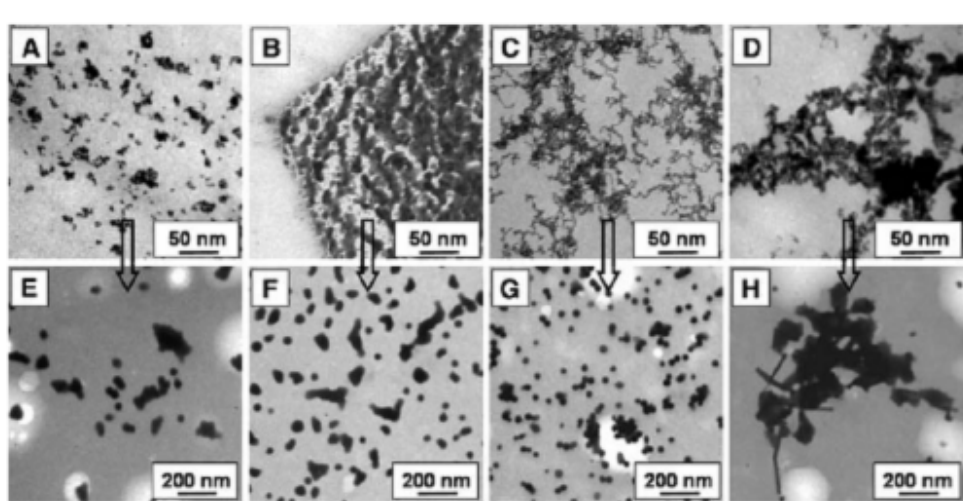


Figure 4.35 TEM images of metal nanoparticles: (A) Au; (B) Cu; (C) Pt; and (D) Pd; and the corresponding selenium nanostructures induced by metal nanoparticles: (E–H).^[183]

Overall when these nanoparticles used to generate Se nanostructures, the obtained results were sort of spherical Se nanostructures with diameter of 100 nm. See Figure 4.35 E-G. Contrary for Pd particles, under exactly same condition only few Se nanorods form, which is believed to occur due to these following ideas:

- (i) no metal selenides formed (e.g., Au_2Se_3 , CuSe , PtSe , or PdxSe_y) under the current conditions, and
- (ii) the lattice mismatch between hexagonal selenium and such metal and/or metal selenides.

4.3.4.2 Shape of Silver Nanoparticles

For the purpose of further investigation, different shapes and size of Ag nanoparticles were also tested to strengthen this result. They were colloids, spheres, and/or plates and sizes ranging from ~15, ~45, up to ~100 nm in diameters. Figure 4.36 shows the TEM images of the size-reduced silver nanoparticles due to the N_2H_4 etching, sizes are varied ranging from the large ones (over 100 nm, Figure 4.36A) to nearly spherical particles with diameter of ~80 nm (Figure 4.36B), and then to small ones with diameter of ~45 nm (Figure 4.36C). It was found that the 45-nm silver nanoparticles to be the most suitable for the growth of selenium nanowires with average diameter of ~25 nm (Figure 4.36D). Then Ag nanoplates (edge length of ~50 nm) and small Ag colloids (~15 nm in diameter) were used to investigate such an induced growth.

The representative TEM image of the Ag nanoplates, with the corresponding Se nanostructures was displayed in Figure 4.37A showing a flat structure and the diameter of ~26 nm in the middle (Figure 4.37B). As the magnification became higher the flat nanowires turned slim gradually distant from the rooted nanoplates that is shown by inset of Figure 4.37B. The growth of nanowires diameter of around 25 nm (Figure 4.37D) could also be induced by small silver colloids but no tips were observed at the end of nanowires. This is due to its smaller size when compared to the diameter of selenium nanowires. Therefore it is revealed that the silver nanoparticles holds an important role in the crystallization and growth of selenium nanowires without any heating and/or sonication. ^[183]

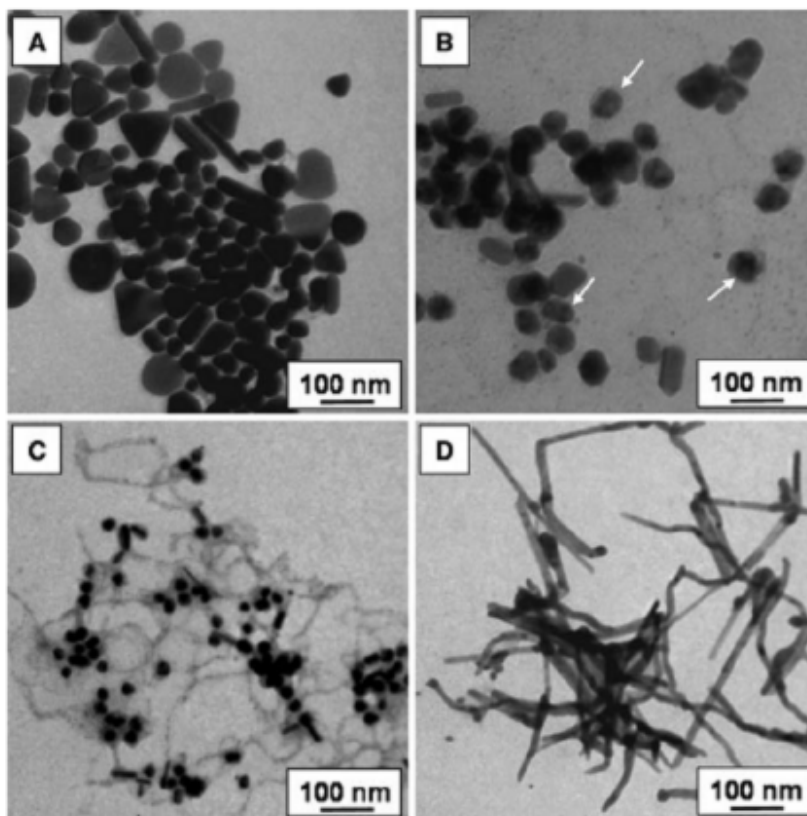


Figure 4.36 (A) TEM images of multiple-shape silver nanoparticles; (B) and (C) the etched silver particles by hydrazine; and (D) the corresponding Se nanowires induced by the freshly formed silver nanoparticles. ^[183]

The shapes and sizes of selenium nanostructures were checked at different stages for the purpose of learning the time-dependent growth. The color of solution gradually changed to light brown and over hours of ageing turned to dark brown after appropriate amount of hydrazine and selenious acid addition to the homogeneous aqueous mixture containing silver nanoparticles. Figure 4.38 shows the TEM images of selenium nanostructures obtained at different stages. As a result, the length of the selenium nanostructures increases from ~30 nm (Figure 4.38A) to ~200 nm (Figure 4.38B), and up to a few micrometers (Figure 4.38C) over aging for around 3, 24, and 48 h, respectively. On the other hand, the diameter of the nanowires shifts a little from ~12 to ~25 nm even after aging for 48 h under current conditions. This implies that selenium atomic grow preferentially along c-axis when compared to a-axis. ^[183]

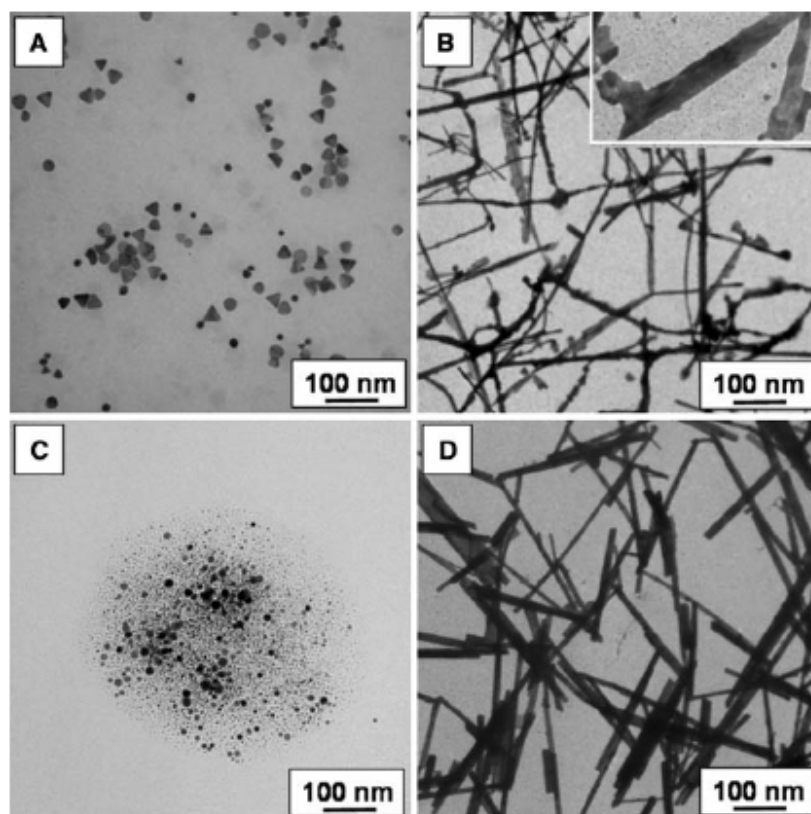


Figure 4.37 (A) TEM image of silver nanoplates; (B) the corresponding slim Se nanobelts and a high magnification inset of image (B); (C) small silver nanoparticles; and (D) the corresponding Se nanowires. ^[183]

4.3.4.3 Induced reaction time

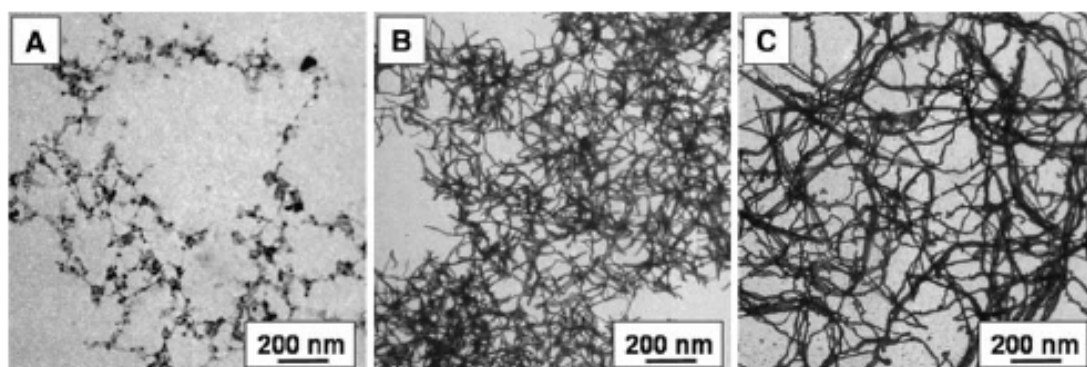


Figure 4.38 TEM images of time-dependent growth of selenium nanostructures at different stages: (A) 3 h; (B) 24 h; and (C) 48 h. ^[183]

4.3.4.4 Molar ratios of Ag^0 to SeO_3^{2-} ions

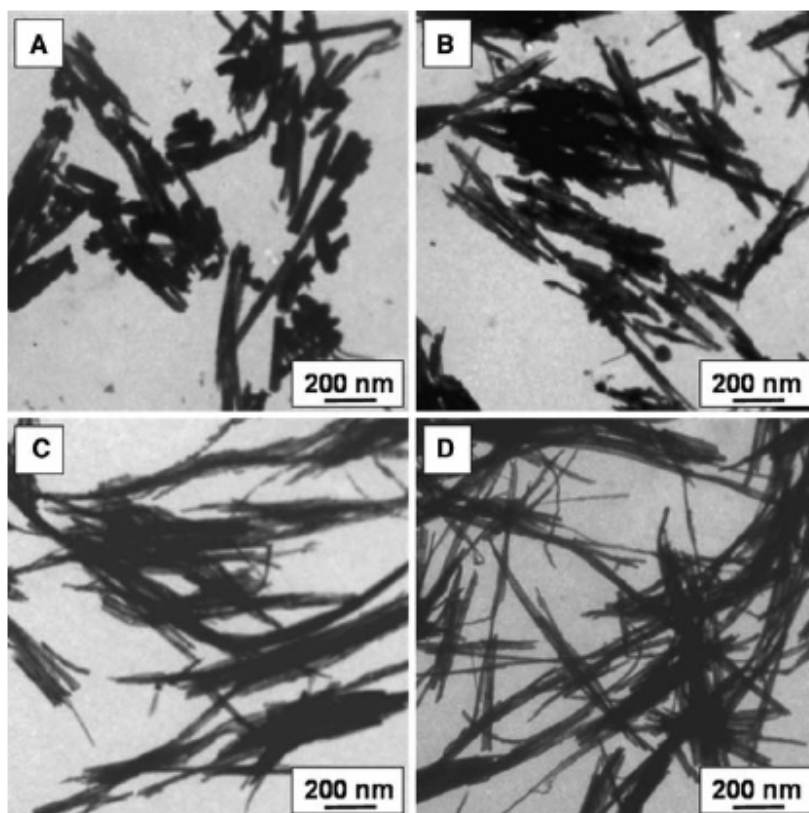


Figure 4.39 TEM images showing the influence of the molar ratios of silver to selenium ions on the formation of Se nanostructures: (A) 1/4,000; (B) 1/800; (C) 1/230; and (D) 1/115. ^[183]

The influence of the amount of silver on the growth was also examined, by adding different molar ratios of silver colloids (diameter of ~15 nm) to selenious acid such as 1/4,000, 1/800, 1/230, and 1/115. Based on the experimental results, it indicates that the rate of solution color change is dependent upon the amount of the silver colloids. After aging for ~48 h, all the four samples turned brown and some precipitates were observed at the bottom of the vial.

The dimension of the final products was predicted by TEM techniques. As seen from Figure 4.39, with increasing the amount of silver colloids the diameters of the nanowires/rods decrease from ~80 nm (1/4,000, Figure 4.39A) to ~50 nm (1/800, Figure

4.39B), to ~30 nm (1/230, Figure 4.39C), and to ~25 nm (1/115, Figure 4.39D). In the same way, the length of selenium nanowires increases with increasing silver colloids. The results reveal that: ^[183]

- (i) in aqueous solution and at room temperature even a very small amount (e.g., 1/4,000) of Ag nanoparticles can successfully induce the crystallization and growth of selenium nanostructures, and
- (ii) the more silver colloids added, the more nucleation sites available hence the smaller the diameter of nanowires formed.

The optical absorption measurement (Figure 4.40) was done to support the study of influence of the molar ratio of silver to selenious ions on the growth of Se nanostructures because the basic idea is that different molar ratios could lead to different nanostructures with different surface plasmon resonances. As illustrated by the graph on Figure 4.40, when the concentration of SeO_3^{2-} ions is high (e.g., 1/4,000 and 1/800), the surface plasmon resonances of the selenium nanostructures are not apparent in the absorption spectra (Figure 4.40 curves a and b). ^[183]

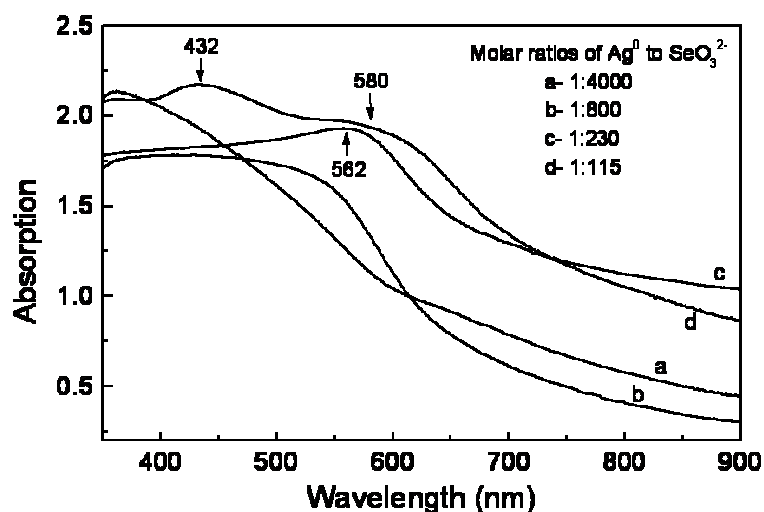


Figure 4.40 UV-vis spectra of Ag-Se nanoparticles with different molar ratio Ag to Se (a) 1/4000, (b) 1/800, (c) 1/230 and (d) 1/115. ^[183]

On the other hand when the concentration of SeO_3^{2-} was reduced a plasmon resonance corresponding to the selenium nanowires emerges and is centered at ~562 nm (Figure 4.40 curve c). Moreover when the concentration of Se lowered to 115:1 to Ag two peaks

are observed centered at 432 and 580 nm (curve d) respectively. This idea is consistent with the literature (Mayers et al. 2003).^[186] In addition, the peak of selenium nanostructures gradually shifts to longer wavelengths to 580 nm from ~350 nm as less amount of Se added, which suggests that the higher molar ratios of Ag to SeO_3^{2-} and the more favorable for the well-crystallized Se nanowires formed at the discussed condition.^[183]

4.3.5 Growth Mechanism

To understand the growth mechanism of the 1-D Se nanostructures, it is necessary to make clear what role the silver nanoparticles play in this system. Xia et al.^[187] suggested that the plausible formation mechanism of crystalline Ag_2Se is mainly related to the lattice match between t-Se and orthorhombic- Ag_2Se by reacting silver nanowires with a dispersion containing α -Se colloids, or reacting Se nanowires with AgNO_3 solution. Although the systems considered differ, this mechanism appears to be applicable to the formation of t-Se nanowires in this work. Citric acid ($\text{C}_6\text{H}_8\text{O}_7$) could reduce SeO_3^{2-} ions to Se0 atoms in aqueous solution, and they could react with the surface silver atoms of silver nanoparticles to form Ag_2Se surrounding Ag particles.^[183]

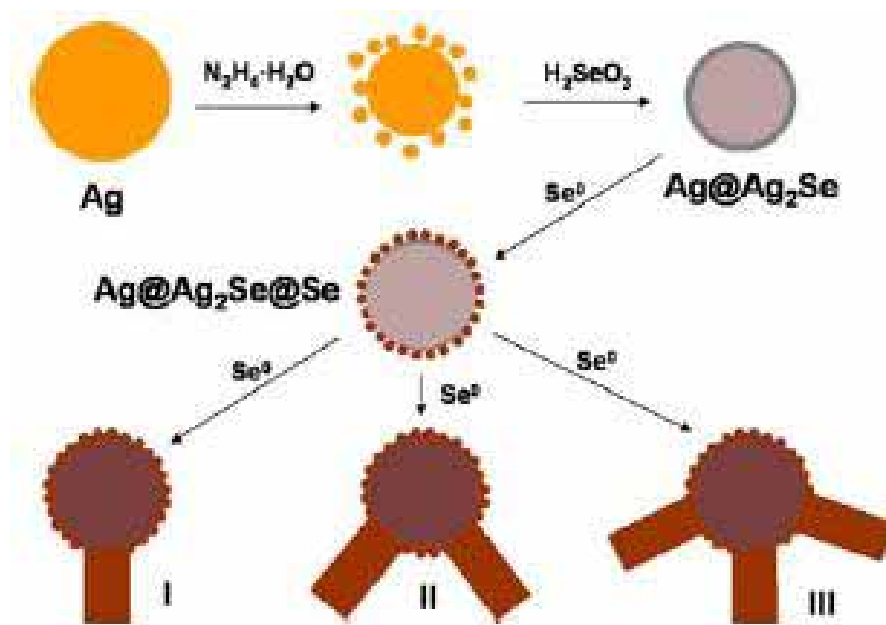


Figure 4.41 Schematic diagram illustrating the growth mechanism of Se nanowires induced by silver nanoparticles.^[183]

More interestingly, we found that the Ag_2Se particles did not prevent the further reaction with Se atoms, and contrarily they may provide multiple sites for nucleation of Se atoms. To reduce total surface free energy, the Se atoms prefer to stack along one direction, especially the helical chains of Se atoms (c-axis) to form Se nanowires. The growth direction of Se nanowires on the surface of Ag_2Se nanoparticles is probably determined by the match of lattice constants between hexagonal Se ($a=0.437$ nm) and orthorhombic- Ag_2Se ($a=0.434$ nm) or between hexagonal Se ($c=0.495$ nm) and tetragonal- Ag_2Se ($c=0.498$ nm) in their topological structures. For the orthorhombic or tetragonal- Ag_2Se , the lattice constant in the a- or c-axis of t-Se was perfect for coordination with that of Ag_2Se during the formation of t-Se nanowires. That is, Ag_2Se particles acted as a bridge in forming Se nanowires in this system. Summarizing the above discussions, the growth process of t-Se nanowires in aqueous media can be schematically illustrated in Figure 4.41.^[183]

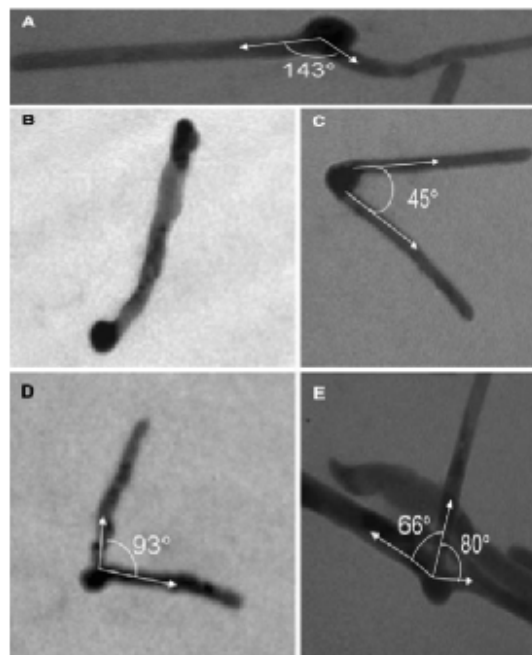


Figure 4.42 TEM images of the as-synthesized Se nanostructures rooted on the surface of $\text{Ag}_2\text{Se}/\text{Ag}$ nanoparticles along one, two or more directions.^[183]

There is tendency of the Se atoms to stack along one or two or more directions on the surface of $\text{Ag}_2\text{Se}/\text{Ag}$ particles. This Figure 4.41 was designed based on the TEM images obtained (Figure 4.42), which can be seen different angles formed between two growth

directions, they are $\sim 143^\circ$ (A), $\sim 45^\circ$ (B), $\sim 93^\circ$ (C), $\sim 66^\circ$ (D) and $\sim 80^\circ$ (E). The reason to this particular numbers is mainly due to the stability purpose in the whole system in the growth process. ^[183]

It is proven that the selenium atom bond with the surface atoms of silver particles in order to produce silver selenide at the beginning and the next step was the selenium atom nucleation and epitaxially growth along c-axis of selenium nanowires on Ag/Ag₂Se particles. ^[183] They would be potentially applied in photoconductors, anisotropic thermoconductors, and nonlinear optical responses. This method would be useful for generating 1-D nanostructures with similar lattice parameter(s) as the results could be helpful for design and construction of nanostructures with comparable lattice parameter(s). ^[183]

4.3.6 Conclusions

This work demonstrated a new synthesis method, silver induced growth approach, for generating crystalline t-Se nanowires in aqueous media at RT although different metals such as Au, Cu, Pt and Pd could be used. However, Ag is the most favorable. By this method, single crystalline t-Se nanowires were successfully synthesized with the diameter of around 23 nm and length over hundreds of nanometers. Different from the previous methods, ^[185, 188-200] this method has advantages that it uses no stabilizers, no sonichemical processes, no toxic reducing agents (e.g. NaBH₄, N₂H₄), and all operations can be conducted in aqueous solution and at RT. More interestingly, the transformation of amorphous α -Se to crystalline t-Se could be successfully achieved by using silver nanoparticles as an inducer in water and at RT. The α -Se nanowires display highly crystalline quality and interesting anisotropic growth property. ^[183] There are several factor affecting the growth of Se nanowires, they are the shape/size of silver nanoparticles, the induced reaction time and the molar ratio of silver to selenious acid. ^[183]

CHAPTER 5

Conclusions and Future Work

This work of thesis has been greatly devoted to the study of noble metal nanoparticles, focusing on the synthesis, growth mechanisms and functional applications of gold and silver nanoparticles. The main findings can be summarized as below.

(i) Gold worm-like nanoparticles are prepared by treating an aqueous solution of chloroauric acid with sodium citrate and poly (vinyl pyrrolidone) (PVP). By using this environment friendly method, one new kind of gold nanostructures, i.e., worm-like nanoparticles, are achieved with dominant sides being {110} facets and with growth direction along [001]. Sizes of the worm-like nanoparticles varies depending on the parameters, they are up to 20 nm in width and up to 60 nm in length. These worm-like nanoparticles in practice can be used for ionic sensing detection of S^{2-} ions and others with sulphur groups.

(ii) Silver nanoplates are prepared by a newly developed self-seeding coreduction hydrochemical method. By this method, triangular silver nanoplates and circular silver nanodiscs have been achieved with thickness of ~2.3 nm. Such nanoplates show unique properties including, high extinction coefficient in the NIR region and high surface-to-volume ratios, which will make them useful in optical sensors, NIR absorbers, catalysts or biosensors.

(iii) The formation of selenium nanowires is induced by silver nanoparticles (plates, spheres and colloids), and no specific requirements are needed such as no use of stabilizers, no sonochemical processes, no toxic reducing agents, and all experiments carried at room temperature. Such well-crystallized selenium nanowires could be found many potential applications in photoconductors, anisotropic thermoconductors, and nonlinear optical responses.

(iv) Theoretical methods, e.g., MD and DFT, have been used to improve the fundamental understanding of the shape-controlled mechanisms of particle growth. The binding energies calculated based on DFT could provide atomic interaction information, and MD simulations could offer the understanding at a molecular level.

These research findings summarized in this section will be useful for the shape controlled synthesis and growth of metal nanoparticles for potential applications. However, some limitations or problems in the shape control of gold, silver nanoparticles, and silver induced selenium nanowires still exist, although much more efforts have been made to improve the quality in uniform size and shape. The future work extended to this research will focus on the monodispersed nanoparticles with anisotropic morphologies for obtaining specific or unique functional properties, and some attempts will also be devoted to apply these nanoparticles for optical probes, ionic sensing detection in practical uses and industries.

CHAPTER 6

References

1. Lee, Y.H., et al., *Materials Chemistry and Physics*, 2006. **100**: p. 85-91.
2. Kemal, L., et al., *J. Phys. Chem. C*, Submitted 2008.
3. Daniel, M. and D. Astruc, *Chem. Rev.* 2004. p. 293-346.
4. Kreibig, U., *Handbook Opt. Properties*, 1997. **2**: p. 145.
5. Kreibig, U. and L. Genzel, *Surf. Sci.*, 1985. **156**: p. 678.
6. Hulst, H.C.v.d., *Light Scattering by Small Particles*. John Wiley and Sons, 1957.
7. Kerker, M., *The Scattering of Light and Other Electromagnetic Radiation*. Academic Press, 1969.
8. Bohren, C.F. and D.R. Huffman, *Absorption and Scattering of Light by Small Particles*. Wiley, 1983.
9. Kreibig, U., *J. Phys. F: Met. Phys.*, 1974. **4**: p. 999.
10. Kreibig, U., *Z. Phys*, 1978. **31**: p. 39.
11. Felidj, N., J. Aubard, and G. Levi, *J. Chem. Phys.*, 1999. **111**: p. 1195.
12. Kelly, K.L., et al., *J. Phys. Chem. B*, 2003. **107**: p. 668.
13. Purcell, E.D. and C.R. Pennypacker, *Astrophys. J.*, 1973. **186**: p. 705.
14. Draine, B.T. and P.J. Flatau, *Opt. Soc. Am. A*, 1994. **11**: p. 1491.
15. Yang, W.H., G.C. Schatz, and R.P.V. Duyne, *J. Chem. Phys.*, 1995. **103**: p. 869.
16. Pérez-Juste, J., et al., *Coordination Chemistry Reviews*, 2005. **249**: p. 1870-1901.
17. Genzel, L., T.P. Martin, and U. Kreibig, *Z. Phys*, 1975. **21**: p. 339.
18. Mie, G., *Ann. Phys*, 1908. **25**: p. 377.
19. Palik, E.D. and (Ed.), *Handbook of Optical Constants of Solids*. Academic Press, 1985.
20. Gans, R., *Ann. Phys*, 1912. **37**: p. 881.
21. Ruppin, R., *J. Opt. Soc. Am. B*, 1989. **6**: p. 1559.
22. Ruppin, R., *J. Phys. D*, 1990. **23**: p. 757.
23. Fuchs, R., *Phys. Rev. B*, 1975. **11**: p. 1732.
24. Al-Rawashdeh, N.A.F., et al., *J. Phys. Chem. B*, 1988. **102**: p. 361.

25. Ruppin, R., J. Phys.: Condens. Matter, 1998. **10**: p. 7869.
26. Draine, B.T. and J.J. Goodman, Astrophys. J. , 1993. **405**: p. 685.
27. Draine, B.T. and P.j. Flatau, *Program DDSCAT*. Scripps Institute of Oceanography, University of California, San Diego, C. A.
28. Stookey, S.D. and R.J. Araujo, Appl. Opt., 1968. **7**: p. 777.
29. Foss Jr., C.A., et al., J. Phys. Chem., 1994. **98**: p. 2963.
30. Su, Y.Y., S.S. Chang, and C.L. Lee, J. Phys. Chem. B, 1997. **101**: p. 6661.
31. Link, S., M.B. Mohamed, and M.A. El-Sayed, J. Phys. Chem. B, 1999. **103**: p. 3073.
32. VanderZande, B.M.I., et al., Langmuir, 2000. **16**: p. 451.
33. Pérez-Juste, J., et al., Adv. Funct Mater., 2004. **14**: p. 571.
34. Yan, B., Y. Yang, and Y. Wang, J. Chem. Phys. B, 2003. **107**: p. 9159.
35. Weaver, J.H., et al., *Optical Properties of Metals. Physics Data Series, Fachinformationszentrum, Karlsruhe*. 1981.
36. Zhu, J. and Jin, X.L., .Superlattices and Microstructures, 2007. **41**: p. 271-276.
37. Wilson, O., G.J. Wilson, and P. Mulvaney, Adv. Mater, 2002. **14**: p. 1000.
38. Link, S. and M.A. El-Sayed, Int. Rev. Phys. Chem., 2000. **19**: p. 409.
39. Link, S. and M.A. Al-Sayed, Annu. Rev. Phys. Chem, 2003. **54**: p. 331.
40. Esley, G.L., Phys. Rev. Lett., 1983. **51**: p. 2140.
41. Esley, G.L., Phys Lett. Rev. B. , 1986. **33**: p. 2144.
42. Groeneveld, R.H.M., R. Sprik, and A. Lagenduk, Phys Lett. Rev. B., 1992. **45**: p. 5079.
43. Groeneveld, R.H.M., R. Sprik, and A. Lagenduk, Phys. Rev. B, 1985. **51**: p. 11433.
44. Schoenlein, R.W., et al., Phys Lett. Rev., 1987. **58**: p. 1680.
45. Brorson, S.D., J.G. Fujimoto, and E.P. Ippen, Phys Lett. Rev., 1987. **59**: p. 1962.
46. Sun, C.K., et al., Phys Rev. B, 1993. **48**: p. 12365.
47. Sun, C.K., et al., Phys Rev. B, 1987. **50**: p. 15337.
48. delFatti, N., et al., Phys. Rev. Lett., 1998. **81**: p. 922.
49. Elsayed-Ali, H.E., et al., Phys. Rev. B, 1991. **43**: p. 4488.
50. Juhasz, T., et al., Phys. Rev. B, 1992. **45**: p. 13819.

51. Juhasz, T., et al., Phys. Rev. B, 1993. **48**: p. 15488.
52. Fann, W.S., et al., Phys. Rev. B, 1992. **46**: p. 13592.
53. Fann, W.S., et al., Phys. Rev. Lett., 1992. **68**: p. 2834.
54. Schmuttenmaer, C.A., et al., Phys. Rev. B, 1994. **50**: p. 8957.
55. Aeschlimann, M., et al., J. Chem. Phys., 1995. **102**: p. 8606.
56. Gao, Y., et al., Phys. Rev. B, 1997. **56**: p. 1099.
57. Cao, J., et al., Phys. Rev. B, 1998. **58**: p. 10948.
58. Kreibig, U. and C.Z.V. Fragstein, Phys., 1969. **224**: p. 307.
59. Kreibig, U., Z. Phys., 1970. **234**: p. 307.
60. Zhou, W.L., et al., J. Appl. Phys., 2003. **93**: p. 7340.
61. Ahmadi, T.S., et al., J. Phys. Chem., 1997. **101**: p. 3713.
62. Hodak, J.K., I. Martini, and G.V. Hartland, J. Phys. Chem., 1998. **102**: p. 6958.
63. Perner, M., et al., Ultrafast Phenomena X, 1966.
64. Perner, M., et al., Phys. Rev. Lett., 1997. **78**(11): p. 2192.
65. Perner, M., T. Klar, and U. Lemmer, J. Lumin, 1998. **76-77**: p. 181.
66. Hodak, J.K., M. I., and G.V. Hartland, J. Phys. Chem. Lett., 1998. **284**: p. 135.
67. Hodak, J.K., I. Martini, and G.V. Hartland, J. Phys. Chem., 1998. **108**: p. 9210.
68. Hodak, J.K., A. Henglein, and G.V. hartland, J. Chem. Phys., 1999. **111**: p. 8613.
69. Link, S., et al., Phys. Rev. B, 2000. **61**(9): p. 6086.
70. Link, S., et al., J. Chem. Phys., 1999. **111**: p. 1255.
71. Ahmadi, T.S., S. Logunov, and M.A. El-Sayed, J. Phys. Chem., 1996. **100**: p. 8052.
72. delFatti, N., et al., Appl. Phys. B, 1999. **68**: p. 433.
73. Wang, Z.L., M.B. Mohamed, and S. Link, Surf. Sci., 1999. **440**: p. 809.
74. Rosei, R., F. Antongeli, and U.M. Grassano, Surf. Sci., 1973. **37**: p. 689.
75. Cardona, M., et al., *Modulation Spectroscopy, Solid State Physics, Supplement II*. 1969.
76. Ashcroft, N.W. and N.D. Merwin, *Solid State Physics*. Saunders College: Philadelphia, PA, 1976.
77. Pines, D. and P. Nozieres, *The Theory of Quantum Liquids*. Benjamin : New York, 1966.

78. delFatti, N., C. Voisin, and F. Vallee, *J. Chem. Phys.*, 1999. **110**: p. 11484.
79. Gao, P.X., Y. Ding, and Z.L. Wang, *Nano Lett.*, 2003. **3**: p. 1315.
80. Hamanaka, Y., N. Hayashi, and A. Nakamura, *J. Lumin.*, 1998. **76-77**: p. 221.
81. Smith, B.A., et al., *Chem. Phys. Lett.*, 1997. **270**: p. 139.
82. Stella, A., et al., *Phys. Rev. B*, 1996. **53**(23): p. 15497.
83. Stella, A., et al., *Ultrafast Phenomena X*. Springer: Berlin, Germany, 1996.
84. Nisoli, M., S. Stagira, and S.D. Silvestri, *Phys. Rev. B*, 1997. **78**: p. 3575.
85. Belotskii, E.D. and P.M. Tomchuk, *International Journal of Electronics*, 1992. **73**(5): p. 955-957.
86. Coombes, C.J., *J. Phys.*, 1972. **13**: p. 2287.
87. Castro, T., et al., *Phys. Rev. B*, 1990. **42**: p. 8548.
88. Beck, R.D., et al., *Science*, 1991. **253**(879).
89. Martin, T.P. and W.A. Jesser, *J. Chem. Phys.*, 1990. **100**: p. 2322.
90. Schmid, G. and E. K. J. Klabunde, *Metals In Nanoscale Materials in Chemistry*. Wiley Interscience: New York, 2001(2): p. 15.
91. Alivisatos, A.P., *J. Phys. Chem.*, 1996. **100**: p. 13226.
92. Couchman, P.R. and W.A. Jesser, 269, 1977(481).
93. Ecrolessi, F., W. Andreoni, and E. Tosatti, *Phys. Rev. Lett.*, 1991. **66**: p. 911.
94. Klein, D.L., P.L. McEuen, and J.E.B. Katari, *Appl. Phys. Lett.*, 1996. **68**: p. 2574.
95. Black, C.T., D.C. Ralph, and M. Tinkham, *Phys. Rev. Lett.*, 1996. **76**(688).
96. Ingram, R.S., M.J. Hostetler, and R.W. Murray, *J. Am. Chem. Soc.*, 1997. **119**: p. 9279.
97. Andres, R.P., et al., *Science*, 1996. **272**: p. 1323.
98. Mukherjee, B. and N. Ravishankar, *Nanotechnology*, 2007. **18**(2): p. 025603.
99. Kim, F., J.H. Song, and P. Yang, *J. AM. Chem. Soc.*, 2002. **124**: p. 14316-14317.
100. Chang, S.S., et al., *Langmuir*, 1999. **15**: p. 701.
101. Tsuji, M., et al., *Materials Letter*, 2005. **59**: p. 3856-3860.
102. Tsuji, M., et al., *Materials Letter*, 2004. **58**: p. 2326-2330.
103. Pan, A.L., H.G. Zheng, and Z.P. Yang, *Materials Research Bulletin*, 2003. **38**: p. 789-796.

104. Long, D., G. Wu, and S. Chen, *Radiation Physics and Chemistry*, 2007. **76**: p. 1126-1131.
105. Li, C., et al., *J. Phys. Chem. B*, 2006. **110**: p. 1546-1552.
106. Shao, Y., Y. Jin, and S. Dong, *Chem. Commun.*, 2004: p. 1104-1105.
107. Burda, C., et al., *Chem. Rev.*, 2005. **105**: p. 1025-1102.
108. Liu, J., et al., *Adv. Colloid Interface Sci.*, 1996. **69**: p. 131.
109. Tanori, J. and M.P. Pileni, *J. Phys. Chem. B*, 1997. **105**: p. 5643.
110. Lin, K.-N., et al., *China Particuology*, 2007. **5**: p. 237-241.
111. Link, S. and M.A. El-Sayed, *Int. Rev. Phys. Chem.*, 2000. **19**: p. 409.
112. Germain, V., et al., *J. Phys. Chem. B*, August 28, 2003. **107**: p. 8717-8720.
113. Salem, A.K., P.C. Searson, and K.W. Leong, *Nature Materials*, 2003. **2**: p. 668-671.
114. Wiley, B., et al., *MRS Bullentin*, 2005. **30**: p. 356-361.
115. Xia, Y. and N.J. Halas, *MRS Bulletin*, 2005. **30**: p. 338-347.
116. Li, Y. and M.A. El-Syaed, *J. Phys. Chem. B*, 2001. **105**: p. 8938-8943.
117. Johnson and F.G. Brian, *Top. Catal.*, 2003. **24**((1-4)): p. 147.
118. Zhou, M., et al., *Chemistry Letters*, 2005. **34**(12): p. 1670-1671.
119. Iwanaga, H., et al., *J. Cryst. Growth*, 1994. **474**: p. 234-238.
120. Hu, H., et al., *Phys. Rev. E.*, 2000. **62**: p. 4318.
121. Jana, N.R., L. Gearheart, and C.J. Murphy, *J. Phys. Chem. B*, 2001. **105**: p. 4065-4067.
122. Murphy, C.J. and N.R. Jana, *Adv. Mater*, 2002. **14**: p. 80-82.
123. Germain, V., et al., *J. Phys. Chem. B*, 2003. **107**(34): p. 8717-8720.
124. Maillard, M., G. Giorgio, and M.P. Pileni, *Adv. Mater.*, 2002. **14**: p. 1084-1086.
125. Lofton, C. and W. Sigmund, *Adv. MFunc. Mater.*, 2005. **15**: p. 1197-1208.
126. Mulvaney, P., et al., *Plasmonics*, 2006. **1**: p. 61-66.
127. Chen, S., et al., *J. Am. Chem. Soc.*, 2003. **125**: p. 16186-16187.
128. Jiang, X., et al., *Adv. Mater.*, 2003. **15**: p. 1740.
129. Jun, Y.W., et al., *J. Am. Chem. Soc.*, 2001. **125**: p. 16186-16187.
130. Brioude, A., X.C. Jiang, and M.P. Pileni, *J. Phys. Chem. B*, 2005. **109**: p. 13138-13142.

131. Jiang, X.C. and M.P. Pileni, *Colloid Interface A: Physichem. Eng-Aspects*, 2007. **295**: p. 228-232.
132. Jiang, X.C., A. Brioude, and M.P. Pileni, *Colloid Interface Sci A*, 2006. **277**: p. 201-206.
133. Jiang, X.C., Q.H. Zeng, and A.B. Yu, *Nanotechnology*, 2006. **17**: p. 4929-35.
134. Halder, A. and N. Ravishhankar, *Adv. Mater.*, 2007. **17**: p. 1854-1858.
135. Jiang, X.C., Q.H. Zeng, and A.B. Yu, *Langmuir*, 2007. **23**: p. 2218-23.
136. Zeng, Q., et al., *Nanotechnology*, 2007. **18**: p. 035708.
137. Chen, S. and D.L. Carroll, *Nano Lett.*, 2002. **2**: p. 1003-1007.
138. Boon, G., et al., *Chem. Phys. Lett.*, 1998. **295**: p. 122-128.
139. Boon, G., et al., *J. Phys. Chem. A*, 2001. **105**: p. 8805-8814.
140. Boon, G., et al., *J. Phys. Chem. A*, 2003. **107**: p. 11120-27.
141. Manna, L., E.C. Scher, and A.P. Alivisatos, *Nat. Mater.*, 2000. **2**: p. 382-385.
142. Peng, Z.A. and X. Peng, *J. Am. Chem. Soc.*, 2001. **123**: p. 183-184.
143. Perdew, J.P. and Y. Wang, *Phys. Rev. B*, 1986. **33**: p. 8800-8802.
144. Balleto, F. and R. Ferrando, *Rev. Mod. Phys.*, 2005. **77**: p. 371-423.
145. Henglein, A., P. Mulvaney, and T. Linnert, *Faraday Discuss*, 1991. **92**: p. 31-44.
146. Henglein, A. and D. Meisel, *Langmuir*, 1998. **14**: p. 8392-7393.
147. Ung, T., et al., *Langmuir*, 1997. **13**: p. 1773-1782.
148. Xia, Y., *MRS Bulletin*, 2005. 30: p. 338-348
149. Jiang, X., Q. Zeng, and A. Yu, *Nanotechnology*, 2006. **17**: p. 4926-4935.
150. Rossen, A.R. and W.C. Carter, *Physics A*, 1998. **261**: p. 232.
151. Livnat, A. and O. Kafri, *Appl. Opt.*, 1983. **22**: p. 3013.
152. Jin, R.C., et al., *Science*, 2001. **294**: p. 1901.
153. Silva, T.J., S. Schultz, and D. Weller, *Appl. Phys. Lett.*, 1994. **65**: p. 658.
154. Schultz, S., et al., *Proc. Natl. Acad. Sci/*, 2000. **97**: p. 996.
155. Maillard, M., S. Giorgio, and M.P. Pileni, *Adv. Mater.*, 2002. **14**: p. 1084.
156. Germain, V., et al., *J. Phys. Chem. B*, 2003. **207**: p. 8717.
157. Hao, E., et al., *J. Am. Chem. Soc.*, 5115. **124**: p. 15182.
158. Jin, R.C., et al., *Nature*, 2003. **18**: p. 8692.
159. Partoria-Santos, I. and L.M. Liz-Marzan, *Nano Lett.*, 2002. **2**: p. 903.

160. Chen, S. and D.L. Carroll, *Nano Lett.*, 2002. **2**: p. 1003.
161. Sun, Y., B. Mayers, and Y. Xia, *Nano Lett.*, 2003. **3**: p. 675.
162. Callegari, A., D. Tonti, and M. Chergui, *Nano Lett.*, 2003. **3**: p. 1565.
163. Yener, D.O., et al., *Langmuir*, 2002. **18**: p. 8692.
164. Sun, Y. and Y. Xia, *Adv. Mater.*, 2002. **14**: p. 833.
165. Pérez-Juste, J., et al., *Coord. Chem. Rev.*, 2005. **249**: p. 1870.
166. Shankar, S.S., et al., *Nat. Mater.*, 2004. **3**: p. 482.
167. Balleto, F. and R. Ferrando, *Rev. Mod. Phys.*, 2005. **77**: p. 371.
168. Nikoobakht, B. and M.A. El-Sayed, *Langmuir*, 2001. **17**: p. 6368.
169. Nikoobakht, B. and M.A. El-Sayed, *Chem. Mater.*, 2003. **15**: p. 1957.
170. Zeng, Q., et al., *Chem. Mater.*, 2003. **108**: p. 41158.
171. Zeng, Q., et al., *Chem. Mater.*, 2003. **15**: p. 4732.
172. Cullity, B.D., S.R. Stock, and S. Stock, *Elements of X-ray diffraction* 2001.
173. Sun, Y. and Y. Xia, *Adv. Mater.*, 2003. **15**: p. 695.
174. Jiang, L., et al., *Inorg. Chem.*, 2004. **43**: p. 5877.
175. Kotz, J.C. and K.F. Purcell, *Chemistry and Chemical Reactivity*. 1991.
176. Gates, B., et al., *Adv. Funct Mater.*, 2002. **12**: p. 219.
177. Ibragimov, N.I., Z.M. Abutalibova, and V.G. Agaev, *Thin Solid Films*, 2000. **359**: p. 125.
178. Greenwood, N.N. and A. Eamshaw, *Chemistry of Elements*, 1997. **2nd edition**(Ch. 16).
179. Mayers, B., et al., *J. Am. Chem. Soc.*, 2003. **125**: p. 13364
180. Jiang, X., et al., *Chem. Phys. Lett.*, 2004. **385**: p. 472.
181. Jiang, X., L. Kemal, and A. Yu, *Materias Letter*, 2006. **61**: p. 2584-2588.
182. Jiang, X. and A. Yu, *J. Nanopart. Res.*, 2007. **10**: p. 475-486.
183. Gates, B., et al., *Adv. Funct Mater.*, 2002. **12**: p. 679.
184. Cullity, B.D. and S.R. Stock, *Elements of X-Ray Diffraction*. 3rd ed. Prentice-Hall, 2001.
185. Mayers, B., et al., *Chem. Mater.*, 2003. **15**: p. 3825.
186. Mayers, B.T., et al., *Chem. Mater.*, 2003. **15**: p. 3852-3858.
187. Xia, Y., et al., *Adv. Mater*, 2003. **15**: p. 353-389.

188. Jiang, Z.Y., et al., Chem. Phys. Lett., 2003. **368**: p. 425.
189. Wang, J.J., et al., Ultrason. Sonochem., 2004. **11**: p. 307.
190. Cheng, B. and E.T. Samulski, Chem. Commun., 2003: p. 2024.
191. Tang, Z.Y., et al., Adv. Mater, 2005. **17**: p. 358.
192. Zhang, B., et al., J. Phys. Chem. B, 2005. **109**: p. 22830.
193. Gauta, U.K., M. Nath, and C.N.R. Rao, J. Mater. Chem., 2003. **13**: p. 2845.
194. Klyaman, D.L. and T.S. Griffin, J. Am. Chem. Soc., 1973. **95**: p. 197.
195. Wang, Z.H., et al., Inorg. Chem. Commun. **6**: p. 1329.
196. Ren, L., et al., J. Phys. Chem. B. **108**: p. 4627.
197. Cao, X.B., et al., Adv. Mater., 2004. **16**: p. 649.
198. Cao, X.B., Y. Xie, and L.Y. Li, Adv. Mater, 2003. **15**: p. 1914.
199. Zhang, B., et al., Angew. Chem. Int. Ed, 2006. **45**: p. 2571.
200. Ishida, K. and K. Tanaka, Phys. Rev. B, 1997. **56**: p. 206.

Reply to the comments from Examiners

The author thanks the examiners for the comments and suggestions provided. Each point has been considered carefully and the thesis is revised accordingly. The followings are our responses to each of the comments (*in italic*).

1. *“A general question is regarding the interaction scale between the metal face and the surfactant/organic molecule from the MD/DFT simulation.*

(a) As presented on Page 87 (DFT), the interaction scale between Au and PVP is {111} -0.0531 eV (-1.3 kcal/mol), {100} -0.0425 eV (-1.0 kcal/mol) and {110} 0.0197 eV (0.5 kcal/mol), which is the same scale as the thermal energy (kT or RT , 0.6 - 0.7 kcal/mol). The question is whether so small difference in the interaction energy is enough for PVP preferentially to block facet {111}.”

To understand the PVP-controlled preferential growth of Au nanoparticles, two issues need to address clearly. First, Density Function Theory (DFT) simulation belongs to quantum mechanics, and it can be used to calculate the binding energy (BE) between metal and surfactants, e.g., Au and PVP. The energy unit for BE is eV rather than kcal/mol. The latter is an energy unit generally used for the description of micro-scale system but not binding energy. Second, the difference of binding energies from different crystal surfaces and PVP is “big” not “small”. For example, the difference of {111}/PVP-{100}/PVP is $\sim 20\%$, and that of {111}/PVP-{110}/PVP is $>60\%$. So such a “big” difference of binding energy is sufficient to result in the preferential growth of Au nanoparticles.

(b) “On page 102-109, MD results indicate the interaction between the Ag surface and surfactant molecules is -250 to -959 kcal/mol (Table 4.1). It is well known that a singly covalent bond is 800 - 100 kcal/mol. This means that the interaction between the Ag surface and surfactant molecules corresponds to a few chemical bonds and will completely block all surfaces.”

The interaction energy obtained by MD simulation describes the interaction between the whole AOT molecules and silver surface, but not the formation of a bond or a few bonds between them, which is not simply attributed to the bond energy. Actually, the interaction energy is heavily affected by the whole coverage of surfactant on particle surface. Given dense coverage occurred on the particle surface, the adsorbed molecules still cannot block all surfaces, so the particles can gradually grow bigger.

(c) *“Is the difference in the interaction between the metal surface and surfactant molecules from DFT and MD simulation stemmed from the accuracy of these two methods?”*

The difference in the interaction energy is indeed stemmed from the accuracy of these two methods. It is noted that the MD simulation provides the interaction energy between a whole surfactant molecule and metal surface, but DFT focuses on the interaction between an atom of the surfactant molecule and metal surface.

2. *“On page 77, the second peak at 750-800 nm is hard to be observed. On page 90, this peak marginally appears as a shoulder. Does the deconvolution indicate this peak?”*

As suggested, Figure 4.4 on Page 77 has been changed where the second peak at 750 - 800 nm can be seen easily.

3. *“On page 80, last 2 lines and page 81: the Au average particle size changes with the aging time, but seemingly not in the same way. What are the possible reasons behind?”*

The size distribution patterns were constructed using image analysis software called ImageJ, which is slightly different from TEM observations. During the analysis, the

overlapped or closed particles were detected as one single particle, so it is not surprise that the large size distribution was found in a short heating time.

4. *“On page 100, C₁₂SH seems to freeze the Ag-AOT shape as the triangular nanoplates. However, the adsorption peak red-shifts from 685 nm (Ag-AOT) to 707 nm (Ag-AOT-C₁₂SH). Is this shift possibly caused by the size change and/or by the change of Ag surface refractive index?”*

The addition of C₁₂SH resulting in a slight red-shift in adsorption is probably caused by the aggregation of a small amount of Ag plates but not by size change or the change of refractive index.

5. *“On page 105, last 3-4 line: the interaction energy between C₁₂SH and Ag(100)-AOT is -104.6 kcal/mol, while on page 106, line 1-2: the total reduced energy is 130 kcal/mol. Are these two statements conflict?”*

The two energies, i.e., interaction energy and total energy, are different concepts in describing particle surface energy. These two statements are not conflict. The detailed description has been presented in the thesis (please see pp105-106).

6. *“On page 125, last line 2” the sentence “This Figure 4.1.... obtained” does not make sense. Need revision.”*

As suggested, this sentence has been corrected in the revised version.

In addition, all the typos and grammar errors have been revised as suggested.